LIQUID-CRYSTAL MICRODROPLETS AS OPTICAL MICRORESONATORS AND LASERS

Matjaž Humar

Doctoral Dissertation
Jožef Stefan International Postgraduate School
Ljubljana, Slovenia, February 2012

Evaluation Board:

Prof. Boštjan Zalar, Chairman, Jožef Stefan Institute, Ljubljana, Slovenia

Asst. Prof. Miha Škarabot, Member, Jožef Stefan Institute, Ljubljana, Slovenia

Prof. Slobodan Žumer, Member, University of Ljubljana, Ljubljana, Slovenia

MEDNARODNA PODIPLOMSKA ŠOLA JOŽEFA STEFANA
JOŽEF STEFAN INTERNATIONAL POSTGRADUATE SCHOOL

Matjaž Humar

LIQUID-CRYSTAL MICRODROPLETS AS OPTICAL MICRORESONATORS AND LASERS

Doctoral Dissertation

TEKOČEKRISTALNE MIKROKAPLJICE KOT OPTIČNI MIKRORESONATORJI IN LASERJI

Doktorska disertacija

Supervisor: Prof. Igor Muševič

Ljubljana, Slovenia, February 2012

Poets say science takes away from the beauty of the stars - mere globs of gas atoms. I, too, can see the stars on a desert night, and feel them. But do I see less or more?

Richard P. Feynman

Index

Abstract **XI**

Povzetek **XII**

Abbreviations **XIII**

1 Introduction **1**
- 1.1 Whispering-gallery modes 1
  - 1.1.1 Tunable WGMs 2
  - 1.1.2 WGM microcavities for biosensing 3
  - 1.1.3 WGM microcavities for filters and optical communications 4
  - 1.1.4 WGM ultralow-threshold microlasers 4
  - 1.1.5 Coupled WGM cavities 4
- 1.2 Circular and spherical Bragg microcavities 5
- 1.3 Liquid crystals 6
  - 1.3.1 Polymer dispersed liquid crystals 6
  - 1.3.2 Lasing in cholesteric liquid crystals 7
  - 1.3.3 Liquid crystal biosensors 8
- 1.4 Goal of the thesis 10

2 Theoretical background **13**
- 2.1 Optical microcavities 13
  - 2.1.1 Quality factor 13
  - 2.1.2 Purcell effect 14
- 2.2 Theory of WGMs 15
  - 2.2.1 WGM frequencies in an isotropic sphere 15
  - 2.2.2 Approximate solutions 18
  - 2.2.3 Non-spherical whispering-gallery cavity 19
  - 2.2.4 WGM frequencies in an anisotropic sphere 20
  - 2.2.5 Excitation of WGMs 21
    - 2.2.5.1 Evanescent field coupling 21
    - 2.2.5.2 Fluorescence 21
- 2.3 Theory of lasing 21
- 2.4 Bragg microcavities 23
- 2.5 Liquid crystals 25
  - 2.5.1 Introduction to liquid crystals 25
    - 2.5.1.1 Nematic liquid crystals 25
    - 2.5.1.2 Order parameter 26
    - 2.5.1.3 Elastic properties of liquid crystals 26
    - 2.5.1.4 Electric field effect in liquid crystals 26
    - 2.5.1.5 Change of the refractive indices of liquid crystals by temperature 27

2.5.2 Surface anchoring of liquid crystals 28
2.5.2.1 Anchoring on a anisotropic surface 28
2.5.2.2 Anchoring on an isotropic surface 29
2.5.3 Cholesteric liquid crystals 29
2.5.3.1 Position and width of the photonic bandgap 30

3 Materials and methods 31
3.1 Liquid crystals 31
3.2 Dyes 31
3.3 Carrying medium 32
3.4 Making dispersion of LC droplets 33
3.5 Optical setup 34
3.6 Microfluidic setup for chemical sensing 37
3.7 Setup for angular measurements of the 3D laser emission 38
3.8 Setup for 3D laser polarization measurements 39
3.9 Sample preparation and setup for strain tuning 40
3.10 Sample preparation for electric field tuning 41
3.11 Preparation of cholesteric 3D lasers 41

4 Experimental results and discussion 43
4.1 Dispersion of liquid-crystal droplets 43
4.2 Whispering-gallery modes in nematic liquid-crystal droplets 46
4.2.1 Polarization properties 48
4.2.2 Fitting the WGMs 51
4.2.3 Q-factor 51
4.3 Electric field tuning of WGMs in nematic droplets 53
4.3.1 Director distortion under electric field 53
4.3.2 WGMs under electric field 53
4.3.3 Tuning of multiple droplets 57
4.3.4 In-plane electric field 57
4.3.5 Electric field with droplets containing particles 58
4.4 Temperature tuning 61
4.5 Optical tuning 65
4.6 Strain tuning 69
4.7 Chemical sensors based on WGMs in LC droplets 71
4.7.1 LC droplets at different surfactant concentrations 71
4.7.2 Lasing in LC droplets 72
4.7.3 Sensing characteristics 74
4.7.4 Sensing in non-lasing regime 76
4.8 3D laser 77
4.8.1 Cholesteric liquid-crystal droplets 77
4.8.2 Simulation of the CLC droplet configuration 78
4.8.3 Lasing characterization 81
4.8.4 Polarization 85
4.8.5 Angle dependance 86
4.8.6 Tunability 86
4.8.7 Lasing of higher Bragg modes 87
4.8.8 Polymerizable 3D laser 90
4.8.9 Particles incorporated into a CLC droplet 93

5 Conclusions 95

6 Acknowledgements 99

7 Zahvala **101**

8 References **103**

Index of Figures **111**

Index of Tables **113**

Appendix A: Further observations **115**
Lasing and switching in ferroelectric LCs 115
Photonic molecules 117
Measuring spectral width of WGMs using a Fabriy-Perot interferometer . . . 117
Pulse length of the 3D laser 118

Appendix B: Bibliography **121**

Abstract

This thesis investigates the use of single liquid-crystal droplets as optical microresonators and lasers. We have shown that liquid-crystal droplets can support a number of different optical modes that can be excited by introducing a fluorescent dye in the liquid crystal material and using an external excitation source of light. These optical modes are in general different from the ones in isotropic materials, because of birefringence of the liquid crystals and specific configurations of the director field within the droplet. The droplets were prepared just by mechanical mixing of a liquid crystal material and another non-miscible fluid. The director structure in the droplets self assembles to minimize the elastic energy. To measure the optical properties of the microresonators an optical setup was built that includes a pulsed laser for excitation and a spectrophotometer for spectral analysis. Regarding the type of liquid crystalline material used for the droplets and the type of optical modes supported in the droplets, the thesis is basically divided into two parts.

In the first part, nematic liquid crystal is used to make the droplets. It has been shown that the nematic droplets confine light by total internal reflection and therefore support whispering-gallery modes. At higher peak intensities of the pump laser, low threshold multimode lasing has been achieved. The optical modes were tuned by electric field, temperature and mechanical deformation. In the case of applying electric field, the nematic director orientation changes locally, so that the circulating light sees a change in the refractive index. On the other hand, by changing the temperature only the order parameter is altered, which results in the change of both ordinary and extraordinary refractive indices. In the case of mechanical deformation, only geometrical path length is changed with the applied strain, like it would happen also in an isotropic droplet. It has been shown that the response to electric field and temperature is much larger than reported before in the literature for other materials. By applying just an electric field of few V/μm or changing the temperature by few °C, the modes shift by more than 10 nm in visible light. By using a nematic droplet floating in water, also a chemical sensor was demonstrated. The surfactant molecules, which concentration we want to measure, adsorp to the surface of the liquid-crystal droplet and change the anchoring and therefore also the director configuration in the droplet. This results in a change of the optical properties of the droplet and therefore the frequencies of the optical modes. The spectrum of light captured from such a droplet serves as an indicator of the presence of the surfactant in the surrounding water.

In the second part of the thesis, cholesteric liquid crystals with selective reflection in visible light were used to make the droplets. The cholesteric liquid crystal in the droplet self assembles so that the helical axis is pointing from the center in all the directions to the surface of the droplet. The structure is acting as a spherical Bragg onion microcavity with periodic modulation of the refractive index that confines the light into the center of the droplet. By having a fluorescent dye in the LC and illuminating the droplet by an external pulsed laser, the droplet starts to emit laser light in all the directions. In this way we have made a 3D laser, a coherent isotropic point source of light. The spherical cholesteric laser is one of the first lasers emitting in all the directions and also one of the easiest lasers to make in general. The laser is also highly tunable by changing the temperature.

Povzetek

Doktorsko delo obravnava uporabo posameznih tekočekristalnih kapljic za optične mikroresonatorje in laserje. Pokazali smo, da so v tekočekristalnih kapljicah možni številni optični nihajni načini, ki jih vzbudimo s pomočjo zunanjega vira svetlobe in fluorescentnega barvila razporejenega v tekočem kristalu. Optični nihajni načini v kapljicah tekočega kristala so v splošnem drugačni od tistih v izotropnih snoveh. Razlog je dvolomnost tekočih kristalov in posebne ureditve tekočekrstalnega direktorja znotraj kapljice. Kapljice smo pripravili z enostavnim mehanskim mešanjem tekočega kristala in druge tekočine v kateri tekoči kristal ni topen. Struktura direktorja se v posameznih kapljicah uredi tako, da minimizira elastično energijo. Za namene proučevanja optičnih lastnosti kapljic, smo sestavili optični sistem, ki vključuje pulzni laser za vzbujanje kapljic in spektrofotometer za spektralno analizo. Glede na uporabljeno vrsto tekočega kristala in na tip optičnih načinov v kapljicah, je doktorska disertacija razdeljena na dva dela.

V prvem delu smo kot material za pripravo kapljic uporabili nematski tekoči kristal. Pokazali smo, da zaradi totalnega notranjega odboja, nematske kapljice zadržujejo v svoji notranjosti svetlobo in zato v njih obstajajo tako imenovani whispering gallery nihajni načini. Pokazali smo tudi, da ob vzbujanju z višjo intenziteto, že pri zelo nizkem pragu, kapljice pričnejo oddajati večrodovno lasersko svetlobo. Optične nihajne načine lahko uglašujemo s pomočjo električnega polja, temperature ali mehanske deformacije. Ko na kapljico priključimo električno napetost, v njeni notranjosti lokalno spremenimo smer nematskega direktorja, kar vpliva na lomni količnik, ki ga vidi svetloba na poti po robu kapljice. S spremembo temperature, pa se po drugi strani spremeni samo nematski red, kar vpliva na spremembo rednega in izrednega lomnega količnika. Pri mehanski deformaciji kapljice, pa se spremeni geometrijska dolžina poti po kateri potuje svetloba, pri čemer je učinek enak kot v izotropni kapljici. Pokazali smo, da je vpliv električnega polja in temperature precej večji kot pri doslej v literaturi objavljenih rezultatih za drugačne materiale. Z električnem poljem le nekaj V/µm, ali spremembo temperature za samo nekaj °C, se optični nihanji načini v vidni svetlobi premaknejo za več kot deset nanometrov. Nematske kapljice dispergirane v vodi smo uporabili tudi kot kemične senzorje. Molekule surfaktanta, ki ga hočemo zaznati, se adsorbirajo na površino kapljice in s tem spremenijo sidranje tekočega kristala ter posledično smer nematskega direktorja v kapljici. To pomeni, da se spremenijo tudi optične lastnosti kapljice in zato tudi optični nihajni načini vzbujeni v kapljici. Z meritvijo spektra svetlobe, ki ga oddaja kapljica, lahko določimo prisotnost surfaktanta v vodi.

V drugem delu doktorske disertacije smo za pripravo kapljic uporabili holesterični tekoči kristal, ki ima selektivno refleksijo v vidni svetlobi. Tekoči kristal se v kapljici samouredi tako, da je vijačnica usmerjena iz centra v vse smeri proti površini kapljice. Tako tvori čebulasto Braggovo strukturo s periodično modulacijo lomnega količnika, ki zadržuje svetlobo v kapljici. Če imamo v tekočem kristalu še fluorescentno barvilo in barvilo vzbujamo z zunanjim pulznim laserjem, kapljica prične oddajati lasersko svetlobo v vse smeri v prostoru. Tako smo naredili 3D laser, ki je koherentno isotropično točkasto svetilo. Sferični holesterični laser je en izmed prvih laserjev, ki oddaja svetlobo v vse smeri. Je tudi en izmed laserjev, ki ga je v splošnem najlažje narediti. S spreminjanjem temperature lahko laser tudi uglašujemo v velikem območju.

Abbreviations

5CB = 4’-pentyl-4-biphenylcarbonitrile
a.u. = arbitrary units
AOD = acousto-optic deflectors
CLC = cholesteric liquid crystal
CROW = coupled resonator optical waveguide
CW = continuous wave
DAC = digital-to-analog converter
DCM = 4-(dicyanomethylene)-2-methyl-6-(4-dimethylaminostyryl)-4H-pyran
FCPM = fluorescence confocal polarizing microscopy
FSR = free spectral range
FWHM = full-width at half-maximum
IR = infrared
LC = liquid crystal
MDR = morphology-dependent resonance
MF = melamine formaldehyde
ND = no data
Nd:YAG = neodymium-doped yttrium aluminium garnet
NIR = near infrared
NLC = nematic liquid crystal
PBG = photonic bandgap
PDLC = polymer dispersed liquid crystal
PDMS = polydimethylsiloxane
PVA = polyvinyl alcohol
SDS = sodium dodecyl sulfate
SPP-106 = rhodamine B tetradecyl ester chloride
UV = ultraviolet
WGM = whispering-gallery mode

1 Introduction

In recent years, great attention has been paid to the development of micro-optical components and integrated optic circuits. Small size, easy and cheap manufacture, high speed, nonlinear properties and tunability are the main properties that scientist and companies are searching for. Especially tunability is very difficult to achieve just using solid state components. Nowadays, top down approach, mostly lithography is used to manufacture optical micro-components. In the future, bottom up approach with self assembly could be a better way to produce smaller and cheaper devices.

One of the most important optical components are *optical microcavities* [1]. These structures resonantly couple light to small volumes, that is on the order of a small multiple of the optical wavelength. Like mechanical oscillators, they support resonant frequencies that are dependent on their size. The smaller the cavity, the further the resonant modes are from each other. In this case less modes are going to be excited, achieving for example single mode lasing. Smaller size also means stronger coupling of light with matter. Ideal resonator would have infinitely sharp resonances and would confine light indefinitely. In real resonators this is not possible because of the losses such as absorbtion and radiation loss. The *resonant Q-factor* gives how much time the light is confined in the resonator in terms of optical period. From the Q-factor we can calculate the spectral width of the resonance. There are three kinds of confinement of light in microcavities, by total internal reflection, by a periodic structure and by plasmons. These three types of microcavities give increasing confinement of light, in the plasmon case even below the diffraction limit.

By adding an active material to the microcavity, microlasers can be made. So far, lasing has been achieved in a number of different dielectric microstructures, such as photonic crystal defect microcavities [2], micropillar cavities [3], whispering-gallery microcavities [4], a 3D photonic crystal of the liquid-crystal blue phase II [5], and has been combined with plasmon resonances in nanosized laser sources [6, 7].

Optical microcavities are already used in commercial applications such as laser diodes that we can find in a variety of products including CD, DVD and BluRay players. For basic research the microcavities provide an excellent platform to study strong coupling between light and matter (cavity quantum electrodynamics - QED), atom optics and other fields of photonics and nanophotonics.

1.1 Whispering-gallery modes

One type of microresonators are made of transparent dielectric spheres or planar circular structures with typical radius of $10 - 50\,\mu\text{m}$ [8]. If the refraction index of the sphere is grater than the index of the outside medium the light can be trapped inside the sphere as a consequence of total internal reflection (Figure 1a). If the circulating light returns to the same point in phase, we get resonant standing waves (Figure 1b). This resonant modes are referred to as *whispering-gallery modes* (WGMs) or *morphology-dependent resonances* (MDRs). The first name comes from Whispering Gallery, the dome of St. Catherine's cathedral in London where L. Rayleigh observed and analyzed sound bouncing of the dome walls. Sometimes they are called also *optical atoms*, since the electric field distribution resembles wavefunctions in hydrogen atom, as well as the three mode numbers and polarization are equivalent to the three quantum numbers and spin in hydrogen atom.

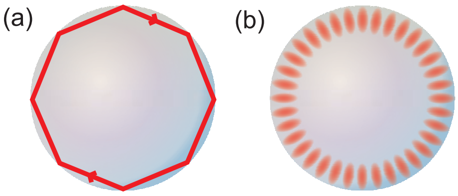

Figure 1: *Schematics of WGMs.* a) Geometrical optics and b) wave optics representation of whispering gallery modes.

WGMs are especially interesting because of their high Q-factors. In silica microspheres the Q-factor can be as high as 8×10^9 [9]. This is possible because of very low optical loss of bulk silica and nearly perfect surface. As a starting material a commercial optical fiber is usually used. The tip of the fiber is melted with a high power laser or an oxygen-hydrogen torch. Surface tension creates nearly perfect sphere with very smooth surface. The advantage of using optical fiber is that the fibers are made from very clean materials that have very low optical losses. But the loss limit is usually determined by the surface. Just exposure to the air can significantly lower the Q-factor because of the formation of -OH groups on the surface. Spherical microresonators are also interesting because the solutions of Maxwell equations in spherical microresonator are analytical, which can help to better understand the physics behind. Instead of a sphere, toroidal resonators are also used. They are made from silica on a silicon wafer using lithographic methods [10]. Microtoroid resonators with Q-factors as high as 10^8 were made [1].

Because of their small size and high Q-factors they are perfect candidates for miniaturization and integration of sensors and optical systems. Despite these advantages there is still a long way towards real life applications. In laboratories a wide range of applications were demonstrated [11] such as microlasers, narrow filters, optical switching, ultrafine sensing, displacement measurements, high resolution spectroscopy, Raman sources, enhancement and suppression of spontaneous emission and studies of nonlinear optical effects. Impressive results have been achieved so far. With new materials and microfabrication techniques there is still a lot of space for improvement. In the near future a wide range of commercial applications using WGMs is expected.

1.1.1 Tunable WGMs

One important aspect of WGM microcavities is to be able to change the resonant frequencies in real time. The frequencies are tuned by changing the optical path of the light, by either changing the refractive index of the resonator or by changing the physical dimension of the resonator. This can be done in a number of different ways including electric field, temperature and mechanical strain. The electric tuning is especially interesting since it is usually fast and can easily be integrated into current electro-optical circuits. Even though most of the resonators are made of a solid material, which optical properties can not be changed much, we can still change the refractive index of the cladding layer. This effects the evanescent field extending out of the resonator enabling tunability, however to a smaller extent. A microresonator can be for example immersed in a liquid crystal and a voltage is applied across the system [12, 13]. Because the evanescent field represents only a small fraction of the total electric field of the WGMs, the tunability is much lower than when having the liquid crystal inside the cavity. Maune et al. [12] report 0.01% tunability by applying $2\,\mathrm{V}/\mu\mathrm{m}$ using silicon-on-insulator ring resonator embedded in a LC. Piegdon et al. [13] have achieved tunability of 0.5% when applying very low fields of $300\,\mathrm{V/cm}$ to a $3\,\mu\mathrm{m}$ GaAs microdisks with InAs quantum dots embedded in 5CB. However, the reported mode shift is nonreversible when the field is switched off and only heating to isotropic phase brings the system back to the original state. Another way of tuning the modes is to make the resonator out of a solid state material that has large electro-optic effect. However, the effect is much lower than in LCs. Wang et al. [14] report WGM shifts of 0.006% by applying 1.5 V/μm in lithium niobate microring resonators. Electric field can also be applied to droplets. Kiraz et al. [15] reports tuning WGMs in liquid microdroplets standing on superhydrophobic surface using electrowetting. The tunability in this case is 0.8% when applying electric field of 2.9 V/μm.

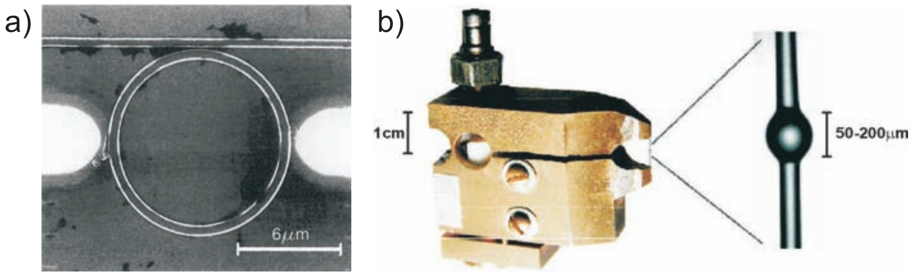

Figure 2: *Two examples of tunable WGM resonators.* a) Electrically tunable microring resonator. Liquid crystal cladding layer and two electrodes (bright patches on the left and right of the ring) are used to change the refractive index outside the resonator. Reprinted with permission from [12]. Copyright 2003, American Institute of Physics. b) Mechanical tuning of a bottle microresonator by stretching. Reprinted with permission from [16].

Another way of tuning is by changing the temperature, which changes the refractive index of the resonator or its physical size. Usually the effect of temperature is quite small for solid state materials and for example tunability of 10 pm/K at 1.5 μm was achieved in silica [17]. In the case of soft materials like PDMS, the tunability is larger, 0.3 nm/K at 1.5 μm was shown [18]. Liquid crystals were employed before for temperature tuning of WGMs, but again just as a cladding. Temperature tuning of 8 nm at 1.2 μm has been demonstrated [13]. Due to their high Q-factors the WGMs can also be used as very precise temperature sensors [17, 18].

Tuning by mechanical deformation has been achieved in a number of different geometries and materials. Two examples are droplets of a liquid in a PDMS polymer [19] and fused silica microresonators (Figure 2b) [16]. In both cases the achieved tunability was approximately 1 nm in visible. Since it is possible to measure the deformation, also a force sensor can be made in this way [20].

1.1.2 WGM microcavities for biosensing

One of the most interesting applications of WGMs is biosensing [10, 21, 22]. The WGMs can interact with the environment outside the microsphere through evanescent field. A particle on the surface or near the surface of a microsphere changes the optical path of the light and/or the cavity loss. This causes a shift of the resonant frequency. Because spherical microresonators have really high Q-factors, they are among the most sensitive optical systems. In the case of a microresonator with $Q = 10^8$ and diameter 100 μm the light travels few tens of meters around the sphere and the particle on the surface is sampled more than 100,000 times. In this way, it is possible to detect single molecules attaching to the surface [10]. We can further functionalize the surface of the microresonator in order to bind just specific molecules to the surface, in this way selective single molecules detection is possible. Such detection has also been demonstrated in real life environment like blood serum.

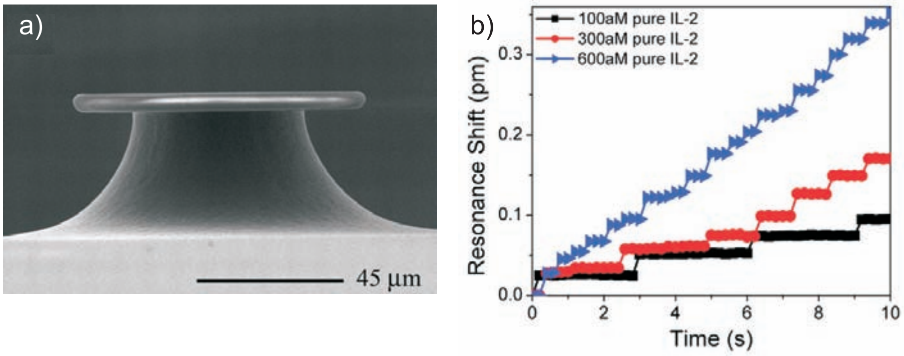

Figure 3: *Silica microtoroid resonator used for biosensing.* a) SEM image of a microtoroid resonator. b) Shift of a single WGM in time at three different concentration of target molecules. The steps are single molecule binding events to the microtoroid. From [10]. Reprinted with permission from AAAS.

1.1.3 WGM microcavities for filters and optical communications

The need for ever greater bandwidth in communications is growing continuously. Today optical communication is widely used for long range transmission. To increase the bandwidth of a single optical fiber, more wavelengths have to be used at the same time. Therefore, the interest in optical filtering and switching is gaining interest in recent years. An optical microresonator enables coupling between two optical fibers, forming a so called add/drop filter [23]. Single frequency that matches the frequency of microresonator can be transferred with low loss from one fiber to the other fiber. In the same way as a frequency is dropped from the fiber another frequency can be added. The advantages of a microresonator in comparison with other filters is its small size and potential for high density integration on a chip. By electrically changing the refractive index it is also possible to dynamically select the filtered frequency.

1.1.4 WGM ultralow-threshold microlasers

WGM resonators can be also used as laser sources. Lasing has been demonstrated in different microresonators such as liquid droplets, microspheres, microdisks and microcapilares. Because of small cavity volumes and high Q values, submicrowatt optical pump lasing thresholds can be achieved [1]. Usually a rare earth doped silica microsphere coupled to an optical fiber is used. The frequency of the pump laser is adjusted so it matches one WGM. Above the threshold one or more peaks that correspond to WGMs appear. Microresonator lasers could extend the range of available laser wavelengths especially for compact systems like semiconductor lasers.

1.1.5 Coupled WGM cavities

From applications point of view, also multiple coupled WGM microcavities are very interesting. If two resonators are so close together, that their evanescent fields overlap and they become coupled [23]. The light can tunnel from one to another (Figure 4). The process is efficient only in the case when the frequencies of the resonators match perfectly. A single WGM cavity is called optical atom, more of them together are called *optical molecules* [24, 25]. A chain or cavities acts as a *coupled resonator optical waveguide* (CROW) [26] and serves as an optical delay line. These structures are usually made by lithography with the size and gaps controlled exactly.

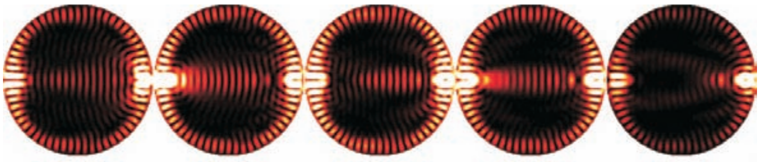

Figure 4: *CROW simulation.* Electric field intensity distribution in a chain of five touching microspheres. Reprinted with permission from [27].

1.2 Circular and spherical Bragg microcavities

Apart from light confinement by reflection and total internal reflection such as in WGMs, confinement by photonic structures is even more efficient. Dielectric photonic structures have a periodic modulation of the refractive index with the period comparable to the wavelength of the light. The periodic structure can be one-, two- or three-dimensional. On each period of the structure a part of incident light is reflected and than constructively or destructively interferes. Therefore, the light can be reflected from the structure, this effect is called *Bragg reflection.* Bragg reflection is more known in the case scattering of X-rays from a crystal lattice, which is exactly the same phenomenon, just at shorter wavelengths. For the wavelength range that is reflected from the structure, we say that *photonic bandgap* (PBG) exists. The frequencies in this range are forbidden inside the periodic material. The PBG usually changes for different directions. Structures having the PBG are referred to as *photonic crystals.* If the propagation of the same frequency range is forbidden in all the directions in space and for all the polarizations, we have *full photonic bandgap.* Typically the structures based on photonic crystals can confine light in a volume much smaller than for example in the case of WGMs, however at the cost of lower Q-factors, that are up to approximately 10^5 compared to 10^{10} for WGMs [1].

One type of PBG structures are the *circular Bragg microcavities* [28–30] and *spherical Bragg microcavities* [31–34] made of concentric rings (planar structure, Figure 5a) or concentric shells ("onion" structure), respectively. Such structures are basically one dimensional photonic crystals, but wrapped around the central point. Light going out from this central point is reflected back by the periodic structure and is confined in the center. Spherical Bragg-reflector microcavities, are particularly interesting because of their perfect rotational symmetry in 3D. The PBG is independent of the direction of light propagation and the light is strongly confined in all directions.

In non-layered spheres there are a large number of modes present, which can be tailored to our needs only in a very limited way. But for a Bragg microcavity the layered structures can be modified so that only a limited number of modes are possible. In contrast with other 3D photonic crystals such as opals, the refractive index contrast between the layers can be arbitrarily small in order to generate full PBG. Therefore spherical Bragg microcavities are useful in a number of ways. By placing an emitter in the center of the cavity, suppression of the spontaneous emission and modification of the fluorescent decay rate can be achieved. High intensity of the light trapped in the center enables nonlinear processes such as second harmonic generation and in strong coupling of light with matter. Furthermore, such cavities can be used for light sources such as microcavity lasers and electroluminescent devices.

A number of Bragg-onion resonator structures have been realized in 2D using standard planar lithography (Figure 5a) and lasing has been demonstrated in these structures (Figure 5b) [28–30]. The natural step now would be to go into three dimensions. However, unfortunately, it is quite difficult to manufacture any 3D solid-state microcavity [35]. There have been several attempts to produce 3D Bragg-onion resonators by chemical synthesis [36] or by combining etching and chemical vapor deposition [34], but to our knowledge, lasing has not been achieved in these solid-state structures.

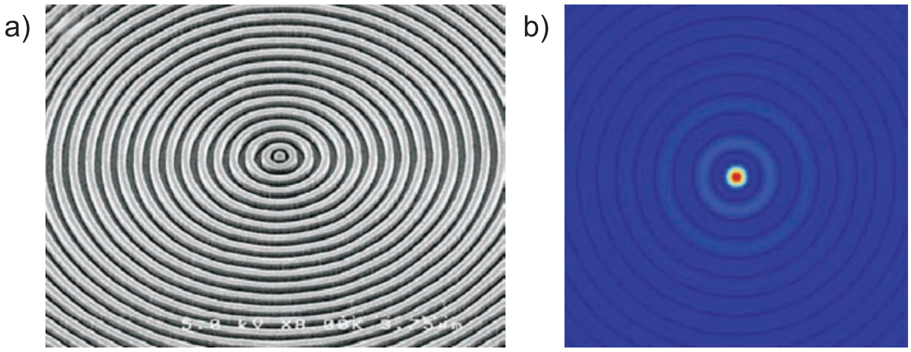

Figure 5: *2D Bragg microcavity laser.* a) SEM image of a laser made by lithography. b) Simulation of electric field distribution in such a laser for the mode with the lowest angular modal number, that has the maximum in the center of the microcavity. Reprinted with permission from [37].

1.3 Liquid crystals

Liquid crystals (LCs) are anisotropic fluids whose molecules have orientational and sometimes positional order [38]. The alligment direction is dictated by the external field or confining surfaces. *Nematic liquid crystals* (NLCs) are the simplest case of liquid crystals and are composed of rod-like molecules that are oriented in a particular direction and do not have positional order. If the molecules of a NLC are chiral or another chiral molecule, called *chiral dopant*, is added to the NLC, a helical twist is introduced. Such LCs are refereed to as *cholesteric liquid crystals* (CLCs).

When an external AC electric field is applied to a NLC sandwiched between confining surfaces, molecules tend to align with their long axes into the field direction to minimize the elastic and electric energy. This causes collective reorientations of NLC molecules, and the liquid crystal is elastically distorted. As the NLC molecules are usually strongly anchored at the confining surfaces of the device, the elastic deformation provides restoring torques, which drive the NLC into original configuration, once the field is switched-off. Due to their high birefringence (typically $0.1 - 0.2$) and large optical response to the external electric field, nematic liquid crystals are now widely used in LCDs, 2D spatial light modulators, optical filters, tunable waveplates and optical switches. Electrically tunable optical devices such as cholesteric liquid crystal lasers [5,39–43], beam steering devices, tunable 2D photonic nematic colloidal crystals [44] and solid state optical microresonators with a NLC cladding layer [12] have been demonstrated.

1.3.1 Polymer dispersed liquid crystals

In practical applications, the LCs are confined by some external surface that aligns the molecules in a particular direction. The confinement is in most cases in a form of a thin layer of LC, several micrometers thick. The confining glass plates used as substrates are coated with different materials and mechanically treated to induce the correct anchoring. Another type of confinement is to encapsulate the LC droplets into a carrying material. LC droplets in a polymer matrix are known as *polymer dispersed liquid crystals* (PDLCs) [45,46]. The size of the droplets is usually in the order of a micron, so that the scattering of light is as efficient as possible. The fraction of the LC in PDLCs can be as high as 50% to 90%. PDLCs are useful for switchable windows and displays, however they are actually not really much used in commercial applications, even though, they have the advantage that no alignment layers and no polarizers are necessary. PDLC switchable windows and displays are based on the fact, that with no electric field, the LC molecules in the droplets are randomly oriented and they scatter light, making the film opaque. But when the electric field is applied, the LC orients along the field, so that the refractive index for the light traveling perpendicular to the film matches the refractive index of the polymer matrix, making the film transparent. PDLCs are also interesting from basic research point of view, since they poses large surface-volume ratio, so that the surface effects and strong confinement can be studied into detail. By using different liquid crystals, different droplets size and different anchoring conditions, a huge variety of director configuration in the droplets can be achieved. Also the light propagation in such nonuniform and birefringent materials is very complex and can introduce a number of interesting optical phenomena including random lasing [47, 48].

1.3.2 Lasing in cholesteric liquid crystals

To make a laser, a cavity and a gain material are needed. By reflection of light the cavity confines the light in a small space and at the same time defines the possible modes inside it. The gain material amplifies these modes so that lasing is possible. In cholesteric liquid crystals the molecules rotate around their axis and make a helical structure. Because the molecules are birefringent, the helical structure has periodic modulation of the refractive index. If the periodicity matches the wavelength of light in the material, the light can be reflected from the structure. The CLC is therefore working as a one-dimensional photonic crystal and has a photonic bandgap. By introducing a gain material as for example a dissolved fluorescent dye, a laser can be made. The dye doped CLC acts at the same time as an optical cavity and at the same time as gain material. By pumping the CLC with an outside pulsed laser, single line lasing is achieved in the direction of the helical axis. The laser line is positioned on one of the two edges of the PBG, where the density of states in the largest. This can also be explained in terms of the photon lifetime. In the middle of the PBG the lasing is not possible, since the propagation of photons is prohibited and even the spontaneous emission is suppressed. On the other hand on the outside of the PBG the CLC does not reflect the light and the photons just escape the structure. However, on the edge of the PBG the spontaneous emission is not suppressed on a larger extent and the structure still has enough reflexivity, so that the photon lifetime is the longest. Therefore, the optical path of light in the structure is also the longest and also the gain is the largest.

The first observations of bandedge lasing in CLCs were independently demonstrated by Kopp et al. [49] and Taheri et al. [50, 51]. Since then, it has been shown in a number of experiments on dye-doped cholesteric liquid crystals that a low-threshold mirrorless lasing can be achieved [43, 52–54] (Figure 6). A recent review on this subject can be found in Ref. [55].

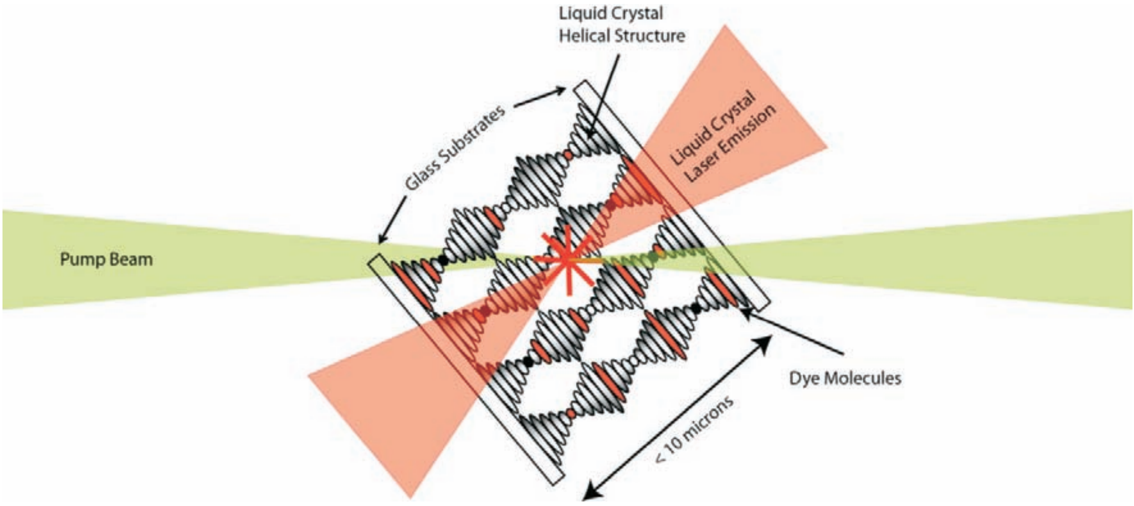

Figure 6: *CLC laser.* Principle of lasing from a thin layer of dye doped CLC. A pump laser (green beam) is used to excite the dye and the laser light is emitted along the helical axis (red beam). Reprinted from [52], Copyright (2006), with permission from Elsevier.

1.3.3 Liquid crystal biosensors

Surface science appears in a huge range of areas including basics science and large scale industrial production. In dispersions of small particles the surface has a large effect on their properties or the properties of the material containing them. Liquid crystals are especially interesting in this regard, since the effect of the surface extends deep into the bulk phase. The director orientation is therefore sensitive to the interface properties [56] such as the shape of the surface and its chemical composition. In most liquid crystal applications, such as LCDs, the surface is treated so that the correct anchoring of the liquid crystal is achieved. Planar anchoring is made by rubbing the surface, whereas the homeotropic anchoring is achieved by the deposition of a surfactant to the substrate. Similarly the molecules can be absorbed to the interface between a LC and water, changing the alignment of the LC. Since the anchoring angle is very sensitive to the surfactant concentration, this system can be used as a sensor. The anchoring also affects the bulk liquid crystal, the change being amplified through the long range orientational order of the liquid crystal, so the changes can be easily observed under a polarizing microscope. Therefore, the LC interfaces can be used as sensors to detect a variety of chemicals including phospholipids at LC-water interface [57, 58], protein binding [59], viruses [60, 61], bacteria [61] and pH measurements [62]. However, current methods of observing these changes are still based on bare-eye observation and small changes in the anchoring can not be detected in this way.

It has been demonstrated [63], that it is possible to change the anchoring of a LC on a hard substrate by controlled absorbtion of target molecules (Figure 7). In order to achieve this, chemical receptors are attached to a rubbed substrate. These receptors weakly bind the LC molecules orienting them in a well defined direction. When target molecules are introduced into the LC, they bind more strongly to the receptors replacing the LC molecules. However, non-targeted molecules bind the receptors more weakly than the LC molecules, so they do not replace the LC molecules. When LC molecules are not bind any more to the receptors, the LC tend to align parallel to the rubbing. This kind of sensors can be used for the detection of air contaminants. The molecules diffuse from the atmosphere through the LC to the receptors. R. Shah, et al. [63] reports detection of parts-per-billion vapor concentrations of targeted low molecular weight molecules, including organoamine and organophosphorus compounds.

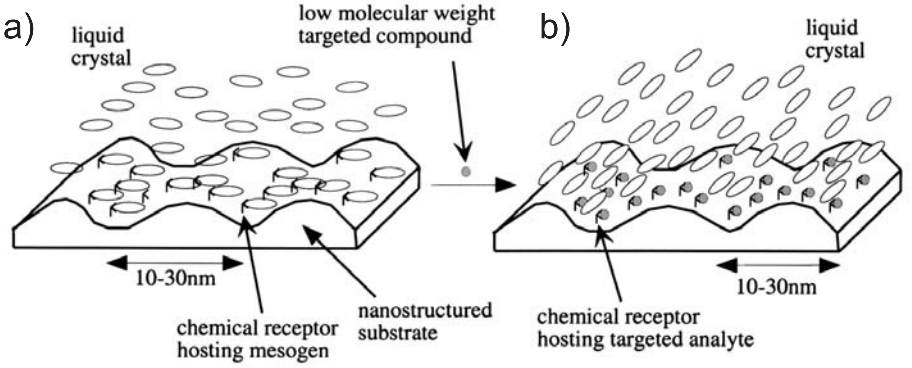

Figure 7: *LC sensor on hard surface interface.* The competitive interaction of a LC and targeted low molecular weight compound for a molecular receptor hosted on a surface with nanometer-scale topography. (a) Orientation of LC molecules is determined by the binding to the receptors. (b) Upon addition of the target compound the LC molecules detach from the receptors and align in the direction of surface grooves (rubbing direction). From [63]. Reprinted with permission from AAAS.

One drawback of hard surface LC sensors is that the target molecules must be soluble in the LC. However, most biological molecules are soluble in water, but not in non-polar solvents like LCs. Another option is to use the interface between a LC (not soluble in water) and the water environment containing the target molecules. Amphiphilic molecules such as phospholipids can bind to the interface, changing the anchoring (Figure 8). A typical setup consists of a thin metallic grid that is originally used for transmission electron microscopy. The square 100 µm × 100 µm openings in the grid are filled with a several micrometers thick LC layer, that is on one side in contact with a hard surface and on the other side in contact with water. The orientational changes are typically observed using a microscope and crossed polarizers. The reported sensitivities of such sensors are of the order of 10 µg/ml concentration in water, which corresponds to approximately one monolayer coverage of the LC interface with targeted molecules.

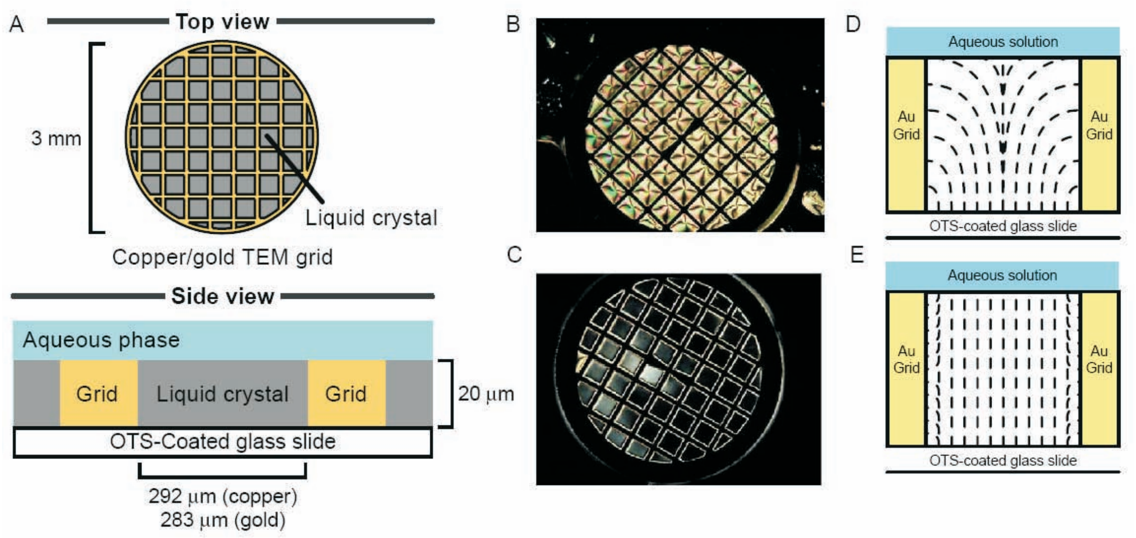

Figure 8: *LC sensor on fluid interface.* a) Experimental geometry used to create stable interfaces between aqueous phases and LCs. b) and c) optical images in crossed polarizers of 5CB confined to a copper grid immersed in b) pure water or c) an aqueous solution of 2.2 mM SDS. (d) and (e) schematic illustrations of the director profiles of the LC corresponding to d) planar anchoring of the liquid crystal at the interface with the aqueous phase and e) homeotropic anchoring with the SDS added. Reprinted from [64], Copyright (2005), with permission from Elsevier.

However, by this sensing method we do not have selective detection, as all the amphiphilic molecules are going to be absorbed to the interface. Alternatively, a monolayer of surfactant molecules can be made on the surface. If these molecules have specific binding sites, only target molecules will attach to them, changing their order or concentration. It has been also shown that is possible to measure the pH of the solution by carefully choosing the molecules absorbed on LC-water interface [62].

Instead of a flat layer of LC, also LC droplets dispersed in water can be used as sensors [61, 65, 66]. The director configuration in nematic droplets is dependent on the surface anchoring and it can be easily identified using a microscope. The advantage of such system is, that the droplets do not need any mechanical support or surface treatment, they are small and can be introduced into a microfluidic chip. Furthermore, it has been recently demonstrated that the sensitivity of droplets to specific molecules can be at least a factor of a million better compared to that of a flat sensing interface [67]. For endotoxins the sensing limit is as low as 1 pg/ml, which corresponds to about 30 molecules per droplet. Such huge amplification of sensitivity is attributed to the local binding of the surfactant molecules to the two surface boojum defects. This kind of sensor is also very specific, since only very specific surfactants such as endotoxins with six carbon chains are able to induce the changes in director configuration of the droplets.

1.4 Goal of the thesis

The purpose of this PhD work was to explore the possibility to use liquid crystal micro-droplets as optical microcavities that could be employed as novel micro light sources and other active optical elements in the microscale. The possible applications of such optical components extend from integrated optical circuits to imaging, holography and sensing. The work was stimulated by the lack of research in the area of soft photonics and the lack of such optical components.

We anticipated that liquid crystals could be used in the field of microresonators because of two main characteristics. Firstly, because of their long distance interaction and molecular order, liquid crystals offer high degree of self assembly and therefore possibly a route to easy, cheap and scalable manufacture of optical components. Secondly, they have large response to external stimuli, like electric and magnetic field, temperature, surface characteristics and light. These influences can change their optical properties and in this way offer large tunability of optical components. PDLCs have been studied extensively in the past, but individual droplets have never been considered as tunable optical microcavities. Most research in optical microcavities was conducted on solid state optic components or in isotropic liquids.

Primary goal was to demonstrate that liquid-crystal droplets (nematic, cholesteric, ferroelectric, smectic or blue phase) can support a number of different optical modes. By choosing different LC materials and different anchoring conditions we can achieve various LC configurations in the droplet, which will confine light in different ways. The simplest way how to achieve this, is to use the droplet as whispering-gallery-mode microcavity. What is needed is just a nice spherical shape of the droplet and the refractive index inside to be larger than on the outside. For non-miscible, soft-matter materials, a spherical shape appears naturally because of the surface tension, which tends to reduce the amount of surface for a given volume of material. Different LCs could be used, but the simplest case is the nematic liquid crystal. For anchoring on the droplet interface with the outside material we can choose either planar for bipolar director configuration or homeotropic for radial director configuration. We can again choose the simpler case, so the radial configuration, since it has spherical symmetry.

Once demonstrating the presence of optical modes in LC droplets, the goal was to tune the positions of the resonance frequencies. This could be achieved by external stimuli like electric or magnetic field, temperature, optical field, mechanical deformation, change in surface anchoring and chemical composition. Because of large response of LCs to external stimuli, the tunability of such LC microcavities was expected to be orders of magnitude larger than of solid state materials. However, such large response could also have drawbacks in the sense of resonant frequency and amplitude stability. Instead of tuning the modes by external stimuli, the LC microcavities could also be used as sensors. One of the most interesting applications would be a biosensor, where varying the concentration of a specific compound present in the exterior of the droplet could change the anchoring or directly the internal properties of the LC, such as the pitch. We expected that very sensitive chemical sensors could be realized using liquid-crystal droplets immersed in water containing the target substance.

By having a microcavity and fluorescent dye in the LC microcavity we expected lasing to occur above the lasing threshold when pumping the fluorescent dye with an external source of light. By carefully choosing the configuration of the LC director in the droplet as well as the gain medium, singlemode as well as different multimode lasing is expected to occur. The lasing lines should tune in a very similar way as the modes bellow the lasing threshold.

Further, we wanted to use CLCs to confine light into a droplet. CLCs are known to produce selective Bragg reflection of light on the periodic structure. By making a droplet out of a CLC, the onion Bragg structure was expected to produce omnidirectional PBG and confine the light in the center of the droplet. By introducing a gain material and using external pumping, lasing should be achieved in the same way as in planar CLC structure. Because of nearly spherical symmetric structure, this laser is supposed to emit light in all the directions, making it an omnidirectional coherent point source of light.

To achieve all the above goals, the intention was to use commercially available substances and as simple procedures as possible. In this way, repeatability of the experiments as well as scalability and price of possible future applications could be achieved. To test the microcavities, an upgrade of an existing optical system was planed, by adding a pulsed laser for excitation and a high resolution spectrophotometer with a sensitive EMCCD for the detection of light.

In reality, in the beginning of this research work, the idea was not to use liquid-crystal droplets as microcavities, but to study the inverted system. So to use hard isotropic spheres embedded in a LC as optical microresonators. It has been shown in a number of experiments that particles in nematic liquid crystal can be assembled in a very rich variety of structures such as chains [68], two-dimensional colloidal crystals [69], entangled structures [70], hierarchical self-assembled nematic colloidal superstructures [71], knots [72] and even three-dimensional colloidal crystals [73]. All this structures could be used for a number of photonic applications such as photonic crystals, split ring resonators for metamaterials and optical microcavities. The original idea of this work was to use spherical particles in LC as WGM microresonators. The LC around the microresonators would serve for three different purposes. Firstly, the outside LC can act as a tunable cladding layer and make the microcavities tunable [12,13]. Secondly, the forces in between the particles in LC bind them together enabling self assembly. For example a chain of resonators assembled in this way would work as coupled resonator optical waveguide transferring light from one resonator to the other. Thirdly, by changing the optical properties of the layer of LC in between neighboring microresonators by electric field or laser beam (Figure 9) one could control the coupling between them and make an optical switch.

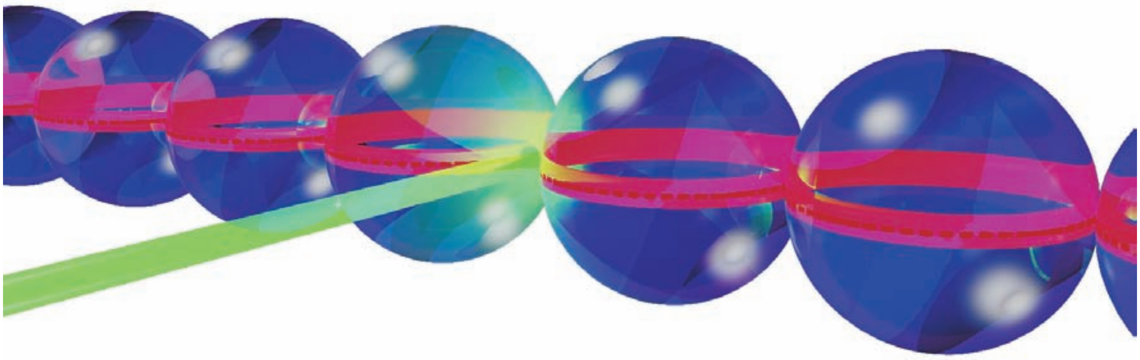

Figure 9: *Proposed CROW structure made from nematic colloids.* A chain of hard microspheres is embedded in a LC that are bound together by elastic forces. Each microsphere supports WGMs that are coupled with neighbouring resonators so that the chain acts as a CROW. A laser beam is used to change the optical properties of the LC between two microresonators achieving all-optical switching.

2 Theoretical background

2.1 Optical microcavities

In this section we will give description of general properties for microcavities, no matter if the microcavity confines light by reflection, total internal reflection or by periodic structure. The most important property of a cavity is the number and frequencies of resonant modes [1]. Usually, the smaller the cavity, less modes will be present. The spacing between two neighboring modes is given by *free spectral range* (FSR). Large FSR is in most cases desirable, since if we have a very large cavity, a huge number of modes will be present and single modes could not be distinguished any more. Another parameter of a microcavity is the *Mode volume.* This is the volume that the electric field of a particular mode occupies in the microcavity. In WGMs the mode volume is typically from several tens to several thousand cubic microns. Smaller the mode volume, higher is the energy density in the cavity, enabling various nonlinear processes and strong light-matter coupling.

2.1.1 Quality factor

The *quality factor* (Q-factor) is a measure of the resonance sharpness relative to its wavelength. Q-factor is defined as the ratio of the energy of light in the resonator to the energy lost per optical cycle

$$Q = \omega \frac{\text{Stored energy}}{\text{Power loss}} \tag{1}$$

where ω is the optical frequency given by $\omega = 2\pi c/\lambda$. The Q-factor can also be expressed as

$$Q = \omega\tau, \tag{2}$$

where τ is the decay time or *photon lifetime.* It can also be easily calculated from the mode spectrum as

$$Q = \frac{\lambda}{\Delta\lambda}, \tag{3}$$

where λ is the central wavelength of the resonance and $\Delta\lambda$ is the full-width at half-maximum (FWHM) of the resonance lineshape.

The overall Q-factor of a WGM microcavity is a sum of many contributions

$$\frac{1}{Q} = \frac{1}{Q_{\text{rad}}} + \frac{1}{Q_{\text{mat}}} + \frac{1}{Q_{\text{ss}}} + \frac{1}{Q_{\text{coupling}}} + \frac{1}{Q_{\text{LC}}}. \tag{4}$$

Radiation loss Q_{rad} is because of curvature of the microcavity. For modes with radial mode number equal to one and cavity diameters larger than approximately 15 µm, the Q_{rad} is usually very large and can be neglected in the sum. Material loss Q_{mat} is caused by absorbtion and scattering in the dielectric medium from which the resonator is made. Surface scattering Q_{ss} is caused by surface roughness. If the resonator is coupled to an external optical device by evanescent field, the reduction of the Q-factor because of coupling

---

[1] For WGMs, the detailed calculation will be given in next section.

(Q_{coupling}), should also be taken into account. And finally, if the resonator is made of liquid crystal, an important factor is contributed to the thermal fluctuations of the LC director (Q_{LC}). The thermal fluctuations change locally and temporarily the refractive index. The light scatters on these local changes of refractive index. As well the mean refractive index of the resonator changes in time. For a small time interval, the resonance is sharp, but its frequency fluctuates with time, so it broadens if averaged over time.

From the decay time, the path length that the light travels around the sphere can be calculated as

$$L = \frac{Qc}{\omega n} \tag{5}$$

and the number of circulations inside a sphere with the radius r is

$$N = \frac{Qc}{2\pi r \omega n}. \tag{6}$$

For high Q-factors already small input power will induce large intensity of the circulating light in resonator. The circulating intensity can be calculated by [1]

$$I = P_{\mathrm{IN}} \left(\frac{\lambda}{2\pi n}\right)\left(\frac{Q}{V}\right) \tag{7}$$

where P_{IN} is the input power and V is the mode volume.

We can calculate the maximum theoretical Q-factor for a resonator made from 5CB. We take into account only Q_{mat}, so the absorbtion of bulk 5CB, that can be found in Ref. [74]. The maximum Q-factors at different wavelengths are

$$\begin{aligned} Q(\lambda = 600\,\mathrm{nm}) &= 5\cdot 10^7 \\ Q(\lambda = 800\,\mathrm{nm}) &> 10^8 \\ Q(\lambda = 1500\,\mathrm{nm}) &= 2\cdot 10^5. \end{aligned} \tag{8}$$

Minimum absorbtion is reached at 800 nm. At shorter wavelengths, especially in blue and UV, the absorbtion is higher like in all the organic materials and in NIR the absorbtion is larger because of molecular vibrations.

2.1.2 Purcell effect

The spontaneous emission of a two level system depends on the properties of the system itself, as well as the environment surrounding the system. The spontaneous decay rate is proportional to the spectral density of the modes at the transition frequency. In vacuum the density of modes is constant, but inside a cavity the density of modes is much higher at resonant frequencies. The modification of the spontaneous emission in a cavity is referred to as *Purcell effect* [1]. At resonant frequencies of the cavity the emission is enhanced by the *Purcell factor*

$$P = \frac{3}{4\pi^2}\left(\frac{\lambda}{n}\right)^3\left(\frac{Q}{V}\right) \tag{9}$$

where λ is the resonance wavelength, n is the refractive index, Q is the Q-factor and V is the mode volume. Furthermore, not only the decay rate is larger, but also the light is directionally emitted to the mode itself, greatly increasing the light intensity of this mode. At frequencies that do not match the resonances, the mode density can be below the density in free space, so the emission is suppressed. The emission of light is also inhibited in photonic bandgap materials. Just as a remark, the Purcell effect can not be explained by classical electrodynamics, but *cavity quantum electrodynamics* (cavity QED) is needed.

An example of the Purcell effect would be a spherical WGM microcavity with embedded fluorescent dye. In the bulk, the dye emits in a broad spectrum and isotropically in all the directions. But inside the microcavity, more light is be emitted at frequencies matching the resonances. This is visible in the spectrum of the light emitted from such a sphere as sharp peaks above the fluorescent background. The light is also preferably emitted in such direction, that it is trapped in the resonant modes. The directionality of the emission is however more difficult to measure.

2.2 Theory of WGMs

To calculate the positions and linewidths of optical modes (WGMs) in spherical dielectric microcavities we have to solve the Maxwell's equations in spherical coordinates with appropriate boundary conditions [11, 75–77]. Calculation of electric field inside and outside a sphere is known for a long time and is mostly used to calculate scattering on small particles [78]. The general solutions are known as *Mie theory* or *Mie scattering.*

2.2.1 WGM frequencies in an isotropic sphere

Here we are going to calculate solutions for electric and magnetic field in an isotropic dielectric sphere. The derivation is summarized from Ref. [78].

We start with source-free *Maxwell's equations* for isotropic medium

$$\begin{aligned}\nabla\cdot\mathbf{E} &= 0 &(10)\\ \nabla\times\mathbf{E} &= -\frac{\partial\mathbf{B}}{\partial t} &(11)\\ \nabla\cdot\mathbf{B} &= 0 &(12)\\ \nabla\times\mathbf{B} &= \mu\mu_0\varepsilon\varepsilon_0\frac{\partial\mathbf{E}}{\partial t}. &(13)\end{aligned}$$

Taking the curl of equations (11) and (13) gives

$$\begin{aligned}\nabla\times\nabla\times\mathbf{E} &= -\frac{\partial}{\partial t}\nabla\times\mathbf{B} = -\mu\mu_0\varepsilon\varepsilon_0\frac{\partial^2\mathbf{E}}{\partial t^2} &(14)\\ \nabla\times\nabla\times\mathbf{B} &= \mu\mu_0\varepsilon\varepsilon_0\frac{\partial}{\partial t}\nabla\times\mathbf{E} = -\mu\mu_0\varepsilon\varepsilon_0\frac{\partial^2\mathbf{B}}{\partial t^2}. &(15)\end{aligned}$$

By using the vector identity

$$\nabla\times(\nabla\times\mathbf{V}) = \nabla(\nabla\cdot\mathbf{V}) - \nabla^2\mathbf{V} \tag{16}$$

and $c = \frac{1}{\sqrt{\mu\mu_0\varepsilon\varepsilon_0}}$ it gives the wave equations for electric and magnetic field

$$\frac{\partial^2\mathbf{E}}{\partial t^2} - c^2\nabla^2\mathbf{E} = 0 \qquad \frac{\partial^2\mathbf{B}}{\partial t^2} - c^2\nabla^2\mathbf{B} = 0. \tag{17}$$

By using oscillating electric field in the form of $\mathbf{E} = \mathbf{E}_0 e^{i(\mathbf{k}\cdot\mathbf{r}-\omega t)}$ and $k = \frac{\omega}{c}$ we can rewrite the wave equation in the form of *Helmholtz equation*

$$k^2\mathbf{E} + \nabla^2\mathbf{E} = 0 \qquad k^2\mathbf{B} + \nabla^2\mathbf{B} = 0. \tag{18}$$

By using a scalar function ψ and a constant vector $\mathbf{c}$ we construct a vector function $\mathbf{M}$ that has zero divergence, such that

$$\mathbf{M} = \nabla\times(\mathbf{c}\psi). \tag{19}$$

It can be shown [78] that if **M** satisfies the vector Helmholtz equation and ψ is a solution to the scalar Helmholtz equation

$$k^2\psi + \nabla^2\psi = 0. \tag{20}$$

We can construct another vector function **N** which also satisfies the vector Helmholtz equation and has zero divergence, so that

$$\mathbf{N} = \frac{\nabla \times \mathbf{M}}{k}. \tag{21}$$

and also

$$\nabla \times \mathbf{N} = k\mathbf{M}. \tag{22}$$

The scalar function ψ is called *generating function* for *the vector harmonics* **M** and **N**. Both **M** and **N** have all the all the required properties of an electromagnetic filed. They satisfy the vector wave equation, they have zero divergence and the curl of **M** is proportional to **N** and the curl of **N** is proportional to **M**. Therefore instead of solving the vector wave equation we can solve the scalar wave equation, which is much more simple.

The generating function should be chosen so that it fits the symmetry of our problem. Since we want to calculate the fields in a sphere we choose functions ψ that satisfy the wave equation in spherical coordinates and for the vector **c** we choose the radius vector **r**. We have now to solve scalar wave equation (20) in spherical coordinates:

$$\frac{1}{r^2}\frac{\partial}{\partial r}\left(r^2\frac{\partial\psi}{\partial r}\right) + \frac{1}{r^2\sin\theta}\frac{\partial}{\partial\theta}\left(\sin\theta\frac{\partial\psi}{\partial\theta}\right) + \frac{1}{r^2\sin^2\theta}\frac{\partial^2\psi}{\partial\phi^2} + k^2\psi = 0 \tag{23}$$

The variables can be separated and the solution can be written as

$$\psi(r,\theta,\phi) = R(r)\Theta(\theta)\Phi(\phi) \tag{24}$$

and the separated equations are

$$\frac{d^2\Phi}{d\phi^2} + m^2\Phi = 0 \tag{25}$$

$$\frac{1}{\sin\theta}\frac{d}{d\theta}\left(\sin\theta\frac{d\Theta}{d\theta}\right) + \left(l(l+1) - \frac{m^2}{\sin^2\theta}\right)\Theta = 0 \tag{26}$$

$$\frac{d}{dr}\left(r^2\frac{dR}{dr}\right) + (k^2r^2 - l(l+1))R = 0 \tag{27}$$

The solutions to (25) are

$$\Phi = \frac{1}{\sqrt{2\pi}}e^{\pm im\phi} \tag{28}$$

and the solutions to (26) are *associated Legendre functions of the first kind*

$$\Theta = P_l^m(cos\theta) \tag{29}$$

where for each polar mode number l, the allowed azimuthal mode numbers m are in the range of $-l < m < l$. The two above solutions for ϕ and θ can be also combined, so we get spherical harmonics

$$\Theta(\theta)\Phi(\phi) = N\, e^{im\phi}\, P_l^m(\cos\theta) = Y_l^m(\theta,\phi) \tag{30}$$

where N is a normalization factor.

The solutions to (27) are *spherical Bessel functions of first and second kin*d

$$j_l(kr) = \sqrt{\frac{\pi}{2kr}}J_{l+1/2}(kr) \tag{31}$$

$$y_l(kr) = \sqrt{\frac{\pi}{2kr}} Y_{l+1/2}(kr) \tag{32}$$

where J and Y are ordinary Bessel functions.

The whole solution is now equal to

$$\psi_{lm} = Y_l^m(\theta, \phi) z_l(kr) \tag{33}$$

where z_l is j_l or y_l or any linear combination of the two. Two special linear combinations are known as *spherical Bessel functions of the third kind*, also called *spherical Hankel functions*

$$h_l^{(1)}(kr) = j_l(kr) + i y_l(kr) \tag{34}$$

$$h_l^{(2)}(kr) = j_l(kr) - i y_l(kr). \tag{35}$$

The optical modes in the sphere can be uniquely characterized by a set of three mode numbers, the *radial mode number* q, the *polar mode number* l, the *azimuthal mode number* m and the *polarization* p. The radial mode number indicates the number of maxima in the radial intensity distribution in the sphere, the polar mode number gives the number of wavelengths for one circulation of the light and the azimuthal mode number indicates the inclination of the circular orbit of the light in respect to our reference frame. In Figure 10 there are represented the electric field intensity distributions for modes with the same polar mode number, but different radial mode numbers.

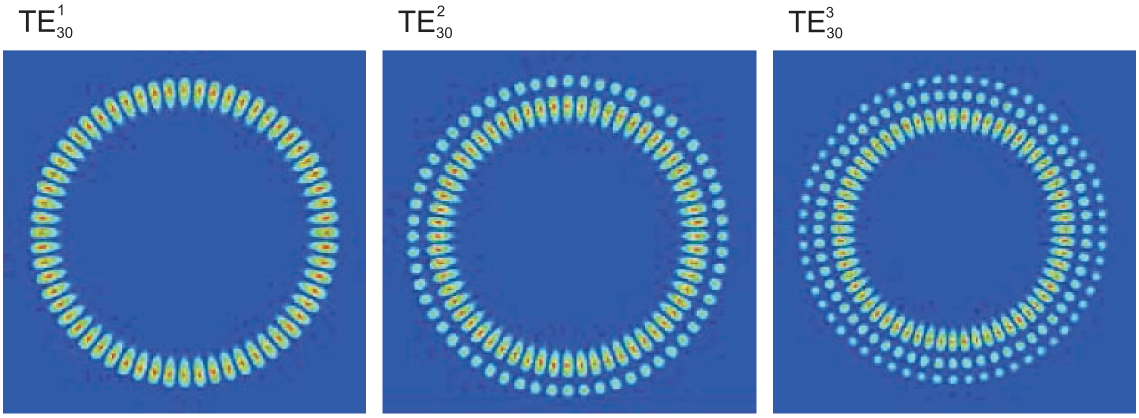

Figure 10: *Electric field intensity distributions in the equatorial plane of the sphere for TE WGMs with* $l = m = 30$ *and* $n = 1, 2$ *and* 3. It can be seen that for all the three cases the number of maxima in tangential direction is equal to 60, which corresponds to 30 wavelengths, so also to the polar mode number. In the radial direction the number of maxima corresponds to the radial mode number. Reprinted with permission from [76].

Because the Bessel function of second kind is singular at the origin, only first kind function is retained inside of the sphere. On the outside, the Hankel functions are used, $h_l^{(1)}$ corresponds to outward propagating spherical wave and $h_l^{(2)}$ corresponds to inwards propagating wave. We are interested just in leaking of the modes, so we keep just $h_l^{(1)}$. From radial functions, electric and magnetic fields can be written. At the surface of the sphere ($r = a$) the inner fields must match the exterior ones giving the *characteristic equations*

$$\frac{[n_r x j_l(n_r x)]'}{j_l(n_r x)} = \frac{[x h_l^{(1)}(x)]'}{h_l^{(1)}(x)} \quad \text{for TE} \tag{36}$$

$$\frac{[n_r j_l(n_r x)]'}{m^2 j_l(n_r x)} = \frac{[x h_l^{(1)}(x)]'}{h_l^{(1)}(x)} \quad \text{for TM} \tag{37}$$

where $n_r = n_s/n_a$ is the relative refractive index between the interior and the surrounding of the sphere, $x = ka$ is the size parameter, where $k = \frac{\omega}{c} n_a$ is the wavenumber in the surrounding medium. The primes denote differentiations with respect to the argument. Solving these two equations numerically, gives the exact solutions for WGMs. For each polar mode number l there are a number of solutions, that correspond to different radial mode numbers q. The solutions for x can not be real, so that the eigenfrequencies ω_{ql} are complex. This means that the modes are leaky and that the resonances are not infinitely sharp. The real part of ω_{ql} is the central frequency of the resonance and the imaginary part represents its width. The Q-factor can be calculated as

$$Q = \frac{\mathrm{Re}(\omega_{ql})}{2|\mathrm{Im}(\omega_{ql})|}. \tag{38}$$

2.2.2 Approximate solutions

Resonant WGM frequencies for small radial mode numbers q can be accurately computed using asymptotic expansion in powers of $(l/2)^{-1/3}$ [79, 80]

$$n_s ka = l - \alpha_q \left(\frac{l}{2}\right)^{1/3} - \frac{\chi n_r}{\sqrt{n_r^2 - 1}} + \frac{3\alpha_q^2}{20}\left(\frac{l}{2}\right)^{-1/3} - \frac{\alpha_q n_r \chi (2\chi^2 - 3n_r^2)}{6(n_r^2 - 1)^{3/2}}\left(\frac{l}{2}\right)^{-2/3} + O(l^{-1}) \tag{39}$$

where

$$\chi = \begin{cases} 1 & \text{for TE modes} \\ 1/n_r^2 & \text{for TM modes} \end{cases}$$

and a is the radius of the sphere, k is wavenumber, $l \gg 1$ and $q = 1, 2, 3, ...$ are mode numbers, α_q are negative q-th zeroes of the Airy function and $n_r = n_s/n_a$ is relative refractive index, where n_s is the refractive index of the sphere and n_a is the index of the surrounding medium.

For even better accuracy, additional terms can be added to the expansion. However, for typical microresonators used in this work ($l > 100$ and $q < 4$) the error using (39) is less than 10^{-4}. For a mode at 600 nm this means 0.06 nm which is the same as the resolution of the spectrometer used in this work.

For a really simple approximation and to understand physics behind WGMs, just the first term l can be considered. The equation is in this case reduced to $nka \approx l$. Using $k = 2\pi/\lambda$ we get

$$2\pi a n \approx l\lambda. \tag{40}$$

Left side of the equation is the circumference multiplied by the refractive index, which is the optical path around the droplet. The optical path is approximately equal to the integer number of wavelengths around the sphere. This expression is of course valid just for first radial modes ($q = 1$). For $l = 100$ the relative error that we make by using (40), is around 10%, but for larger droplets with $l = 1000$ the error is just 0.2%, so in many cases is useful for making rough estimations.

Instead of positions of resonant frequencies also approximate mode separation versus the two indices l and q up to $O(l^{-2})$ can be given as

$$\frac{1}{\omega}\frac{\partial \omega}{\partial l} \approx l^{-1}\left[1 + \frac{\alpha_q}{6}\left(\frac{l}{2}\right)^{-2/3}\right] \tag{41}$$

$$\frac{1}{\omega}\frac{\partial \omega}{\partial q} \approx \frac{\pi}{2\sqrt{-\alpha_q}}\left(\frac{l}{2}\right)^{-2/3}\left[1 + \frac{\alpha_q}{20}\left(\frac{l}{2}\right)^{-2/3}\right] \tag{42}$$

The Q-factor can be as well approximately calculated [79] using

$$Q = \frac{\chi(n_r^2 - 1)}{2} \left[\left(\frac{2u_0}{\nu} \right)^{1/2} - \frac{1}{4u_0} \right]^{-1} e^{\frac{4u_0}{3} \left(\frac{2u_0}{\nu} \right)^{1/2}} \tag{43}$$

where

$$\chi = \begin{cases} 1 & \text{for TE modes} \\ 1/n_r^2 & \text{for TM modes} \end{cases}$$

and n_r is relative refractive index, u_0 is the value of $u = \nu - x$ at the resonance position, $\nu = l + 1/2$ and $x = \frac{2\pi r}{\lambda}$ is the size parameter. However, this approximation is not good for very small or very large polar mode numbers l and can deviate from the correct solution by more than an order of magnitude.

An important characteristics of the WGMs is that the light is not entirely confined to the sphere. Outside the sphere the light intensity exponentially decreases with distance from the surface forming the *evanescent field*. This phenomena is crucial for many applications of WGMs. Evanescent field is typically extending around one wavelength from the surface of the sphere (Figure 11) and is non-radiative.

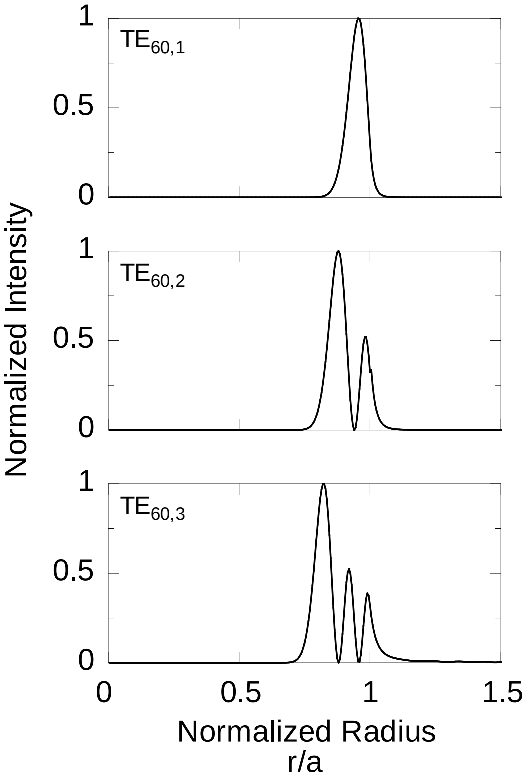

Figure 11: *Radial light intensity for TE WGMs with $l = m = 60$ and $n = 1, 2$ and 3.* Note that the light intensity is nonzero also outside the sphere. Reprinted with permission from [76].

2.2.3 Non-spherical whispering-gallery cavity

In completely spherical cavities the modes with different azimuthal mode numbers m are degenerate. This is because in the case of spherical symmetry it is not important in which plane the light is circulating. As soon as the cavity becomes non-spherical, the modes are not degenerate any more. From the mode splitting one can calculate the non-sphericity of the cavity. For a spheroid we can approximately calculate the frequencies of WGMs using the asymptotic expansion [81]

$$\begin{aligned} n_ska &= l-\alpha_q\left(\frac{l}{2}\right)^{1/3}+\frac{2g(a-b)+a}{2b}-\frac{\chi n_r}{\sqrt{n_r^2-1}}+\frac{3\alpha_q^2}{20}\left(\frac{l}{2}\right)^{-1/3} \\ &\quad -\frac{\alpha_q}{12}\left(\frac{2g(a^3-b^3)+a^3}{b^3}+\frac{2n_r\chi(2\chi^2-3n_r^2)}{(n_r^2-1)^{3/2}}\right)\left(\frac{l}{2}\right)^{-2/3}+O(l^{-1}) \end{aligned} \tag{44}$$

where

$$\chi=\begin{cases}1 & \text{for TE modes}\\ 1/n_r^2 & \text{for TM modes}\end{cases}$$

and a and b are equatorial and polar semiaxes of the spheroid, k is wavenumber, $l \gg 1$, $g = l - |m| = 0, 1, 2, ...$ and $q = 1, 2, 3, ...$ are mode numbers, α_q are negative q-th zeroes of the Airy function and $n_r = n_s/n_a$ is relative refractive index, where n_s is the refractive index of the spheroid and n_a is the index of the surrounding medium. The equation reduces to the spherical case (39) if $a = b$. And the mode separation versus index m up to $O(l^{-2})$ is

$$\frac{1}{\omega}\frac{\partial\omega}{\partial m}\approx l^{-1}\frac{b-a}{b}\left[1+\frac{\alpha_q}{12}\frac{(b-a)(a+2b)}{b^2}\left(\frac{l}{2}\right)^{-2/3}\right]. \tag{45}$$

2.2.4 WGM frequencies in an anisotropic sphere

To find frequencies of WGMs in a nematic droplet, the derivation from Section 2.2.1 has to be performed for an anisotropic sphere where the optical axis is always in the radial direction. In the radial direction we have extraordinary dielectric permittivity ε_e and in the tangential direction we have ordinary dielectric permittivity ε_o. The differential equations for the radial dependance of the electric and magnetic field for TE and TM modes are [82]

$$\frac{d}{dr}\left(r^2\frac{dR^{(1)}(r)}{dr}\right)+(k^2r^2-l(l+1))R^{(1)}(r)=0 \tag{46}$$

and

$$\frac{d}{dr}\left(r^2\frac{dR^{(1)}(r)}{dr}\right)+(k^2r^2-l(l+1)\frac{\varepsilon_o}{\varepsilon_e})R^{(1)}(r)=0. \tag{47}$$

For $\varepsilon_e = \varepsilon_o$ both equations are the same and are equal for the isotropic case (27). Therefore, the solutions to (46) are the same as in isotropic case, so spherical Bessel ($j_l(kr)$) and spherical Hankel functions ($h_l(kr)$). For (47) the solutions [83] are also spherical Bessel ($j_{\tilde{l}}(kr)$) and spherical Hankel functions ($h_{\tilde{l}}(kr)$), but with a non-integer order

$$\tilde{l}(l)=\frac{1}{2}\left[-1+\sqrt{1+4\left(\frac{n_o}{n_e}\right)^2 l(l+1)}\right]. \tag{48}$$

Note that for $n_o = n_e$, $\tilde{l}(l) = l$. Apart from the non-integer order, the characteristic equations (36) and (37) are the same as for the isotropic case, where $n_r = n_o/n_s$. It is interesting, that the equation for TE modes is dependent only on the ordinary refractive index, whereas TM modes couple both ordinary and extraordinary refractive indices.

2.2.5 Excitation of WGMs

2.2.5.1 Evanescent field coupling

We can excite WGMs by coupling the evanescent field of the sphere with an external evanescent field. The external evanescent field can be made in two main ways. The first method is by total internal reflection of light in a prism. The second source of evanescent field can be a thin optical fiber, typically several micrometers in diameter. In both cases we need to mechanically bring the microspehere in close contact with the prism or fiber and typical distance between the two must be under 1 µm for visible wavelengths. Single longitudinal mode tunable laser is used as a light source. By selecting the wavelength that corresponds the to one WGM is it possible to selectively excite single WGMs. Usually we measure the transmission of an optical fiber coupled to a microresonator as a function of wavelength. At the wavelengths that correspond to WGMs the light energy is flowing into the sphere where it is dissipating, reducing the transmission through the fiber at that frequency.

2.2.5.2 Fluorescence

A more simple way of exciting WGMs is fluorescence. For example glass microspheres doped with rare earth elements or microspheres made from polymer material mixed with a fluorescent dye are used. Shorter wavelength light is used to excite the fluorescence and the fluorescent substance is emitting light in a broad spectrum at longer wavelengths and in all the directions. Because of Purcell effect (Section 2.1.2) a larger portion of light is trapped to the optical modes, which can be seen as peaks in the fluorescent spectrum. To further increase the amount of coupled light, it is better not to illuminate the whole microsphere, but just with a tightly focused beam near the edge of the sphere, where the modes are located. In the same way, having the fluorescent substance near the surface is a more efficient way of exiting WGMs, because the light captured inside the sphere is circumnavigating just below the surface. The fluorescent substance can also be on the surface outside the microsphere. In this case the WGMs are excited through the coupling between the fluorescent substance and the WGMs trough evanescent field.

2.3 Theory of lasing

Laser is a special light source with high temporal and spatial coherence that uses stimulated emission to achieve these characteristics. LASER is an acronym for *Light Amplification by Stimulated Emission of Radiation.* A laser is made of a gain medium that amplifies the light and a resonant cavity that enables the recirculation of light through the gain medium. To understand the optical amplification [84, 85] we have to look at the levels in the gain material, transition probabilities and the optical loses in the laser cavity.

Suppose that we have a two level system ($|1\rangle$ and $|2\rangle$), the lower level having energy E_1 and the upper having energy equal to E_2. The number of electrons in the two levels is N_1 and N_2, respectively, with the total number of electrons $N = N_1 + N_2$ and energy of transition $E_2 - E_1 = h\nu$. In thermal equilibrium the ratio of the populations of these two levels is

$$\frac{N_2}{N_1} = e^{(E_1 - E_2)/k_B T}. \tag{49}$$

At zero temperature all the electrons are in $|1\rangle$, while at infinite temperature both levels are equally occupied. As we will se later, for optical gain to be present, *population inversion* ($N_2 > N_1$) is necessary. To achieve population inversion at least a three level system is required ($|1\rangle$, $|2\rangle$ and $|3\rangle$). The electrons are pumped from $|1\rangle$ to $|3\rangle$. Population inversion is achieved between $|1\rangle$ and $|2\rangle$ if the transition from $|2\rangle$ and $|3\rangle$ is faster or between $|2\rangle$ and $|3\rangle$ if the transition from $|1\rangle$ and $|2\rangle$ is faster.

To describe the probabilities of transitions in a two level system we introduce so called *Einstein coefficients.* Three processes are possible in a two level system. If the system is in high energy state and is perturbated by an electric field of frequency ω it may emit an photon, that has the same frequency and in the same phase as the external field. This process is called *stimulated emission.* The rate of stimulated emission is

$$\frac{\partial N_1}{\partial t} = B_{21} u(\omega) g(\omega) N_2 \tag{50}$$

where B_{21} is the *Einstein B coefficient*, $u(\omega)$ is the spectral energy density and $g(\omega)$ is the lineshape of the transition. The transition rate is proportional to the number of excited states and the density of incident photons. The second process is absorption, the rate is equal to

$$\frac{\partial N_2}{\partial t} = B_{12} u(\omega) g(\omega) N_1. \tag{51}$$

The rate is proportional to the number of ground states and again density of the incident photons. The third process is spontaneous emission which is not dependent on the density of the incident photons. The rate is given by *Einstein A coefficient* as

$$\frac{\partial N_2}{\partial t} = -A_{21} N_2. \tag{52}$$

It can be shown [84] that

$$B_{12} = B_{21} = B \tag{53}$$

and

$$\frac{A}{B} = \frac{\hbar \omega^3}{\pi^2 c^3}. \tag{54}$$

For the light with photon flux density ϕ propagating inside a gain material, the following equation can be written [85]

$$\frac{d\phi}{dz} = \frac{\gamma_0 \phi}{1 + \phi/\phi_0}, \tag{55}$$

where γ_0 is *small signal gain coefficient* and ϕ_0 is *saturation photon-flux density* that is connected to Einstein coefficients by

$$\phi_0 \propto \frac{A}{B}. \tag{56}$$

For the laser resonator in equilibrium, the total energy W in the resonator should be constant. The energy gain for propagation of light back and forth through the resonator (path length $2L$, where L is the resonator length) is

$$\Delta W_{\text{gain}} = \frac{\gamma_0 W 2L}{1 + W/W_S}, \tag{57}$$

where W_S is the saturation energy, that is connected to the saturation photon-flux density. On the other hand, the loses are

$$\Delta W_{\text{loss}} = -[\alpha_0 2L + (1 - R_1) + (1 - R_2)]W = -2\Lambda W, \tag{58}$$

where R_1 and R_2 are reflectivities of the two mirrors and α_0 is the absorbtion coefficient. In equilibrium the losses should be the same as the gain, so

$$2\Lambda W = \frac{\gamma_0 W 2L}{1 + W/W_S} \tag{59}$$

and therefore

$$W = \left(\frac{\gamma_0 L}{\Lambda} - 1 \right) W_S. \tag{60}$$

The threshold of the laser is at $\gamma_0 L/\Lambda = 1$. From that point on the energy in the laser is linearly increasing with gain. The power output, if $R_1 = 1$ and $R_2 < 1$, is

$$P = (1 - R_2) \frac{c}{2L} W. \tag{61}$$

2.4 Bragg microcavities

The same as for WGMs, to get the modes in a spherical Bragg microcavity, we have to solve Helmholtz equation in spherical coordinates. The derivation is summarized from Ref. [86].

Ingoing and outgoing light can be expressed as spherical waves by using spherical harmonics. For TE wave polarization the electric and magnetic fields of a spherical wave with frequency ω can be written as

$$\begin{aligned}
\mathbf{E} &= -\mu k_0 \left(\frac{m}{\sin\theta} P_l^{|m|}(\cos\theta)\mathbf{e}_\theta + i\frac{\partial}{\partial\theta} P_l^{|m|}(\cos\theta)\mathbf{e}_\varphi \right) V(r) e^{im\varphi} \quad \text{and} \qquad (62)\\
\mathbf{H} &= \left[\frac{l(l+1)}{r} V(r) P_l^{|m|}(\cos\theta)\mathbf{e}_r + \left(\frac{\partial}{\partial\theta} P_l^{|m|}(\cos\theta)\mathbf{e}_\theta \frac{im}{\sin\theta} P_l^{|m|}(\cos\theta)\mathbf{e}_\varphi \right) \frac{1}{r}\frac{\partial}{\partial r}(rV(r)) \right] e^{im\varphi},
\end{aligned}$$

where $V(r) = Ah_l^{(1)}(kr) + Bh_l^{(2)}(kr)$ are spherical Hankel functions, A and B are constants and $k = n\omega/c$ where n is the refractive index of the medium the spherical wave is propagating through. Orbital momentum is equal to l and its projection m can be in the interval from $-l$ to l. An orbital momentum $l = 0$ corresponds to a fully spherically symmetric electromagnetic wave, which does not exist. Similarly, also fields for a TM mode can be written.

To obtain the spatial distribution of an electromagnetic field in a layered structure, the *transfer matrix technique* is used. In this way also transmission and reflection coefficients can be calculated. For planar Bragg reflector, to obtain maximum reflection at the frequency ω_{BR}, the layers should have the thickness corresponding to quarter wavelength of the light. The thicknesses (d_1 and d_2) for the two layers with refractive indexes n_1 and n_2 must satisfy the relation $d_{1,2} = \pi c/2\omega_{\mathrm{BR}} n_{1,2}$. However, spherical Bragg structure that optimally reflects light is non-periodic [37]. This directly reflects the non-periodicity of the outgoing spherical Henkel functions. The layers should therefore be quarter-wavelength thick, but corresponding to the actual wavelength, that changes with the distance from the center. At larger distances from the center the spherical Henkel functions become periodic, so the wavelength becomes constant and equal to that of a planar wave. The derivation of the reflection coefficient (r_b) of the spherical Bragg structure can be found in Ref. [86].

Depending on the structure of the cavity we have three basic types of spherical Bragg microcavities. The simplest is the structure where the periodic structure fills all the volume of the spherical cavity (Figure 12a). In the second case there is a defect in the center (Figure 12b). This is a sphere, typically half wavelength or larger in diameter that can have the same or different refractive index than the layers. The third type of Bragg microcavity has a shell defect, that is the case when one of the spherical layers is thicker (Figure 12c) or has different refractive index. Modes similar to WGMs are confined to this layer. We will not be interested in this last type. All this structures also have equivalents in 2D case, that are referred to as circular, disk and ring Bragg microcavities, respectively [87].

In the case of microcavity with the central defect, the optical modes are confined into this central region, with the intensity exponentially decaying into the surrounding periodic structure. The resonant frequencies lie in the PBG frequency region, and are therefore called *bandgap modes* or *defect modes.* If there is no defect at the center, the modes in such cavity are delocalized and occupy much of the volume of the cavity. Their frequencies lie on the edge of the bandgap or near the bandedge, so they are called *bandedge modes.*

For the Bragg microcavity with the defect at the center, the electromagnetic field in the core can be expressed as the sum of incoming and outgoing waves. In stationary case the amplitude of both waves in the core should be equal and finite in the center. Therefore, the field in the core is described with spherical Bessel functions. On the other hand, the at the interface of the defect, the amplitude of the outgoing wave should be equal to the amplitude of the outgoing wave from the layered structure multiplied by the reflection coefficient r_b.

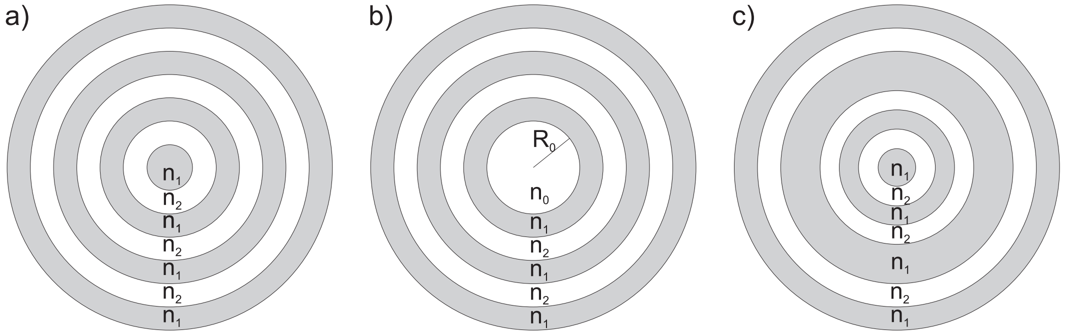

Figure 12: *Three basic types of spherical Bragg microcavities.* a) A normal spherical Bragg microcavity, b) with a defect in the center and c) with a shell defect.

So, the equation for the eigenmodes of a spherical Bragg microcavity with the defect radius of R_0 is

$$r_b h_l^{(1)}(kR_0) = h_l^{(2)}(kR_0). \tag{63}$$

This equation gives solutions for both TE and TM modes, however, the reflection coefficient r_b is different for each polarization. If r_b is close to unity, that is in the case of low absorbtion (high Q-factor) and the core diameter is equal or larger than the wavelength of the light, the frequencies of the TE modes can be approximated as

$$\omega = \frac{b + \pi(2N + l + 1)}{b/\omega_b + 2n_0R_0/c} \tag{64}$$

and for TM modes as

$$\omega = \frac{b + \pi(2N + l)}{b/\omega_b + 2n_0R_0/c} \tag{65}$$

where ω_b is the Bragg frequency for the spherical Bragg structure, $b = \pi n_1 n_2/(n_0(n_2 - n_1))$ and N is an integer. For smaller core diameters we have to solve the equation (63).

All the TE and TM modes have zero electric field in the center of the cavity, except for TM mode with $l = 1$ and $m = 0$ (Figure 13a). For this case, the electric field is oriented along the z-axis and the maximum is achieved in the polar areas in the low index layer, just outside the core. For TE mode with $l = 1$ and $m = 0$ (Figure 13b) the field has torroidal structure with zero electric field in the center. For both TE and TM polarizations with $l = 0$ and $m = 0$ the far field pattern corresponds to the radiation of a dipole oscillating along the z-direction.

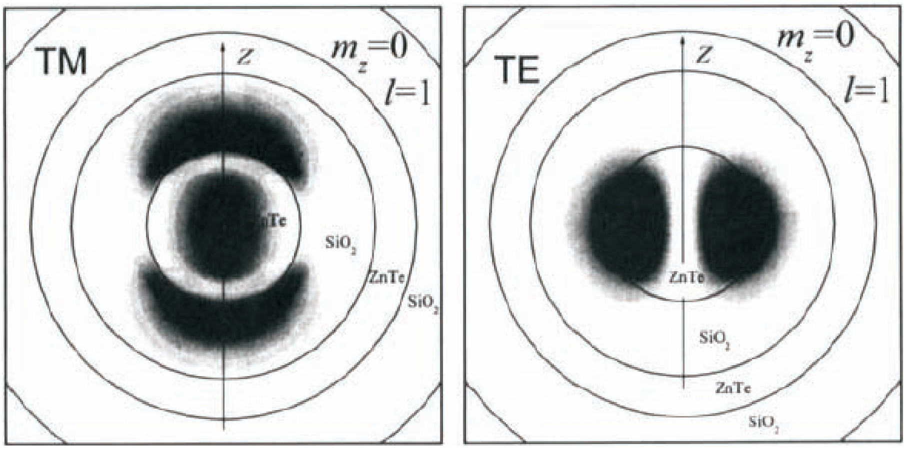

Figure 13: *Intensities for two Bragg defect modes.* TE and TM magnitude of field squared for $l = 1$ and $m = 0$ in cross section of a spherical Bragg cavity with the central defect. The layers correspond to a spherical quarter-wavelength spherical reflector and the core diameter is approximately half the wavelength. Reprinted with permission from [86].

2.5 Liquid crystals

2.5.1 Introduction to liquid crystals

In nature there are three basic states of matter: solid, liquid and gas. However, there are substances, that have several phases between solid and liquid state. Their symmetry properties are in between solids and liquids. This kind of substances are therefore called *liquid crystals* (LC). Their molecules diffuse like molecules in liquids but maintain some degree of orientational order and sometimes also positional order. The order brings several anisotropies like: birefringence, anisotropic viscosity and transfer of statical torques. The properties of LCs derive from the shape of the molecules. They are elongated in one direction or in the shape of a disk.

2.5.1.1 Nematic liquid crystals

In nematic liquid crystal the molecules do not have long range positional order but they have orientational order (Figure 14). This means that in average all the molecules point in the same direction. This direction is characterized by a vector of unit length $\mathbf{n}$ called the *director*. Directions $\mathbf{n}$ and $-\mathbf{n}$ are equivalent. The direction of the director in bulk is arbitrary or it is defined by an external field. In confined systems the director is defined by the boundary conditions at the interface between the LC and another substance.

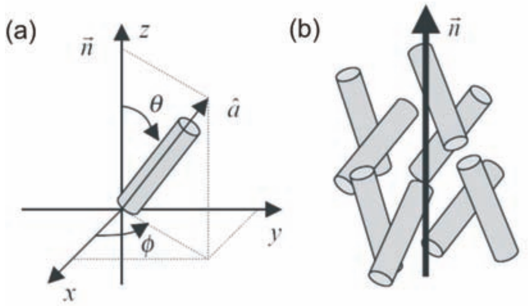

Figure 14: *LC molecule orientation.* a) Deviation of the LC molecule direction from the director and b) orientational disorder of LC molecules. Reprinted with permission from [88].

2.5.1.2 Order parameter

With the director we described the mean direction of the LC molecules. Now we want to characterize how good is the orientation of the molecules in that direction. For that purpose we construct a scalar quantity called *order parameter*, defined as

$$S = \frac{1}{2} < (3\cos^2\theta - 1) >= \int f(\theta)\frac{1}{2}(3\cos^2\theta - 1)d\Omega. \tag{66}$$

where θ is the angle between the director and the long axis of the molecules (Figure 14a). In the isotropic phase it is equal to zero, in the crystal phase equal to one, whereas in the nematic phase its value is usually in between 0.3 and 0.7

2.5.1.3 Elastic properties of liquid crystals

In the nematic phase the director is uniform in space. However, usually because of confinement and external fields the director varies spatially. This deformation of LC costs energy and therefore the elastic energy density is equal to

$$f_{elast} = \frac{1}{2}K_{11}(\nabla \cdot \mathbf{n})^2 + \frac{1}{2}K_{22}(\mathbf{n} \cdot \nabla \times \mathbf{n})^2 + \frac{1}{2}K_{33}(\mathbf{n} \times \nabla \times \mathbf{n})^2. \tag{67}$$

This elastic energy is called also *Oseen-Frank energy*, and K_{11}, K_{22} and K_{33} are referred to as the *Frank elastic constants*. For 5CB at room temperature the values are $K_{11} = 0.64 \times 10^{-11}$ N, $K_{22} = 0.3 \times 10^{-11}$ N and $K_{33} = 1 \times 10^{-11}$ N.

2.5.1.4 Electric field effect in liquid crystals

Liquid crystals are important from the application stand point of view because of their large response to an external electric field. With just few volts applied to a LC cell, the reorientation of the LC molecules and change of the optical properties of the cell can be achieved. Electric field induces electric dipole in LC molecules, which is dependent on the orientation of the molecules, since they posses dielectric anisotropy. We define $\chi_{\parallel}$ as the dielectric susceptibility parallel to the long axes of the molecule, and $\chi_{\perp}$ as the dielectric susceptibility perpendicular to this direction. The anisotropy of the dielectric susceptibility is then $\Delta\chi = \chi_{\parallel} - \chi_{\perp}$ and the anisotropy of the dielectric constant is $\Delta\epsilon = \epsilon_{\parallel} - \epsilon_{\perp} = (1 + \chi_{\parallel}) - (1 + \chi_{\perp}) = \chi_{\parallel} - \chi_{\perp} = \Delta\chi$. The induced polarization for an arbitrary angle between the electric field and the nematic director is given by

$$\mathbf{P} = \epsilon_0\chi_{\parallel}(\mathbf{E} \cdot \mathbf{n})\mathbf{n} + \epsilon_0\chi_{\perp}[\mathbf{E} - (\mathbf{E} \cdot \mathbf{n})\mathbf{n}] = \epsilon_0[\chi_{\perp}\mathbf{E} + \Delta\chi(\mathbf{E} \cdot \mathbf{n})\mathbf{n}]. \tag{68}$$

The density of the electric free energy is calculated as

$$f_{elec} = -\frac{1}{2}\mathbf{P} \cdot \mathbf{E} = -\frac{1}{2}\epsilon_0[\chi_{\perp}\mathbf{E} + \Delta\chi(\mathbf{E} \cdot \mathbf{n})\mathbf{n}] \cdot \mathbf{E} = -\frac{1}{2}\epsilon_0\chi_{\perp}E^2 - \frac{1}{2}\epsilon_0\Delta\epsilon(\mathbf{E} \cdot \mathbf{n})^2. \tag{69}$$

This is an additional contribution to the total free energy of the LC (67). We can neglect the first term, since it is not dependent on the orientation of the nematic director. The director will orient so that the total free energy will be minimal. If $\Delta\epsilon > 0$ the molecules tend to align along the electric field and if $\Delta\epsilon < 0$ the molecules tend align in the perpendicular direction. Most nematic LCs have positive dielectric constant, since the polarizability is larger along the long axis of the molecule.

2.5.1.5 Change of the refractive indices of liquid crystals by temperature

In the nematic liquid crystal phase the bulk refractive indices n_e and n_o correspond to the dielectric constants along and perpendicular to the nematic director. We can define birefringence Δn that is the difference between the two indices

$$\Delta n = n_e - n_o. \tag{70}$$

At high temperature, when the LC is in the isotropic phase, the molecules do not have any rotational order. In this case the liquid crystal is optically isotropic and the average refractive index is

$$\langle n \rangle = \frac{n_e + 2n_o}{3}. \tag{71}$$

Similar to the isotropic liquids, the average refractive index of LCs depends on the density of the material and decreases with the increasing temperature, since also the density decreases. The average refractive index in the isotropic, as well as in the nematic phase can be approximated as

$$\langle n \rangle = A - BT, \tag{72}$$

where A and B are the material parameters. In the nematic phase the molecules are in average oriented along the director direction, but are fluctuating around this average direction. The degree of the orientational order is given by the order parameter S that is strongly temperature dependent and decreases when approaching the isotropic phase. The bulk refractive indices are also dependent on the amount of orientational fluctuations and therefore on temperature [89]. The birefringence decreases with temperature and reaches zero in the isotropic phase. It is described by the Haller approximation

$$\Delta n(T) = (\Delta n)_0 \left(1 - \frac{T}{T_C}\right)^{\beta}, \tag{73}$$

where $(\Delta n)_0$ is the birefringence in the crystalline state with perfect orientational order at $T = 0$, T_C is the isotropic-nematic phase transition temperature and β is a material constant. Using (70), (71), (72) and (73) the ordinary and extraordinary refractive indices are

$$n_o(T) = A - BT - \frac{(\Delta n)_0}{3} \left(1 - \frac{T}{T_C}\right)^{\beta} \tag{74}$$

and

$$n_e(T) = A - BT + \frac{2(\Delta n)_0}{3} \left(1 - \frac{T}{T_C}\right)^{\beta}. \tag{75}$$

Near to the isotropic-nematic phase transition temperature, the contribution of the BT factor is negligible in comparison to the effect of the last term. The ordinary refractive index is therefore increasing with temperature, while the extraordinary refractive index is decreasing. Their change is much faster near the isotropic-nematic phase transition temperature. The extraordinary refractive index change is approximately twice as large as that of the ordinary refractive index.

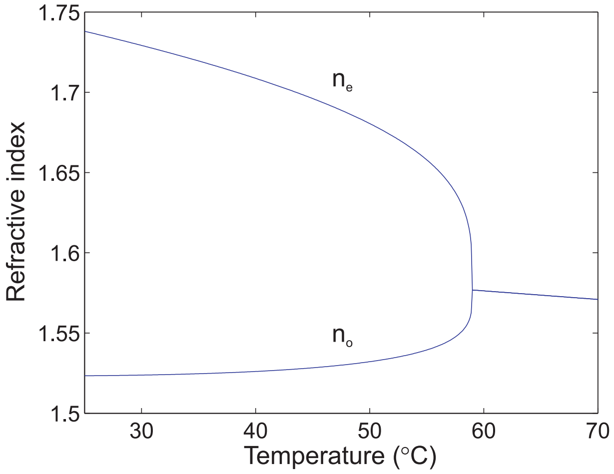

Figure 15: *Refractive indices of E12 as the temperature is increased.* With increasing temperature the ordinary refractive index is increasing whereas the extraordinary is decreasing. At isotropic phase there is only one refractive index. The refractive indices in the plot were calculated using (74) and (75).

2.5.2 Surface anchoring of liquid crystals

In all applications of LCs, the liquid crystal is in contact with another substance. The contact can be either with air, liquid or solid substrate. Because the interaction of LC on the interface, the LC can be oriented in the preferred direction[2]. We distinguish three main types of orientation: homeotropic, planar and tilted.

2.5.2.1 Anchoring on a anisotropic surface

If the surface is anisotropic, there is a preferred direction of LC molecules at the interface, refereed to as the *easy axis*. The interaction energy is minimal when the liquid crystal director is pointing in the direction of the easy axis. However, the direction of the director can be different in the bulk, which can also influence the director at the interface. So the director at the interface is not always parallel to the easy axis.

We define polar angle θ_0 and the azimuthal angle ϕ_0 for the easy axis. If $\theta_0 = 0$, the anchoring is *homeotropic*. If $\theta_0 = 90^\circ$ and ϕ_0 is well defined, the anchoring is referred to as *planar*. If $\theta_0 = 90^\circ$ and there is no preferred azimuthal angle, the anchoring is called *degenerate planar*. If $0^\circ < \theta_0 < 90^\circ$ and ϕ_0 is well defined, the anchoring is *tilted*, whereas if there is no preferred azimuthal angle the anchoring is *conical*.

The liquid crystal director $\mathbf{n}$ is pointing in the direction specified by the polar angle θ and the azimuthal angle ϕ. The mismatching of $\mathbf{n}$ and easy axis gives rise to the anchoring energy function of the liquid crystal: $f_s = f_s(\theta, \phi)$. When $\theta = \theta_0$ and $\phi = \phi_0$, f_s has a minimum value of 0. For small deviations the anchoring energy function can be expressed as

$$f_s = \frac{1}{2} W_p \sin^2(\theta - \theta_0) + \frac{1}{2} W_a \sin^2 \theta_0 \sin^2(\phi - \phi_0), \tag{76}$$

where W_p and W_a are the polar and azimuthal anchoring strengths.

The direction of the easy axis and the strengths of the anchoring depend on the chemistry and the topology of the surface in contact with the LC. Planar anchoring can be achieved by mechanically rubbing the substrate such as glass using a cloth. The rubbing creates micro grooves along the rubbing direction (Figure 16a). When the liquid crystal is aligned parallel to the grooves, there is no deformation. If the liquid crystal molecules were perpendicular to the groves, there would be deformation, which costs elastic energy. Therefore the liquid

---

[2] Instead of using a substrate the LC can be also oriented using external field or flow of LC.

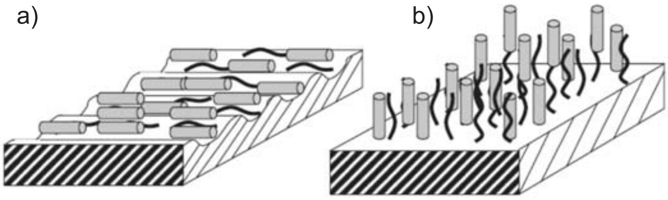

Figure 16: *Two types of anchoring of a NLC.* a) Planar anchoring and b) homeotropic anchoring. Reprinted with permission from [88]

crystal is homogeneously aligned along the grooves. The drawback with alignment created in this way is that the anchoring strength (10^{-5} J/m^2) is weak. A better choice for the planar alignment layer is rubbed polyimide. The rubbing not only creates the micro grooves but also aligns the polymer chains. The interaction between the liquid crystal and the aligned polymer chains also favors parallel alignment and thus increases the anchoring energy. The anchoring strength can become as high as 10^{-3} J/m^2. Furthermore, tilted anchoring with a few degrees pretilt angle can be made.

Homeotropic anchoring can be achieved using a monolayer of surfactants such as lecithin or silane. The polar head of the surfactant is chemically attached to the glass substrate and the hydrocarbon tail points out and perpendicular to the surface (Figure 16b). The intermolecular interaction between the surfactant and the liquid crystal promotes the homeotropic alignment.

2.5.2.2 Anchoring on an isotropic surface

Consider a LC in contact with an isotropic interface such as isotropic solid (e.g. glass), isotropic liquid (e.g. water) or as a free surface. It can also be in contact with gas or isotropic phase of the LC itself. The later is especially easy to describe, since there is no interaction with the substrate involved. The only thing that changes at this kind of interface is the density and the order parameter of the LC.

On an isotropic surface there are three possible types of anchoring: degenerate planar, homeotropic and conical. Planar and tilted anchoring are not possible for obvious symmetrical reasons. The degenerate planar anchoring is geometrically most reasonable with elongated molecules lying parallel to the surface. An example is a free surface of nCB in contact with clean flat glass or water. However, in some cases the anchoring can also be homeotropic, as with nCB in contact with the solution of surfactant such as SDS. Taking into account also the electrostatic interactions between the LC molecules and the substrate, we can get conic anchoring. This is the case of the free surface of MBBA or its nematic-isotropic interface. The angle of the conic anchoring at isotropic surface is very sensitive to temperature and surface contaminants.

2.5.3 Cholesteric liquid crystals

If the LC mixture is chiral, the molecules are not any more oriented in the same direction, but tend to rotate, making a helical twist, but locally the structure is still nematic. This kind of liquid crystals are called *cholesteric liquid crystals* (CLC). The components of the director are

$$\begin{aligned} n_x &= \cos(q_0 z + \phi) \\ n_y &= \sin(q_0 z + \phi) \\ n_z &= 0, \end{aligned} \tag{77}$$

where the *pitch* is

$$p = \frac{2\pi}{|q_0|}. \tag{78}$$

Both the direction and the phase of the helical twist z and ϕ are arbitrary and are usually defined by the surface. The sign of q_0 distinguishes between left- and right-handedness.

The liquid crystal molecules can be chiral by themselves, but usually a mixture of nematic LC and a chiral dopant is used. By changing the concentration of the dopant the pitch can be adjusted to the needs. The pitch is inversely proportional to the dopant concentration as

$$p = \frac{1}{\beta c_w} \tag{79}$$

where β is *helical twisting power* (HTP) and c_w is weight concentration of the chiral dopant. HTP it is highly temperature dependent, so it is also the pitch. It can increase or decrease with temperature or even change sign.

2.5.3.1 Position and width of the photonic bandgap

Chiral nematic liquid crystals provide periodic modulation of the refractive index that influences the light passing through the material. Due to the molecular chirality, the director spontaneously twists in a direction perpendicular to the long molecular axes. The periodicity of this helical birefringent structure depends on the molecular chirality and is in the range from $\sim$ 100 nm to several micrometers. According to the pitch length compared to the wavelength of the light we distinguish two interesting regimes of light propagation along the helical axis [88]. When the pitch is much longer than the wavelength of light ($P \gg \lambda$), the polarization twists in phase with the liquid crystal director and follows the helix. This is called the *waveguide regime.*

In the case when $P\overline{n} \sim \lambda$, CLC reflects circularly polarized light with the same handedness as the CLC. This means that a one-dimensional photonic bandgap exists along the helical axis. The edges of the reflection band are given by $\lambda_1 = n_e p$ and $\lambda_2 = n_o p$, so the center of the bandgap is

$$\lambda_c = \frac{n_e + n_o}{2} p = \overline{n} p \tag{80}$$

and its width is

$$\Delta\lambda = \Delta n p. \tag{81}$$

At angles different from normal incidence, the center of the reflection band shifts towards shorter wavelengths in accordance to Bragg's law. Under white-light illumination, cholesteric liquid crystals are often characterized by the fascinating iridescent colors of the reflected light. The reflectance of a cholesteric layer for the light in the center of the reflection band can be approximately given by [88]

$$R \approx \left(\frac{1 - e^{-2\Delta n \pi h / \overline{n} p}}{1 + e^{-2\Delta n \pi h / \overline{n} p}} \right)^2 , \tag{82}$$

where h is the thickness of the layer.

3 Materials and methods

3.1 Liquid crystals

To make the microcavities, different nematic liquid crystals were used as the material for the droplets. The most common and widely studied NLC is the 5CB (4-cyano-4'-pentylbiphenyl, Nematel). It has ∼ 10°C wide nematic temperature range around room temperature and medium birefringence. In this work, 5CB was used in some experiments, especially for LC biosensors. For experiments with electric field tuning, E12, a mixture of cyano-biphenyls (Merck), was used. Higher birefringence enables wider tunability and higher refractive index gives larger index contrast to the outside medium, the microcavities therefore having higher Q-factors. Larger birefringence and wider nematic temperature range also enables larger temperature tunability. For some time now, E12 is no more commercially available, so other wide temperature range commercial LC mixtures have been used also in this work. High birefringence mixture MLC-2132 (Merck) and low birefringence mixture MLC-7023 (Merck) were used. All the LCs used in this work have positive dielectric anisotropy.

To prepare chiral nematic (cholesteric) mixtures, S-811 chiral dopant (Merck) was used in concentrations from few percents up to 30 wt%. The dopant was added to the nematic LC, the mixture was heated to isotropic phase and mixed for few minutes. If the mixing was performed at room temperature in the nematic phase, the concentration of the dopant was very nonuniform and so was also the pitch and the wavelength of the reflection band.

Table 1: *Properties of LCs.* Refractive indices (measured at room temperature and at ∼ 600 nm) and transitions temperatures for liquid crystals used in this work.

Liquid crystal	n_o	n_e	Δn	C → N	N → I
5CB	1.54	1.71	0.17	24°C	35°C
E12	1.52	1.74	0.22	−10°C	59°C
MLC-2132	1.51	1.77	0.26	ND	114°C
MLC-7023	1.46	1.53	0.07	ND	80°C

3.2 Dyes

As a source of light inside the LC microcavities, different fluorescent dyes were used. Since we used green excitation lasers (514 nm and 532 nm), all the used dyes have strong absorbtion in green part of the spectrum and emission in the red.

One of the most important property of the dyes is their solubility in LCs. Typical concentrations ranged from 0.01 wt% to 0.1 wt%. But especially for lasing, very large concentrations, sometimes several percents, are needed, so nearly saturated solutions up to 0.3 wt% were used. Other important properties are quantum efficiency and photostability against photobleaching. Photobleaching is a process where the dye molecules are irreversibly converted to a non-fluorescent form. Depending on the shape of dye molecules they can orient in the same direction as the LC director or they can be randomly oriented. If they are oriented, also their dipole moment has a well defined direction and therefore the absorbtion as well as the emission is strongly polarization dependent. This effect is used to image local director field using a technique called *fluorescence confocal polarization microscopy* (FCPM). In the case of microcavities the orientation of the dye molecules could increase the coupling of the dye to a specific optical mode if the polarization matches the dipole moment. However, in this work we did not notice a major impact on the results.

The dyes used were

- Rhodamine B tetradecyl ester chloride (SPP-106), Figure 17a
- Rhodamine B octadecyl ester perchlorate (Sigma-Aldrich)
- BASF Lumogen F Red 305
- 4-dicyanomethylene-2-methyl-6-(p-dimethylaminostyryl)-4H-pyran (DCM, Exciton)
- 7-diethylamino-3,4-benzophenoxazine-2-one (Nile red, Sigma-Aldrich), Figure 17b.

At first we tried to use used Rhodamine B, since it has high quantum yield, but we found that it has low solubility in LCs. SPP-106 is Rhodamine B but with an added non-polar tail. It has advantages over plain Rhodamine B, since the non-polar tail of the dye ensures better solubility in the liquid crystal and prevents the diffusion of the dye into the surrounding medium such as PDMS polymer. The SPP-106 was synthesized by Dr. Stane Pajk from Prof. Slavko Pečar research group, Faculty of Pharmacy, University of Ljubljana. Rhodamine B octadecyl ester perchlorate is a similar compound and it is commercially available. Another commercially available dye is BASF Lumogen, that is used to dye plastic products. It has very high stability against photobleaching, but it can have low solubility in certain LCs. For lasing experiments in cholesteric liquid crystals, DCM dye is from literature by far the most used one. With good stability and solubility is well suited for most lasing experiments. We have found that Nile Red has among this dyes the best solubility in most liquid crystals. Higher concentrations in this case can give lower thresholds for lasing. Nile Red is also used for FCPM since it has good dipole orientation in LCs.

To prepare the dye solution in a LC, a small amount of dye was weighted and added to the LC. The LC was heated to isotropic phase and well mixed. After cooling back to room temperature, the solution was centrifuged to remove non-dissolved dye crystals. If smaller concentration of dye was needed it was difficult to weight sub milligram quantities of dye. Therefore, a more concentrated solution was first prepared and than diluted.

In the first experiments also CdSe fluorescent quantum dots were used instead of a dye. They poses superior optical stability, but tend to agglomerate in LCs, which limits their concentration.

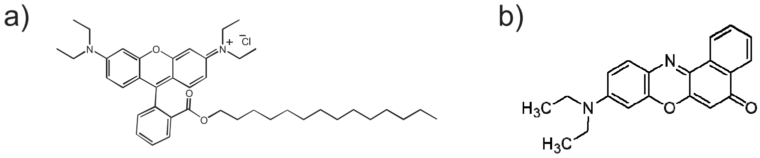

Figure 17: *Dye molecules.* Molecular structure of (a) SPP-6 and (b) Nile red. Adapted from Ref. [90].

3.3 Carrying medium

An important part of a LC dispersion is also the carrying medium. It enables formation of droplets, gives them mechanical support and the right anchoring. We can for example use just distilled water, that gives planar anchoring. However, if there are some impurities in the water, the anchoring can become tilted or even homeotropic. For stronger planar anchoring we can add 5% of polyvinyl alcohol (PVA), which also makes the dispersion more stable, preventing coalescence of droplets. For homeotropic anchoring in water, a surfactant can be added (see Section 4.7). Typical concentrations are in the order of 10 μg/ml. In our work > 4 mM sodium dodecyl sulfate (SDS) was used for homeotropic anchoring. Critical micelle concentration for SDS is 8.4 mM. Using SDS at concentration above the critical micelle concentration results in 5CB dissolving in the aqueous solution of micelles [91]. SDS makes the dispersion stable for months. As the outside medium with planar anchoring also glycerine can be used. It has higher viscosity, which facilitates the formation of droplets by mechanical mixing and also prevents to a certain level the movement of the droplets. Its higher refractive index can be beneficial in certain cases. Some LCs are slightly soluble in glycerol, but this was not a big problem in our experiments. All of this materials work perfectly for making droplets, however they are not appropriate for applying electric field to the droplets. In this case water is not at all suitable, since electrolysis occurs. The droplets are also deformed by the electric field and can also be pushed to one electrode, so a solid matrix should be used. By trying different polymers we found that majority of them are soluble in LC or have planar anchoring. We found, that PDMS (Sylgard 184, Dow Corning) is the most suitable for our purposes. It is a two component system: a base polymer and a curing agent. The base polymer is a viscous fluid, that can be used alone to make the LC dispersion, giving good results. For initiation of the polymerization 10% of the curing agent is mixed with the base. The polymerization rate is temperature dependent and the polymerization takes 48 hours at room temperature or as little as 15 min at 150 °C. In our case the polymerization was performed at room temperature, not to effect much the LC droplets. The PDMS containing the droplets can also be used as a free standing film, that can be mechanically deformed. An alternative to PDMS is CYTOP fluoropolymer. Because of its low refractive index (1.34), homeotropic anchoring, good chemical stability and low LC solubility it is a good candidate.

Table 2: *Carrying materials.* Refractive indices and anchoring of materials used as medium for LC droplets.

Material	**Refractive index**	**LC anchoring**
PDMS (Sylgard 184) unpolymerized	1.38	homeotropic
PDMS (Sylgard 184) polymerized	1.42	homeotropic
water	1.33	planar
5% PVA solution in water	1.34	planar
5 mM SDS solution in water	1.33	homeotropic
glycerol	1.47	planar

3.4 Making dispersion of LC droplets

After preparation of the dye doped LC mixture, the LC dispersion should be prepared. In the case of PDLCs the droplets are usually made by *phase separation* [45]. This means that initially the LC is dissolved in a polymer and the droplets are formed by polymerization-, thermally- or solvent-induced phase separation. In this case the droplets are very small, usually less than one micrometer, very dense and sometimes also of irregular shapes. In our case we need droplets larger than 10 μm, with as possible smooth surface, spherical shape and that are well separated from each other. Therefore, the procedures for making PDLCs are not appropriate for our case. The easiest way to achieve the desiderate properties of the dispersion is by mechanical mixing of the LC with a fluid that is immiscible with the LC (Table 2). The surface tension makes the droplets perfectly spherical and with smooth surface.

The mixing procedure differs for different carrying mediums. For fluids with high viscosity like glycerol and PDMS a small quantity, typically around 100 μl was put into a small bottle. Using a 10 μl pipette a small amount of LC mixture (typically 1 μl – 5 μl) was introduced in the center of the liquid. Stirring was performed using the same pipette by making circular movements. For PDMS, that is very viscous, just few turns were needed, but for glycerol a more vigorous mixing for $\sim 30\,\mathrm{s}$ was performed. For water based dispersions, $\sim 10\,\mu\mathrm{l}$ of LC was introduced into $\sim 1\,\mathrm{ml}$ water solution. Water has to low viscosity to produce small enough droplets just by stirring with pipette, so the whole bottle was vigorously shaken by hand for $\sim 10\,\mathrm{s}$. Alternatively, the water dispersion can be produced also by introducing the mixture of LC and water solution into ultrasonic bath. However, in this case also undesired very small droplets are formed, thus this method was avoided.

The mixing procedure is the same for different LCs, no matter if they are nematic, cholesteric or even smectic. Just for LCs with very high viscosity such as polymerizable mixtures and with LCs with LC phase above room temperature, the mixing is a little bit different. In this case the carrying fluid is heated before introducing the LC, the LC is then mixed and then the dispersion is cooled back to the room temperature. Especially for CLCs it is important not to prepare the mixture at to high temperature. The CLC should not go to isotropic phase, since at cooling back to cholesteric phase, a lot of defects are formed in the droplets. This is usually not a problem for NLCs, except for the ones with very high viscosity.

No other special mixing protocols were used, as the dispersions readily form, even when mixing manually. The only drawback of this method is that the droplets have very wide size distribution, from submicron to several hundreds of micrometers. In literature there are different methods for producing monodisperse droplets, that can be applied also for our dispersions. The LC droplets can be for example produced in a microfluidic channel [92]. Another method is to use monodispersed silica particles as templates [65]. Silica particles are covered with a thin permeable shell of polyelectrolytes, then the silica core is etched out and LC is introduced into the shell.

The dispersion was enclosed into thin glass cells. Two glass slides were sandwiched into a cell, where the cell-gap was controlled by polymer spacer of different thickness usually $20\,\mu\mathrm{m} - 150\,\mu\mathrm{m}$. To apply electric field to the droplets, glass slides covered with a thin indium-tin-oxide (ITO) layer, serving as an electrode, were used. The ITO electrodes were in the interior of the cell and the thickness was as small as possible to get the largest electric field strength. The LC dispersion was introduced to a glass cell using capillary force, and the cell was sealed with two component epoxy glue.

3.5 Optical setup

In order to observe, manipulate and excite the droplets an optical setup build around an inverted microscope was used. For the purpose of this work our old tweezers setup with argon laser was upgraded with several new devices. The configuration of whole setup is shown on Figure 18 and the photo in Figure 19 shows how it looks in reality. The IR tweezers are used to manipulate particles. The Ar+ tweezers were originally meant also for manipulating the particles, but in this work they were mostly used for fluorescent excitation. The pulsed laser was used to excite the microlasers in order to go above the lasing threshold. A spectrometer was than used to analyze the fluorescent light emitted from the samples.

The central part of the setup is an inverted optical microscope (Nikon Eclipse TE2000-U) on an optical table floating on air. To attach optical devices, the microscope has two side ports, one front port and two dichroic mirror turrets enabling the insertion of the light from the back of the microscope. The sample is mounted on a motorized X-Y-Z stage (Prior OptiScan II) that can be precisely controlled by a joystick or from a computer program. The microscope is equipped with a low magnification objective (Nikon Plan Fluor 20×/0.5) and a high numerical-aperture long working distance water-immersion objective (Nikon NIR Apo 60×/1.0w). The later is especially meant for laser tweezers manipulation, but because of high numerical aperture is capable of collection a lot of light and therefore also useful for low intensity processes such as fluorescence. In the experiments with temperature control of the sample, the water-immersion objective is not appropriate since the water that is in contact with the sample conducts heat and in the case of elevated temperatures also evaporates too quickly. In this cases a high numerical-aperture long working-distance objective with coverglass thickness correction ring (Nikon Plan Fluor 60×/0.7) was used. On the back of the microscope two tweezers setups were attached, each using its own filter turret. The laser light from both tweezers is reflected from the dichroic mirrors to the objective, filling its back aperture. The laser tweezers (TOU-200si, Tweezer unit, Aresis) on the top turret operate in infrared at 1064 nm using a CW 5 W Nd:YAG fiber laser (Tweez 200si, Laser unit, Aresis). In this case the used dichroic mirror reflects light with wavelength longer than 700 nm and transmits light bellow it. The laser tweezers at the bottom turret (LTM-N2000-A, Aresis) uses a CW Ar+ ion laser (Coherent, Innova 90C-4) with wavelength of 514.5 nm and 1.7 W of maximum power. The dichroic mirror reflects light with wavelength shorter than 520 nm and transmits light above it. Each laser tweezers are controlled by a separate software (Tweez v2.1 and Tweez v2.13m, Aresis) that enables creation of multiple traps which position and strength can be controlled individually.

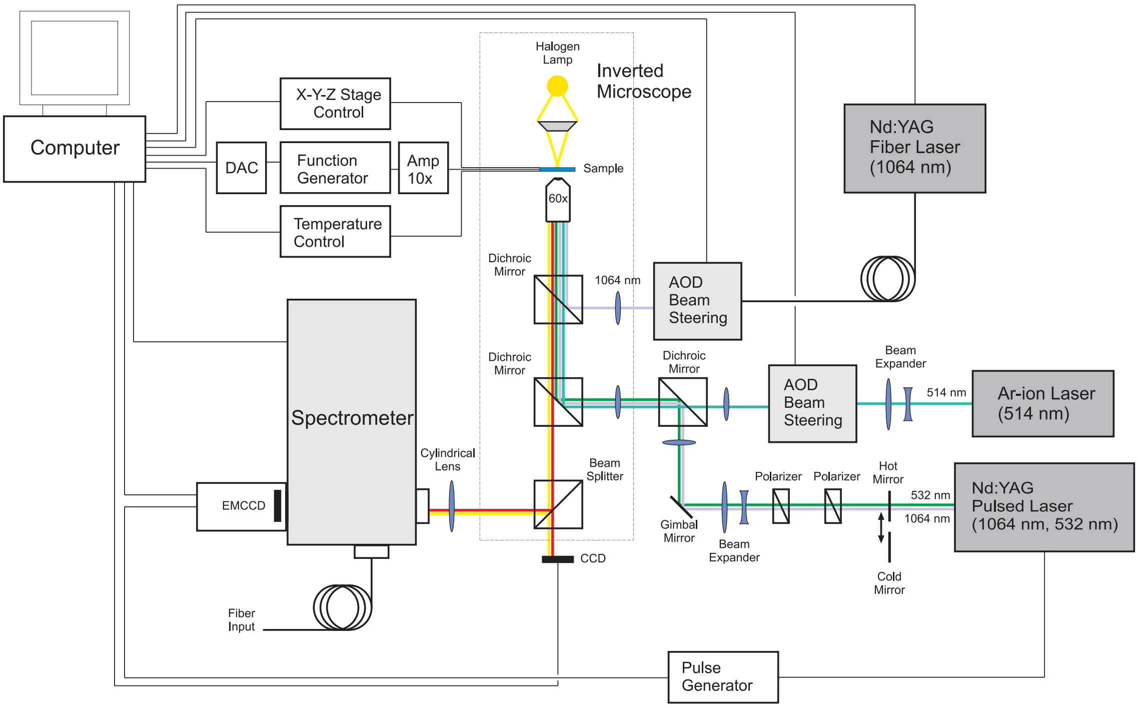

Figure 18: *Schematics of the optical setup.* The optical setup is build around an inverted microscope (center). There are three lasers (right) coupled in the microscope through different optical devices including two AODs working as optical tweezers. A spectrophotometer (bottom left) used for spectral analysis, is also coupled to the microscope. A computer (top left) controls the temperature, electric field and the position of the sample as well as other optical devices.

In between the bottom laser-tweezers setup and the filter turret there is an additional port with a dichroic mirror that is used for the insertion of a third laser. This port is used for an actively Q-switched doubled Nd:YAG laser with a pulse length of 1 ns, a maximum repetition rate of 10 kHz and a maximum pulse energy of 10 µJ (Pulselas-A-1064-500, Alphalas). The active Q-switching enables precise triggering of laser pulses by an outside pulse generator with frequencies ranging from single shot up to the maximum repetition rate. At the laser output, both second harmonic (532 nm) and the remaining fundamental wavelength (1064 nm) that is not doubled, are present[1]. By introducing cold or hot mirror, we

---

[1] Recently also an external third harmonic generator (THG, Alphalas) was bought that can be mounted in front of the pulsed laser and can produce UV light with 355 nm wavelength.

can send either just IR or just green laser light to the microscope. The laser is then passed through two Glan-Taylor polarizers. The first polarizer is aligned with the polarization of the laser and so just improves its polarization. The second one can be rotated such that the transmitted intensity can be adjusted. After the polarizers, there is a adjustable Galilean beam expander ($f_1 = -50\,\mathrm{mm}$ and $f_2 = 100\,\mathrm{mm}$). By changing the distance between the two lenses the beam can be made either collimated or a little bit convergent or divergent. In the case of a collimated beam it fills the back aperture of the 60× objective and it is focused by it to a diffraction limited spot. If the beam is divergent or convergent it is focused by the objective outside the focal plane. In this way we can illuminate larger spot on the sample, that can be as large as 100 µm by using 20× objective. To manually steer the laser beam, a gimbal mirror is located in the focal point of the telescope that transfers the angle change to the back aperture of the objective.

By using appropriate dichroic mirrors, almost any combination of the four laser beams (CW 514 nm, CW 1064 nm, pulsed 532 nm and pulsed 1064 nm) can be used simultaneously except the two IR lasers can not be used at the same time, as well as the two green lasers can not be used at the same time.

To collect light from the sample, it can be sent to either one of the side or front ports. On the right port there is a CMOS camera (PixeLINK, PLA741, 1280 × 960 pixels, physical pixel size 6.7 µm) enabling observation of the sample. The camera is especially suitable for fast imaging, such as tracking of particles, but it is not sensitive enough to observe low intensity fluorescence. To the left port we attached an imaging spectrometer (Andor, Shamrock SR-500i) with the input slit positioned in the focal plane of the microscope, which means that the sample is imaged onto the slit. The spectrometer is a Czerny-Turner type with 500 mm focal length. In the spectrometer there are three interchangeable diffraction gratings (300 lines/mm, 1200 lines/mm and 2400 lines/mm), all of them blazed at around 500 nm. The gratings can be rotated to any position so that the appropriate spectral range is imaged onto the CCD. By using the 2400 lines/mm grating a maximum optical spectral resolution of 0.05 nm can be achieved. Imaging spectrometer means that the plane at the input slit is imaged 1:1 to the output slit or CCD camera. If there will be a mirror instead of a grating, the spectrometer would just transfer the image. Actually this can be done by rotating the grating to its zero order where it acts as a mirror and if the input slit is wide open, the image from the microscope can actually be seen by the CCD. In normal operation the slit is narrow (minimum width is 10 µm) and the grating is rotated so that the first diffraction order is transmitted through the spectrometer. In this case each point on the slit is dispersed to different wavelengths by the grating. This enables the capturing of different spectra along the slit, that means a line stretching along the sample. The spectrometer also has an additional input for coupling in the light from a fiber and an additional output slit.

To the spectrometer there is attached a cooled back illuminated EM-CCD camera (Andor, Newton DU970N). It has an elongated detector with 16 × 16 µm pixel size and 1600 × 200 pixels, specially designed for spectroscopy. The 95% peak quantum efficiency, cooling to −85°C and electron multiplication (EM) enable the sensor to have single photon sensitivity. Therefore it is especially suitable for low light applications such as fluorescence. Using full vertical binning, spectra can be taken up to a maximum rate of 1600 per second, enabling the study of fast processes.

Before we bought the imaging spectrometer and the EMCCD camera, two compact spectrophotometers were used. The light was coupled out of the microscope from the front port into an optical fiber and to the spectrophotometer. Ocean Optics USB4000 spectrophotometer with spectral resolution of 1.5 nm and Ocean Optics Maya 2000 Pro with spectral resolution of 0.03 nm were used. Both have fixed grating and slit and are not particulary sensitive to light. A small number of high resolution linewidth measurements were also performed on a Raman spectrometer (LabRAM HR800, Horiba Jobin Yvone) equipped with multi-channel, air cooled CCD detector, coupled to an optical microscope (BXFM, Olympus). The resolution of the spectrometer is 0.019 nm per detector pixel.

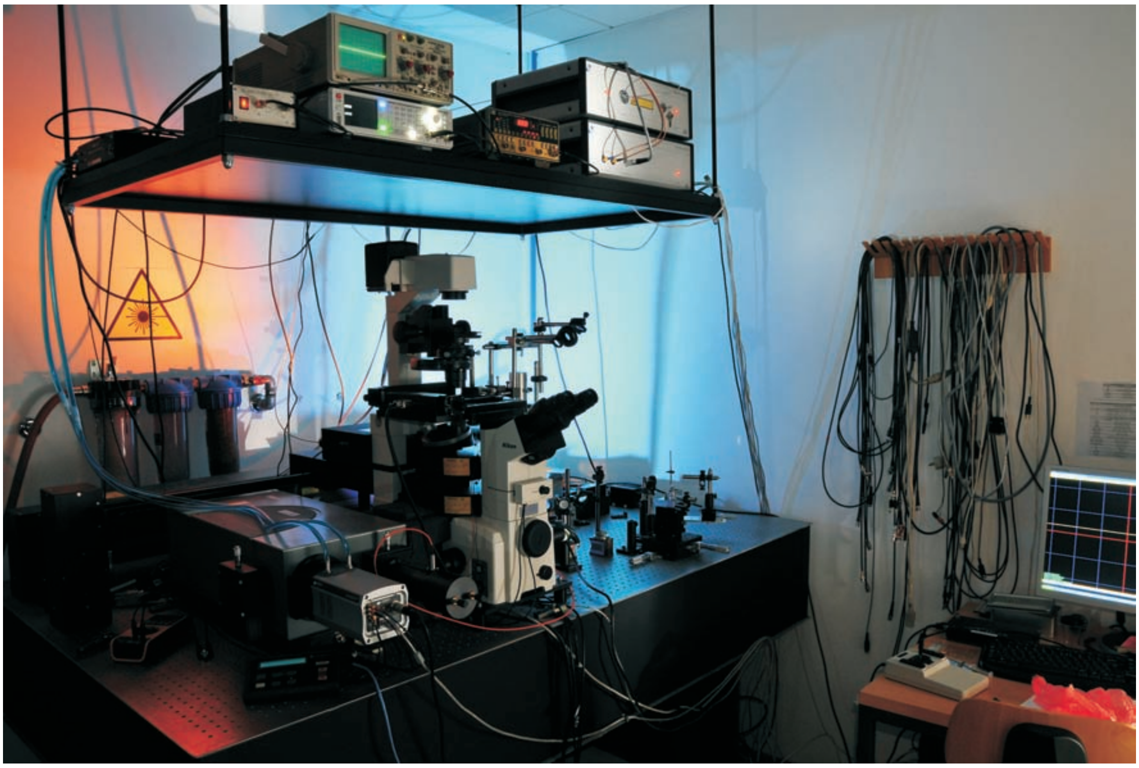

Figure 19: *Photo of the optical setup.* An artistic view of how the actual setup looks like in the laboratory.

Most of the devices integrated into the optical setup are connected to the computer and can be controlled by it. Several computer programs were written in Matlab to control the devices. This includes the temperature control by using ITC-503 temperature controller (Oxford Instruments), digital-to-analog converter (National Instruments, NI USB-6008) for applying electric field to the sample, CCD camera triggering, external AOD control and Prior Z stage control. Custom software was also developed for reading and analyzing spectra.

3.6 Microfluidic setup for chemical sensing

For sensing experiments, measurements of lasing on single trapped droplet were carried out while at the same time changing the concentration of the surfactant. The droplets were prepared from 5CB doped with 0.1 wt% Nile red. The dispersion was produced by shaking of 1 ml of 4 mM water solution of SDS and 10 µl of dye-doped 5CB. In this solution, the 5CB droplets obtain the radial configuration of the LC molecules and the SDS stabilizes the dispersion and prevents from sticking of the droplets to the walls of the microfluidic channels. A single LC droplet was observed and held in place by the IR laser tweezers through the 60× water-immersion objective. Most of the other droplets were flushed out by the flow. To reduce the necessary trapping power to minimum not to heat or deform the droplet, the measurements were performed in a blind leg of a T-shaped microfluidic channel where the flow is slower. The needed trapping power in this case was of 70 mW. We were not able to trap the droplets in 3D, so they were pushed to the upper channel surface. The channels were mad manually by cutting with a knife into an already polymerized PDMS layer (Sylgard 184, Dow Corning) that was attached to a glass slide to seal the channel. Three holes have been made in PDMS to which silicon tubes with inner diameter of 1 mm were attached. The channels had a relatively large cross section of approximately 1 mm × 1 mm enabling large flows of water (500 µl/min). We have kept the flow continuously running also when adding different concentrations of SDS.

Before starting the experiments, any traces of SDS used to stabilize the dispersion of droplets in order to introduce them into the microfluidic system, were flushed out by pure water. Than gradually increasing concentration of SDS was fed through the main channel without interrupting the flow. The flow was generated exclusively by gravity, by having the reservoir with water higher than the end of the tube connected to the exit of the microfluidic chip. The height difference was few centimeters. The trapped droplet was excited above the lasing threshold by the green Q-switched laser (532 nm) with repetition rate of 200 Hz. The laser light was focused by the objective to a waist diameter of ∼ 100 µm, illuminating the whole droplet uniformly. The spectrum was recorded by the Andor spectrometer in 2 s intervals.

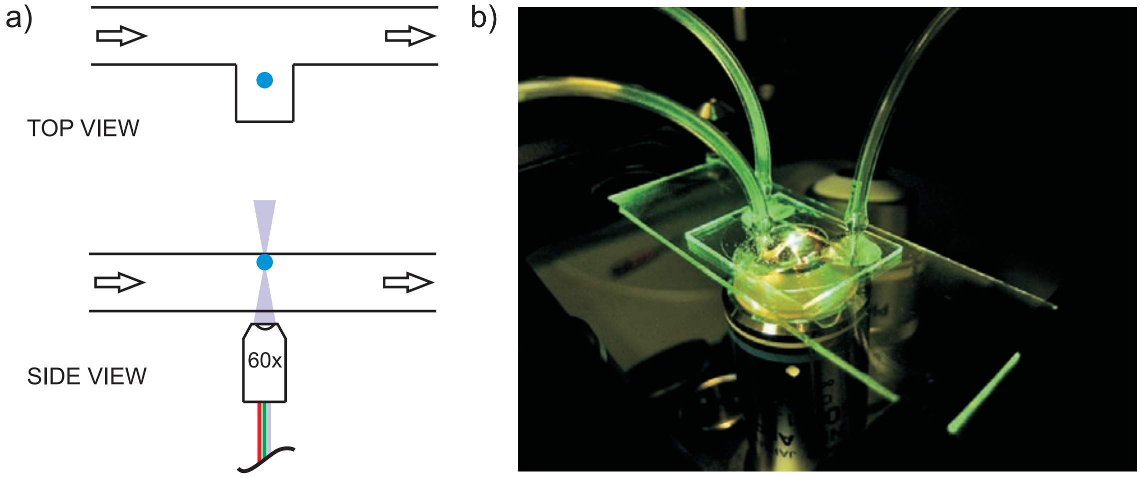

Figure 20: *Microfluidic setup for chemical sensing.* a) Schematic view of the T-shaped microfluidic channel. The IR laser tweezers were used to trap an individual LC droplet in the blind leg of the microfluidic chip. The droplet was pushed to the upper surface by the laser. b) The microfluidic chip mounted to the microscope and illuminated by the pulsed laser. The third leg of he microfluidic chip was actually also connected to a tube, to initially fill it with droplets. This tube was then sealed.

3.7 Setup for angular measurements of the 3D laser emission

To measure the angular dependance of lasing from cholesteric lasers a setup was needed that would enable the observation of the lasers from multiple angles. A CCD camera with a long working distance 10× objective was mounted so, that it could rotate 180° around the sample. A X-Y stage was used to center the objective focus into the center of rotation.

In the first angular measurements, the dispersion of CLC microdroplets in glycerol was introduced in between two glass slides. However, in this case the angle of observation is limited by the total internal reflection from the glycerine to the outside air. Also reflections on glass surfaces needed to be taken into account and the original intensity should be recalculated depending on the angle. Instead, in later experiments, the dispersion was introduced into a 1 mm diameter glass capillary, so that the droplets could be observed from all directions. The capillary was mounted on a X-Y-Z stage so that it could be positioned in the center of rotation and Z direction was used to travel up and down the capillary. A single droplet that was positioned as near as possible to the center of the capillary was observed. If the droplet is on one side of the capillary, the glycerol acts as a lens and distorts the image in a different way when viewing from different directions. The droplet was illuminated from one side by tightly focused laser. A fiber with a lens and connected to the spectrometer was used to check if the droplet is lasing. An additional white light illumination was used to see the droplets and to align the setup. The CCD camera was rotated around the sample and a video was taken. The intensity of lasing was extracted from this video taken at different positions around the droplet (Figure 73). Only pixels with the highest intensity corresponding to high intensity from the center of the droplet were taken into account.

To measure the spectral dependence of lasing, the optical fiber that has been used to check if the droplet was lasing, was placed instead of the camera and rotated around the sample. With the fiber we were not able to accurately measure the intensity, since with the fiber it is no possible to actually see the droplets and to align it perfectly. Also with the camera, if the image of the droplet moves across the image while rotating the camera, the intensity can still be extracted. In the case of the fiber the image of the droplet should be always exactly centered to the fiber. Even though the measured intensity with the fiber was not constant, the spectral position of the laser line could be easily extracted from the data.

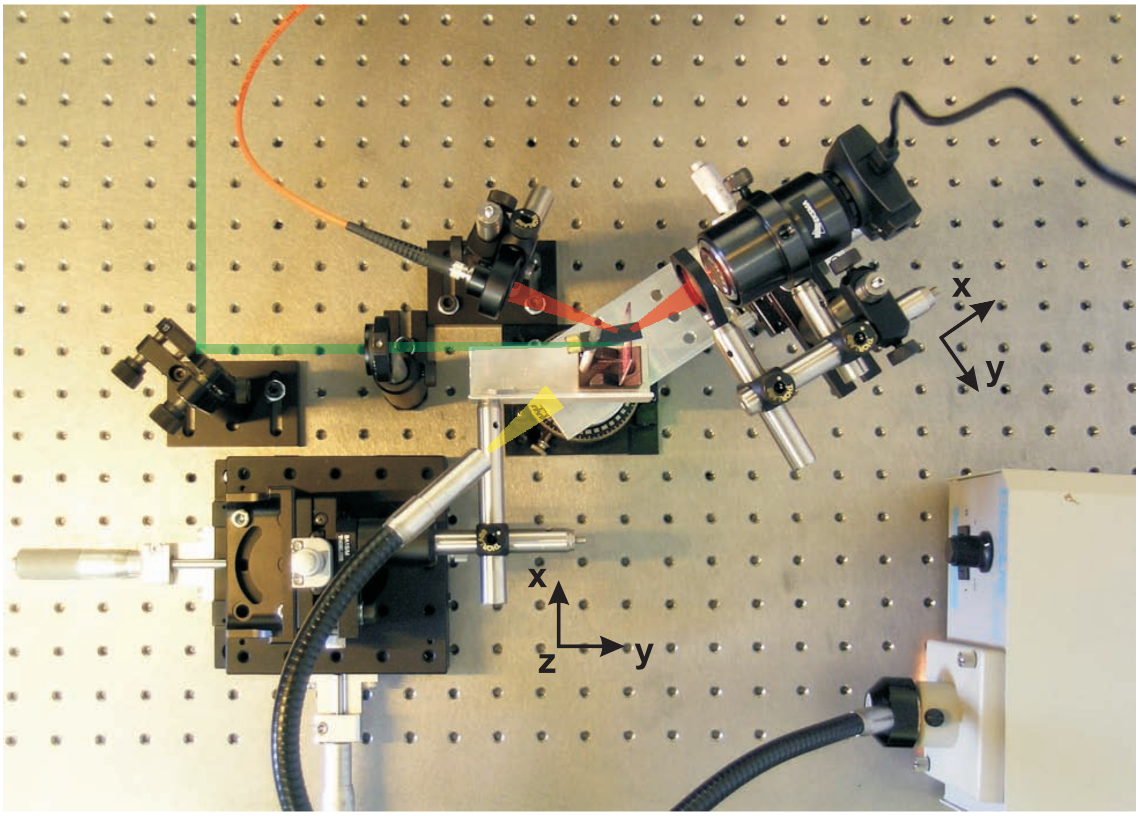

Figure 21: *Experimental setup for angle dependence measurements.* The sample, in this case the dispersion of CLC droplets in glycerol in between two glass slides, is located in the center of the image. From left, the sample is illuminated by a green pulse laser. The light from the sample is than captured by a fixed fiber (top left) and a rotating CCD camera (top right). A white light illumination source is also used (bottom left).

3.8 Setup for 3D laser polarization measurements

Polarization of the light emitted from the CLC microlasers was also investigated. The setup should be able to measure if the light is linearly, circularly or elliptically polarized. The sample was illuminated by circulary polarized light from the doubled Nd:YAG pulsed laser by inserting a quarter-wave plate. To measure linear polarization of the light emitted from a single 3D laser, a polarizer is inserted between the sample and the detector. If the light is linearly polarized there will be a modulation of light intensity on the detector, when the polarizer is rotated. To measure circular polarization a broadband quarter-wave plate was inserted in between the sample and the polarizer and the intensity is again measured as the polarizer is rotated. The quarter-wave plate in this case transforms circularly polarized light to linear polarization. Wave plate and polarizer could be inserted in between the microscope and the spectrometer in the standard optical setup (Figure 18), however, the light is in this case passing through dichroic beam splitters and other optical components in the microscope, which could change its polarization. Therefore, the light was collected by an independent optical setup above the sample (Figure 22) consisting of a 10× objective, optional quarter-wave plate, rotating polarizer, longpass filter and fiber coupler. The light was then sent through the fiber to the spectrometer.

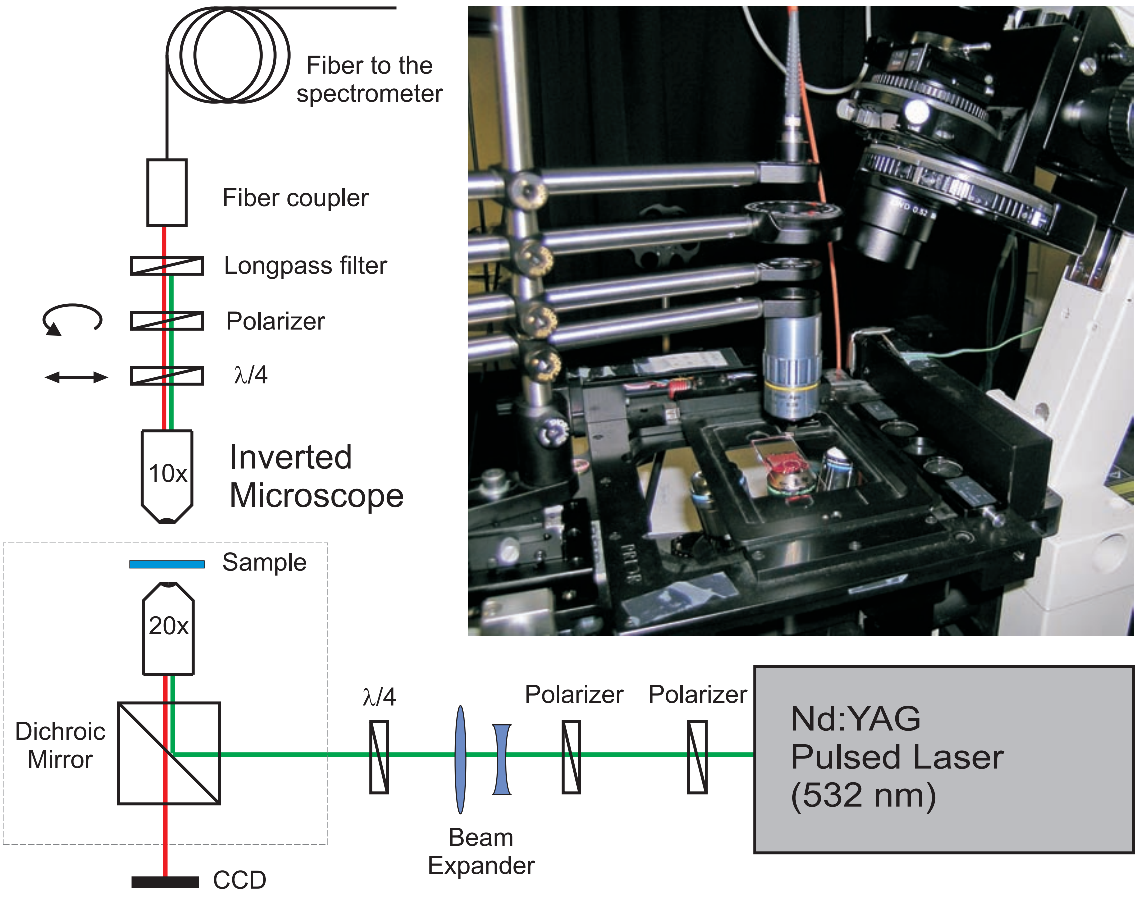

Figure 22: *Experimental setup for 3D laser polarization measurements.* The inset shows the actual setup in the laboratory.

3.9 Sample preparation and setup for strain tuning

For the strain measurements a soft matrix containing the LC droplets should be used. We decided to use a thin self standing film of PDMS and stretch it to achieve the mechanical deformation. The PDMS is known to be a good carrying for the LC droplets, since it has been used before by us in the electric field tuning experiments (Section 4.3). It is also soft enough that can withstand high applied strain. By changing the amount of added currying agent, its mechanical properties can also be changed. To make the film, the dispersion of LC droplets in PDMS was introduced in between two microscope slides that were separated by 150 µm spacers. The two glass slides were dipped into a solution of soap and dried before they were used in order to achieve easier detachment of the PDMS film. After 48 hours the polymerized PDMS was removed from the glass slides forming a free standing film. The film was mounted to a microscope, so that one end was fixed and the other was attached to a translation stage having a micrometer screw (Figure 23). In this way the film could be manually stretched with 10 µm precision. The Ar+ laser was used to illuminate a single droplet near its rim. The film was stretched in small steps and each time the spectrum was recorded. Every time when strain was increased, the droplet moved out of the center of the image and the laser was not illuminating it any more. So the droplet had to be repositioned to the original location by using the motorized X-Y microscope stage.

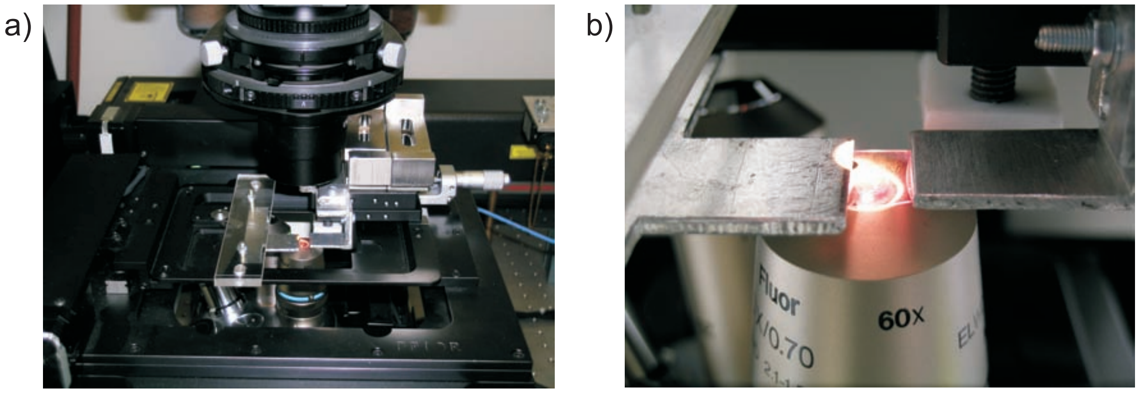

Figure 23: *Experimental setup for strain tuning measurements.* a) A 150 µm thick free standing PDMS film containing the LC droplets is glued to two metal holders. The right holder is attached to a micrometer screw that allows precise stretching of the film. b) A closer view of the film.

3.10 Sample preparation for electric field tuning

For electric field tuning experiments, a dispersion of E12 was prepared in PDMS, which was then polymerized. When applying electric field it is important, that the droplets are fixed and do not deform or move under the action of the field. Therefore, a solid matrix was used. As a material E12 was chosen because it had the highest birefringence among the available LCs in the lab, therefore enabling the highest tunability. The E12 LC was doped with SPP-106, the only LC soluble dye, that did not diffuse in to the surrounding PDMS and was available in the laboratory. Later, a number of different fluorescent dyes were found to be suitable for this purpose (Nile red, BASF Lumogen dyes, DCM, etc.). The LC droplets were prepared by method described in Section 3.4. The dispersion was then introduced in between two glass slides covered with a thin indium-tin-oxide (ITO) layer, serving as an electrode. The electrodes were in the interior and the cell thickness was controlled by 20 µm polymer spacers. A single droplet was observed using the inverted microscope by the 60× objective, illuminated by the argon laser and the spectra was analyzed by a spectrometer. While measuring the spectrum, a sinusoidal electric voltage with the frequency of 50 kHz was applied to the ITO electrodes. The corresponding electric field in the cell was up to $2.6\,\mathrm{V_{RMS}}/\mu\mathrm{m}$. The voltage amplitude was controlled using the digital-to-analog converter, that was used as a external modulation connected to a function generator. A 10× amplifier was used in between the function generator and the sample.

3.11 Preparation of cholesteric 3D lasers

For 3D Bragg lasers, a mixture of a nematic LC and a chiral dopant was needed with the pitch in the range of 400 nm producing photonic bandgap in red part of the spectrum. A fluorescent dye dissolved in the CLC mixture was used as an active material. Two different dye-doped cholesteric liquid-crystal mixtures were used. The low birefringence mixture was prepared using MLC-7023 liquid crystal with 25.5wt% S-811 chiral dopant and 0.2wt% Nile red fluorescent dye. The high birefringence mixture was prepared using MLC-2132 liquid crystal with 26wt% S-811 chiral dopant and 0.5wt% DCM fluorescent dye. In both cases the dye concentration was near saturation. The concentration of the chiral dopant was chosen so, that the longer wavelength edge of the cholesteric photonic bandgap overlapped with the emission maximum of the fluorescent dye. To test this, the position of the photonic bandgap was determined by measuring the spectrum of white light reflected from a 30-μm-thick planar cell containing the mixture.

The dispersion of droplets in glycerol was prepared by method described in Section 3.4. The dispersion was introduced in between two glass slides separated by approximately 150 μm. As single droplet was observed and illuminated by a pulsed laser through the 20× objective. The actively Q-switched doubled Nd:YAG laser with a pulse length of 1 ns, at the repetition rate of 200 Hz and a maximum pulse energy of 10 μJ was used as the excitation source. It was focused through the same objective to a waist diameter of ~ 100 μm.

4 Experimental results and discussion

4.1 Dispersion of liquid-crystal droplets

To make the LC microcavities the most important step is to be able to produce nice spherical LC droplets in a carrying material. We have tried different methods known from the preparation of PDLCs [45,46]. Most of these procedures are based on phase separation of initially homogenous mixture of a LC and a polymer. The droplets formed by phase separation are usually quite small ($\sim 1\,\mu\mathrm{m}$), of irregular shape and very dense. None of this is good for our purposes. Therefore we used a very simple procedure of mechanical mixing of a LC and non-miscible fluid. Figure 24 shows a dispersion of E12 droplets in PDMS under crosses polarizers. The droplets are polydispersed, with sizes ranging from $1\,\mu\mathrm{m}$ to $50\,\mu\mathrm{m}$. Because of surface tension they have almost perfect spherical shape and smooth surface (Figure 25a). PDMS gives homeotropic anchoring so that the molecules are perpendicular to the droplet surface. The director configuration is radial, that means, that the director is pointing in the radial direction in every point of the droplet volume (Figure 25c) inducing splay elastic distortion [38]. The exception is the center of the droplet where a point topological defect appears, called radial hedgehog defect [93]. It can be seen as a black spot in the center of the droplet (Figure 25a). The radial structure can be also observed under crossed polarizers where we can see the typical dark cross (Figure 25b). To further confirm the structure, *fluorescence confocal polarizing microscopy* (FCPM) [94] images of the droplets were taken. The droplets contained Nile red dye, which molecules orient in the direction of the director, so that the excitation and emission of light is the highest along the director. In Figure 25d we can clearly see the radial orientation of the molecules.

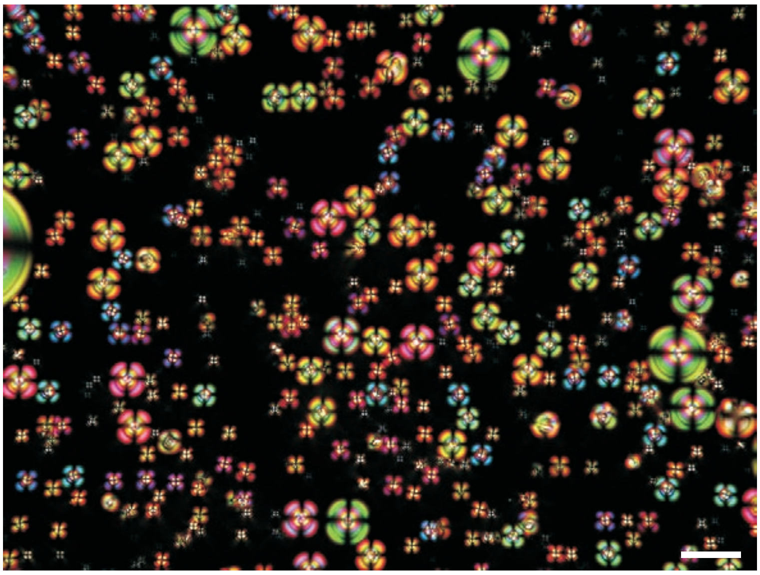

Figure 24: *Dispersion of E12 droplets in PDMS under crossed polarizers.* The colors of the droplets are caused by the interference of ordinary and extraordinary ray and is dependent on the birefringence and the size of the droplet. Scale bar $20\,\mu\mathrm{m}$.

Similar dispersion can also be readily formed in water solution of SDS. The appearance of the droplets is identical as when using PDMS. The difference is that after waiting 48 hours the PDMS polymerizes and fixes the position of the droplets. The appearance of the droplets as well as the WGMs did not change much after polymerization. However, after few days after polymerization, the WGMs were not visible any more in most of the droplets, but the appearance of the droplets did not change. This did not happen in non-polymerized PDMS (no curing agent added) and the WGMs were visible also in several months old samples.

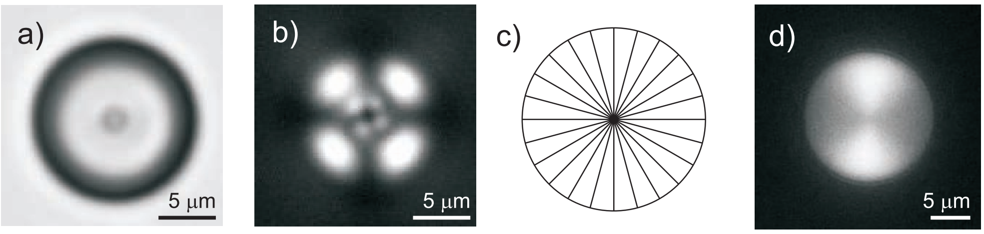

Figure 25: *Radial NLC droplet.* a) Micrograph of a 15 μm droplet of nematic liquid crystal E12 in PDMS. b) The same droplet under crossed polarizers. c) Structure of the director field inside the microdroplet, deduced from b). The lines (i.e. director field) present the direction of orientation of LC molecules. d) A FCPM slice through the center of the droplet. The excitation and emission polarization is vertical.

An important part in using LC WGM microcavities for applications is not just the ability to make nice droplets, but also to be able to place them in precisely determined positions to couple them with other optical components. In the case of LC droplets they are floating in a liquid medium and can be moved and assembled to complex structures by using laser tweezers (Figure 26). If a polymerizable carrying fluid is used, for example PDMS, the structure can be assembled and then the fluid is polymerized fixing the position of the droplets. In PDMS it is however quite difficult to move the droplets because of very high viscosity and assembly takes a lot of time. Also the surface separation between the droplets can not be adjusted precisely, but fortunately the repulsive force between the surfaces of the droplets prevents their coalescence.

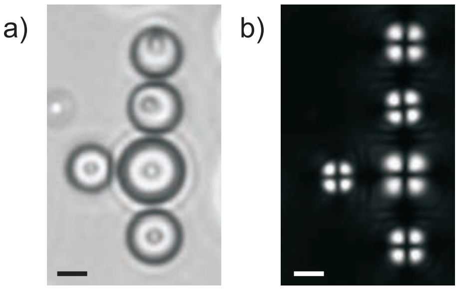

Figure 26: *Assembly of liquid-crystal droplets in PDMS.* Before the PDMS was polymerized, the droplets were assembled into a T-shape structure by using laser tweezers. Scale bar 5 μm.

By mechanical mixing we have very limited control over droplets size. The average size can be partially controlled by the time and speed of mixing, however, the size distribution is quite wide. The polydispersity of the droplets is not that important for laboratory experiments, since we can select one droplet of a desired size and do experiments on it. In this case, it is important that the droplets are well separated from each other, so we can study individual ones. However, with low droplet density in PDMS we had some problems. The cyanobiphenyls, from which the E12 is composed, are slightly soluble in PDMS. At high concentrations of droplets, the PDMS gets saturated quite quickly and the droplets are not much affected by this. However, at concentrations of LC lower than approximately 1%, some components of E12, probably the lighter ones, are transferred to the PDMS. What is left does not have spherical shape any more and it is also not fluid any more, especially if heavier cyanobiphenyls are left. Interestingly, most of the droplets are transformed into birefringent tubes (Figure 27). The walls of the tubes are made from the remainings of the E12 and probably still have at least partially ordered director structure, since they show birefringence under crossed polarizers (Figure 27c and d). This process happens quite quickly after mixing of LC into PDMS and is not affected by latter PDMS polymerization.

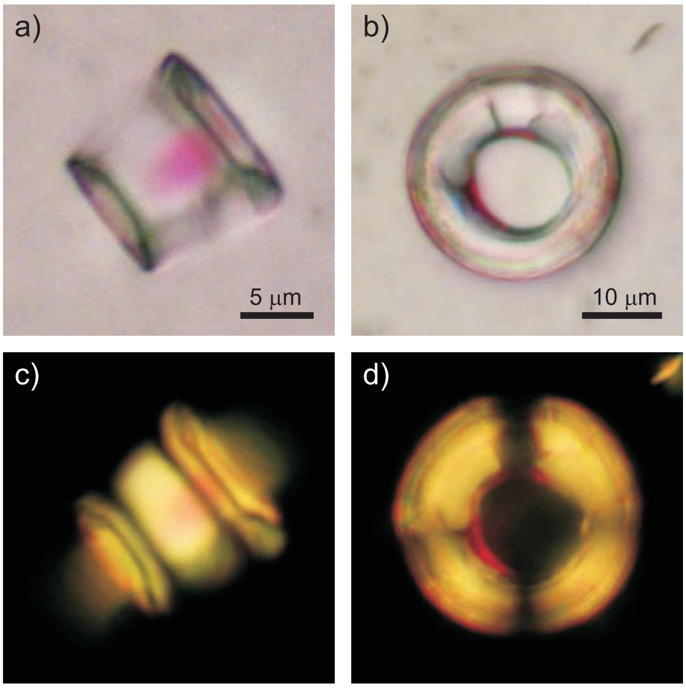

Figure 27: *Two examples of tubes formed from E12 LC when mixed with PDMS.* a) A tube from side view and b) a tube viewed through its hole. c) and d) The same two tubes under crossed polarizers. Birefringence is clearly seen.

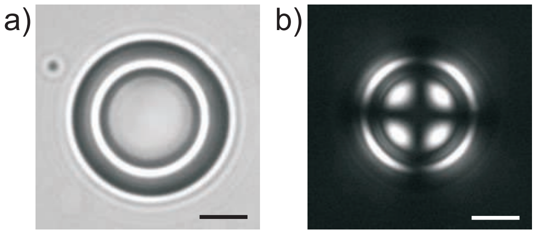

Figure 28: *A LC shell.* A 10 μm melamine formaldehyde particle is positioned in the center of a LC droplet. The outside medium is PDMS. a) The droplet in white light illumination and b) the same droplet in crossed polarizers. Scale bar is 5 μm.

Instead of using just LC to make the droplets, also hard particles can be introduced. In Figure 28 a 10 μm melamine formaldehyde particle having homeotropic anchoring is sitting in the middle of a droplet. The boundary conditions promote the central position of the particle making a shell of LC of almost arbitrary thickness around the particle. The particle-droplet combination is made in a fairly simple way. At first a dense dispersion of particles is made in a LC. The dispersion is then mixed with PDMS. In the mixing process, when the droplets ar formed, some of them contain one or more particles. In the droplets containing just one particle, the shell thickness varies, depending how big droplet of LC is formed. Some particle are also expelled out of the LC into the PDMS. Thin shells could be interesting because they could provide faster switching speed with the electric field, since of small LC volume and small thickness. By measuring the spectra of WGMs in shells as thin as 1.5 µm we did not observe any difference in the modes of a droplet of the same size, but not containing the particle.

4.2 Whispering-gallery modes in nematic liquid-crystal droplets

Once we were able to produce nice spherical droplets, we could introduce a fluorescent substance into the LC and than excite and observe the modes inside the droplets. A single droplet was illuminated by a tightly focused 514 nm laser beam near its edge (Figure 29). A bright spot of fluorescent light was observed at the point of the laser beam as well as on the opposite side of the droplet (Figure 30). A bright stripe is also observed in between the two bright spots and there is a hint of a light ring around the droplet. What is observed can be explained by WGMs circulating inside the droplet near its surface. The fluorescent molecules are excited at the point of the laser spot and emit light in all the directions. Some of the light gets trapped as WGMs. Just the light that circulate in planes that intersect the laser spot are present in the droplet. What light is actually observed is dependent on the direction of observation. We can mostly see the light that circulates in the plane along the viewing direction as the bright spot on both sides of the droplet and a stripe in between.

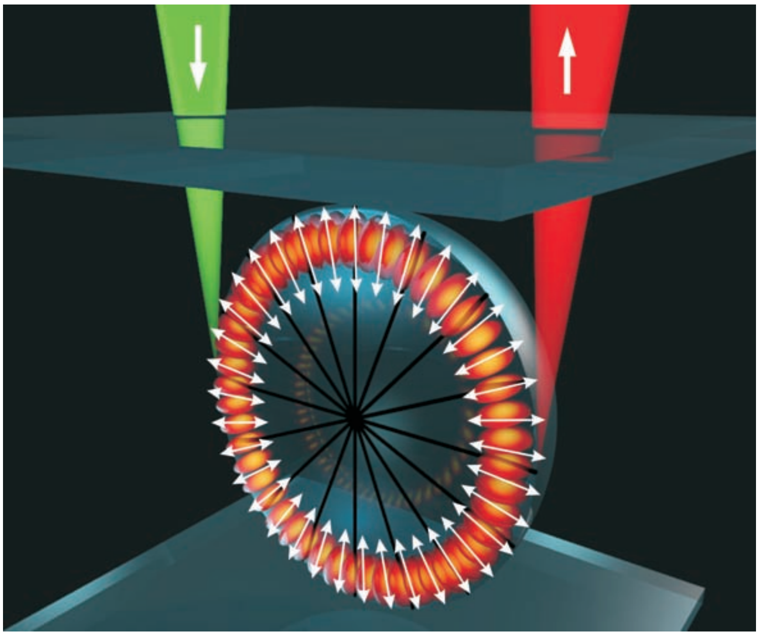

Figure 29: *Schematic view of WGMs in a LC droplet.* WGMs are excited by a focused Ar^+ laser (green light illuminating the edge of the droplet). Only the light irradiating towards the microscope objective is detected (red cone). A TM WGM is shown, with its electric field oscillating in a radial direction.

We observe fluorescence only inside the NLC droplets, which indicates that the dye has not diffused into the surrounding PDMS. In the first experiments we have used CdSe fluorescent quantum dots (QDs) dispersed in 5CB. The QDs experience very little photobleaching and have quite bright fluorescence. However, because of elastic deformation of LC around them, they tend to agglomerate in order to reduce the distortion. The clusters formed in this way scatter light and therefore drastically lower the Q-factor. Despite this, the first WGM observed in a LC droplet were indeed excited in dispersion of QDs in 5CB. However, this was only possible with very low concentrations of QDs and just in droplets that did not contain larger agglomerates.

The fluorescent light from a single droplet was sent to the spectrometer and analyzed. In Figure 31 there is one example of such spectrum for a 16 µm droplet. We can see the fluorescent background, which is nearly the same as for bulk dye doped LC, with the

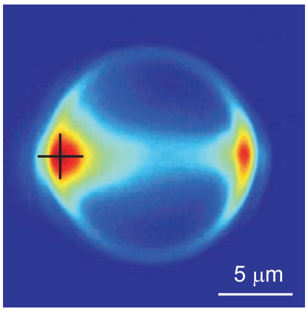

Figure 30: *False color image of fluorescent light intensity from a LC droplet.* The droplet is illuminated by Ar^+ laser near the left edge (black cross).

maximum located in red at 580 nm. On this background there are a number of very sharp spectral peaks. They correspond to WGMs circulating near the surface of the droplet. The modes are grouped in distinct groups, where they are almost equally spaced.

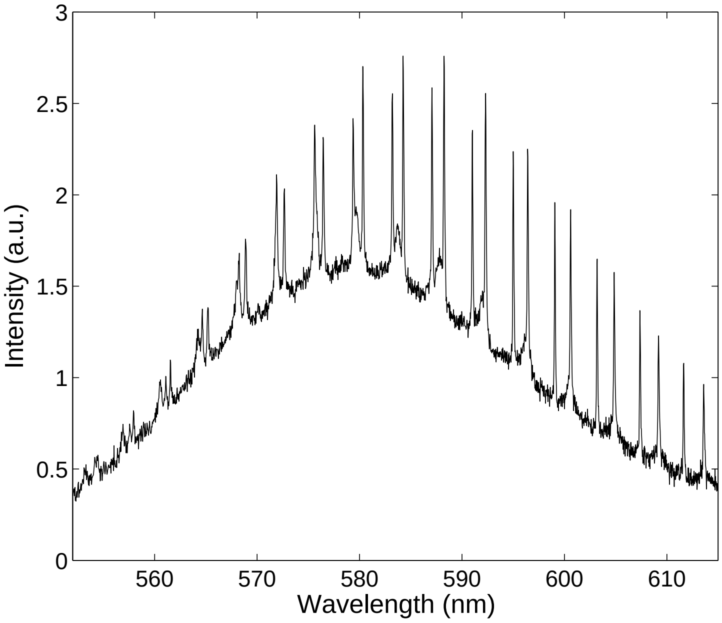

Figure 31: *Spectrum od fluorescent light captured from a LC droplet.* Very sharp peaks corresponding to WGMs are observed on the broad fluorescent background. Droplet size is 16 μm.

Instead of peaks at the positions of the optical modes, one would rather expect dips in the spectrum. The fluorescent molecules emit light in a broad spectrum and in all the directions. The light that matches the frequency as well as the direction of a WGM is trapped by the droplet and because of longer optical path it is absorbed and scattered by the material. All the other light that does not match any mode is directly emitted from the droplet. Therefore at the WGM frequencies we should observe dips in the spectrum. However, Purcell effect (Section 2.1.2), which makes the dye to emit more light at the resonant frequencies, has to be taken into account.

If the light, that is sent sent to the spectrometer, is captured just from the part of the droplet opposite to the excitation point, the spectral peaks of the WGMs are higher in respect to the fluorescent background. This is because mostly the light that is captured as WGMs is transferred to the other side and leaks out. If we are capturing the light from the laser excitation point, also the light that is spontaneously emitted in all the directions from the dye molecules is contributing to the fluorescent background.

The droplets can also be excited by using an optical fiber (Figure 32). The laser light is coupled into the fiber and the fiber end is introduced into the dispersion of the droplets (Figure 32a). The light from the excited droplets can be collected by a microscope objective, or by the same fiber. The fluorescent light from the droplet entering the fiber is separated from the excitation light by a dichroic mirror and sent to a spectrometer (Figure 32b).

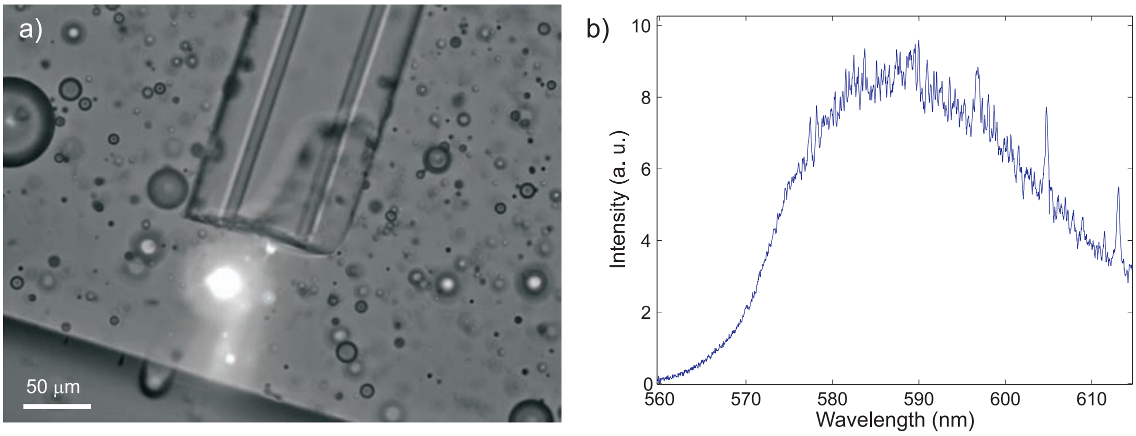

Figure 32: *Fiber excitation of WGMs in LC droplets.* a) A multimode fiber with the core diameter of 60 µm is introduced in the dispersion of LC droplets in PDMS. The fiber is positioned so, that it illuminates just one droplet. b) In the spectrum of fluorescent light that gets coupled back into the fiber we can observe the WGM peaks.

4.2.1 Polarization properties

In order to understand which modes are present in the spectrum, we first have to look at the polarization properties. There are two possible WGMs polarizations, the TE polarization where the electric field oscillates parallel to the surface of the sphere (Figure 33a) and TM polarization where the electric filed is perpendicular to the surface (Figure 33b). For isotropic sphere both modes have the same refractive index. However, LCs are birefringent and different polarizations sense different refractive indices. In the LC droplets the optical axis points in the radial direction. Therefore, the TE modes sense the lower index, the ordinary one ($n_o = 1.52$), and the TM modes sense the larger one, the extraordinary index ($n_e = 1.74$). The TM modes have larger index contrast to the outside medium ($n_s = 1.43$), so we expect them to have higher Q-factors than TE modes. In smaller droplets we expect only TM modes to be visible, since the higher contrast. Two different indices for the two polarizations are quite an unique feature of the LC microresonators. In isotropic microresonators the two polarizations are always in pairs, but in our case the two polarizations are completely independent and can be tuned individually by selecting the appropriate material with a certain birefringence.

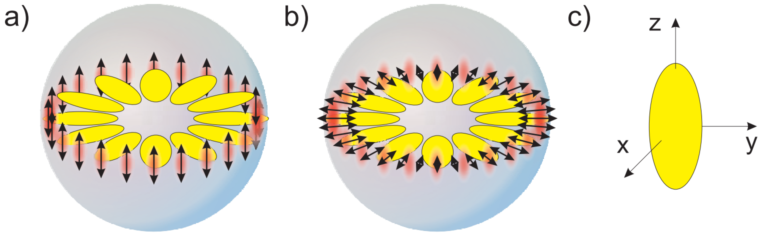

Figure 33: *WGM polarization schematics in LC droplets.* Schematic drawing of the electric field direction for a) TE modes and b) TM modes. c) The yellow prolate ellipsoid represents the uniaxial dielectric tensor of the LC.

Polarization properties of light emitted from a smaller droplet, where just one set of TM modes was visible, were analyzed. The polarization of the excitation laser was rotated to either parallel or perpendicular to the surface of the droplet at the point of illumination by using a $\lambda/2$ waveplate. The polarizer through which the light was sent to the spectrometer or camera was also rotated. The results are presented in Figure 34 and Figure 35 for the four cases. It can be observed that the highest intensity we get when both the excitation on detection polarizations coincide with the polarization of TM modes (Figure 34a).

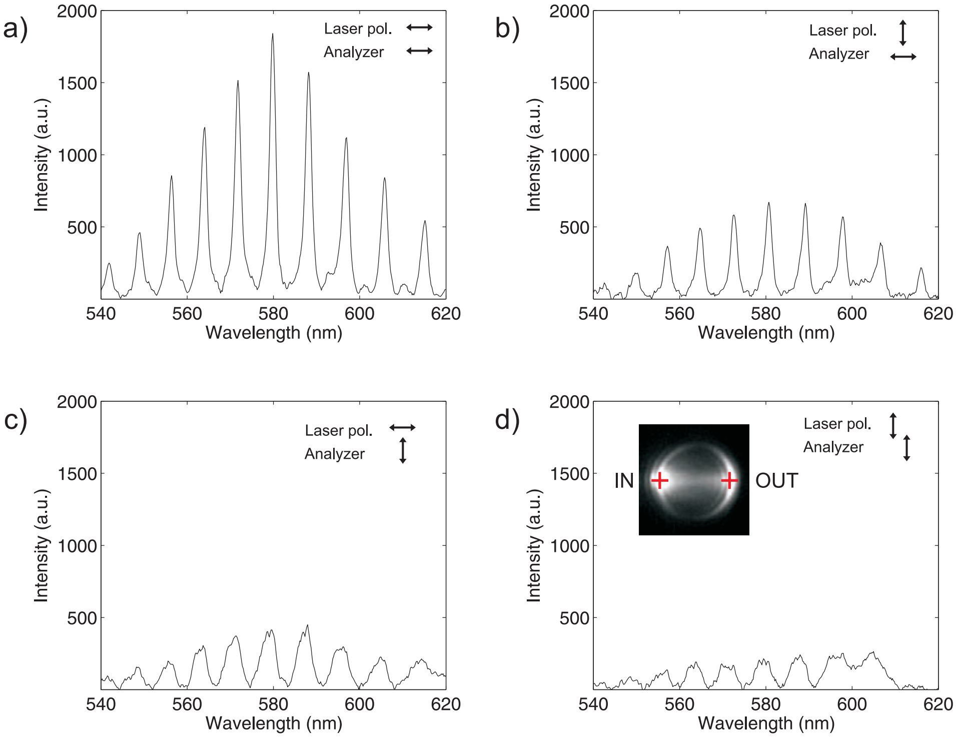

Figure 34: *WGM spectra at different polarizations.* Spectra of light emitted from a 11.7 μm E12 droplet when the excitation and emission polarization is changed. The polarization direction is given by the arrows. The horizontal polarization direction corresponds to TM modes. The inset in d) shows the orientation of the droplet and points of excitation and light detection.

Additionally also images of WGMs circulating in droplets were taken at different laser polarization and analyzer rotation (Figure 35). The intensity on the images matches the spectral results (Figure 34).

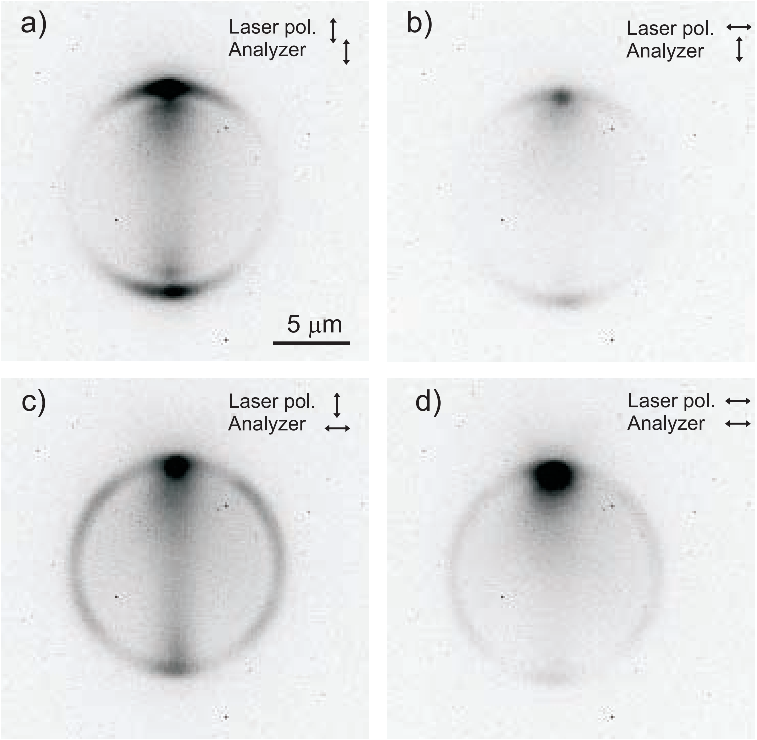

Figure 35: *Fluorescence images at different polarizations.* Images of fluorescent light emitted from a 11.7 µm E12 droplet when the excitation and emission polarization is changed. The polarization direction is given by the arrows. The horizontal polarization direction corresponds to TM modes. For clarity the images are inverted, so the darker color represents higher intensity. The illumination spot is at the top of the droplets. a) The laser polarization and analyzer direction are the same and match the TM modes. A bright spot is observed on the other side of the droplet indicating the TM modes circulating in the plane parallel to the direction of observation. b) When the laser polarization is rotated the intensity is greatly reduced, since it does not match the TM modes any more. c) If the laser polarization matches the TM modes, but the analyzer is perpendicular to this direction a ring around the droplet is observed. These are the TM modes circulating in the plane perpendicular to the observation direction. d) An finally if both polarizations do not match the TM modes, just a bright spot corresponding to fluorescence is observed at the point of laser excitation.

4.2.2 Fitting the WGMs

To further analyze the modes, the peaks were fitted to the calculated modes using the asymptotic expansion (39) or by directly solving (36) and (37). As an initial approximation for the droplet radius, the size calculated from the optical micrograph of the droplet was used. The radius of the droplet in the calculations was manually changed in small steps until the calculated modes matched the peaks in the spectrum. On Figure 36 there are examples for two droplets of different size. For the smaller droplet (Figure 36a) there is just one set of modes visible, that are identified as the TM modes with the radial mode number q equal to one (TM_l^1). The angular mode numbers l range from 86 to 80. Since the material parameters are not known exactly, the angular mode numbers l are determined with the precision of ±1. In the spectrum of the larger droplet (Figure 36a) also second radial TM modes are observed (TM_l^2). In even larger droplets TM modes with higher radial mode numbers and also TE modes become visible in the spectrum.

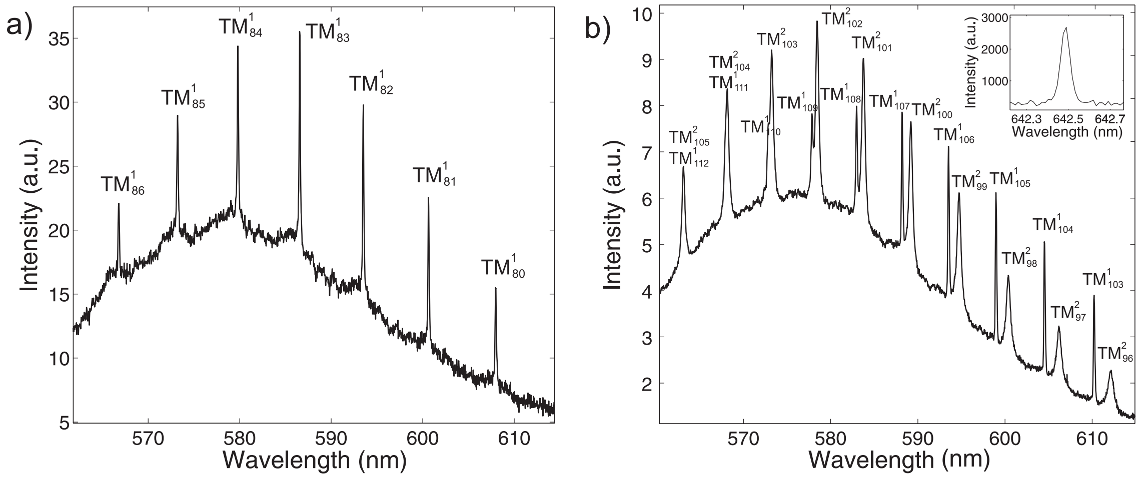

Figure 36: *Spectra of fluorescent light from two E12 droplets in PDMS.* a) A single set of WGM resonances is observed in a 10.1 µm droplet corresponding to modes with radial mode number equal to one (TM_l^1). b) In a larger droplet with diameter of 12.6 µm also second radial modes are visible (TM_l^2), they however have lower Q-factor. The inset shows high resolution spectra of a single spectral line in a large 53 µm droplet. The linewidth is 0.055 nm.

4.2.3 Q-factor

By using a high resolution Raman spectrometer we have measured the Q-factor in LC droplets. The measurements were performed on large droplets where the Q-factor should not be limited by the losses due to leakage, but because the intrinsic losses of the material and the surface roughness. For a 53 µm droplet the linewidth is found to be 0.055 nm which is limited by the spectrometer resolution. The corresponding Q-factor is > 12.000. The Q-factor could be much higher and ultimately limited by scattering of light on thermally induced orientational fluctuations of LC molecules. But unfortunately it is not possible to measure higher Q-factors using currently available spectrometers[1]. Even if the Q-factor is in reality not much higher that the currently measured 10^4, it is still quite high and enables the LC microresonators to be used in a number of applications. For smaller droplets the Q-factor is limited by the losses due to leakage. We have measured $Q = 4.000 - 6.000$ in $10 - 13$ µm droplets and $Q > 10.000$ in droplets larger than 30 µm. As a comparison, linewidths of emission lines that have been reported in lasing experiments in liquid crystals are of the order of $0.3 \sim 0.4nm$ in dye-doped cholesteric liquid crystals [41, 42], $0.11nm$

---

[1] We are currently building a setup that uses a narrow line tunable laser and tapered fiber coupling (Section 2.2.5.1) to measure the exact Q-factor of the LC droplets.

in dye-doped liquid crystal blue phases [5], and $0.06nm$ in an order parameter optimized dye-doped cholesteric liquid crystals (CLC) [43].

4.3 Electric field tuning of WGMs in nematic droplets

Once we were able to get nice WGMs in LC droplets embedded in PDMS, we have tried to apply electric field to the dispersion. We expected that the electric field will reorient the liquid crystal molecules and change optical path of certain polarization and thus enable the tuning of the modes. AC voltage is usually used for switching of liquid crystal cells in order to avoid ionic shielding [88]. In our case we have found out that the largest LC distortion is achieved at frequencies greater than 30 kHz, but above 300 kHz the amplitude on the amplifier is beginning to drop. We have therefore used some intermediate frequency of 50 kHz in all the experiments.

4.3.1 Director distortion under electric field

First, appearance of LC droplets was observed under the microscope as the electric field was applied. The evolution of the radial nematic structure in a spherical microdroplet with increasing electric field has been studied before [95]. In Figure 37 a 9.3 µm droplet is imaged under crossed polarizers and corresponding director fields are presented. At zero field, the droplet is in radial configuration with a radial hedgehog point defect at the center and is seen as a cross under the crossed polarizers (Figure 37a). As the field is applied, the molecules of the positive dielectric anisotropy LC are starting to rotate in the direction of the field. There is almost no distortion very near the surface because of the strong anchoring and no distortion also in the flat disk in the center of the droplet (Figure 37b). The radial hedgehog point defect is still in the center of the droplet. The director also rotates a little bit around the axis parallel to the filed, to lower the energy of the distorted region, as can be seen in the crossed polarizer image. The transition from completely radial configuration to this distorted configuration is continuous and completely reversible. Therefore, this range was used for the tuning of the WGMs. When higher field is applied, the structure of the droplet is transformed into a +1/2 defect ring recirculating the droplet at the surface and an almost uniform director configuration in the center (Figure 37c). Due to the conservation of topological charge [93] the radial hedgehog point defect cannot be annihilated, but can be transformed into other defect structures. In this case to a defect ring, that is similar, but of opposite winding number to the Saturn ring [96]. This transition happens at certain voltage threshold and it is discontinuous and non-reversible. When reducing the field back, the defect ring slowly shrinks (Figure 37d) until the point defect is formed again.

4.3.2 WGMs under electric field

The distortion of the nematic director inside the droplets should have large impact on the optical path length. At zero field, when the droplets are in radial configuration, TM modes that we observe, have the electric field in radial direction and therefore sense the extraordinary refractive index. When the electric field is applied, the molecules rotate and the TM modes sense lower index (Figure 38). This decreases the optical path length and the modes should shift to shorter wavelengths. At lower fields the rotation of the molecules is zero at the top and bottom of the droplet as well as in the plane perpendicular to the field (Figure 38a). At higher field when the transition to the ring configuration, the distortion that influences the WGMs the most, is located near the ring defect, represented as the shadowed area in Figure 38b.

The spectra of WGMs were observed as the electric field was gradually increased from zero up to 2.1 $\mathrm{V_{RMS}}/\mu\mathrm{m}$. The results for a 16 µm droplet are presented in Figure 39. The modes clearly shift to shorter wavelengths. Till 0.2 $\mathrm{V_{RMS}}/\mu\mathrm{m}$ the shifting is very small, but soon in becomes almost linear, but approaching saturation towards 2 $\mathrm{V_{RMS}}/\mu\mathrm{m}$. If the field is small enough that the transition to the ring configuration is not reached, the tuning has no hysteresis and is completely reversible. Two distinct sets of modes are visible, the modes

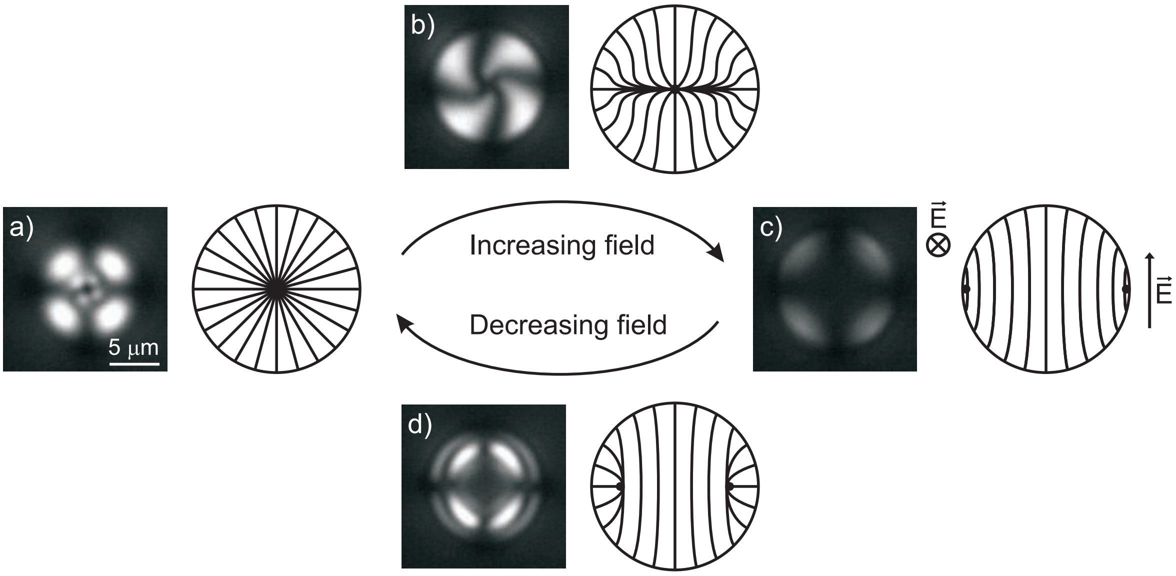

Figure 37: *Nematic droplet director configuration under applied electric field.* A 10 µm E12 droplet at increasing and decreasing electric field and the corresponding nematic director configuration from a side view. a) At zero field the droplet is in radial configuration, that is seen as a black cross under crossed polarizers. b) At small fields a disk like distortion is formed in the droplet, that also twists slightly. c) At higher field a defect ring appears perpendicular to the field and the director is quite uniform. d) When decreasing the field from the ring configuration, the ring slowly shrinks towards the center of the droplet.

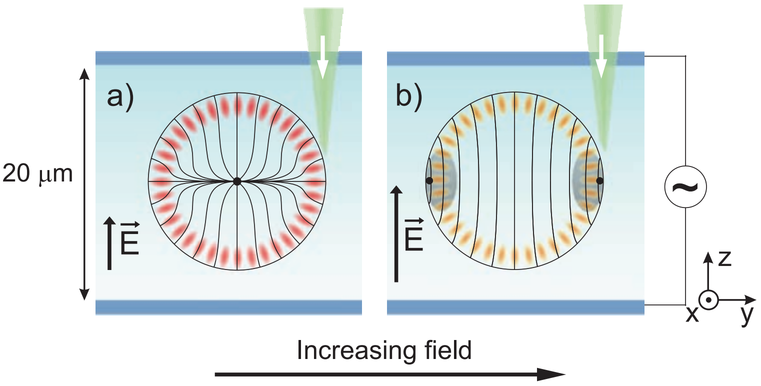

Figure 38: *Schematic drawing of the light circulation in a LC droplet* at a) small electric field and b) large field.

with radial mode number equal to one (TM_l^1) and the ones with radial mode number of two (TM_l^2). The first radial modes have smaller shift and smaller linewidth, that can be observed as thinner lines on Figure 39. The second radial modes on the other hand have higher tunability and are seen as wider lines. The reason for different tunability for different radial mode number is confinement of the modes. The TM_l^1 modes are confined very close to the surface of the droplet where the distortion of LC director under the effect of the electric field is small because of the strong anchoring. On the other hand, the modes with higher radial mode numbers are located more in the interior of the droplet where the distortion is larger. The tunability is also dependent on the size of the droplets (Figure 40), since in smaller droplets the effect of the anchoring is more important, meaning that the tunability is lower. The tunability is as high as 20 nm when 2.6 $\mathrm{V_{RMS}}/\mu\mathrm{m}$ is applied to a 17 μm diameter droplet. For most droplet sizes the tunability is larger than the free spectral range, meaning that the resonator frequencies can be shifted to any value.

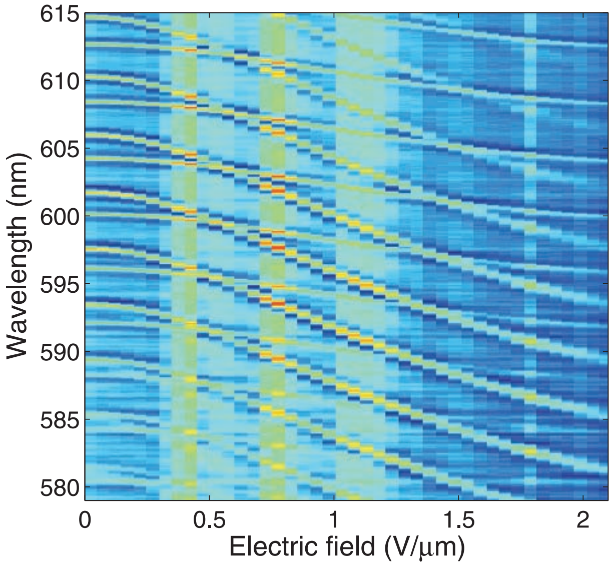

Figure 39: *WGM spectrum versus applied electric field.* Electric-field-induced wavelength shift of TM_l^1 and TM_l^2 WGM resonances in a 16.1 μm diameter microresonator made from dye doped E12 nematic liquid crystal. Color scale indicates intensity of detected light. Note the enhancement of the resonances at discrete wavelengths.

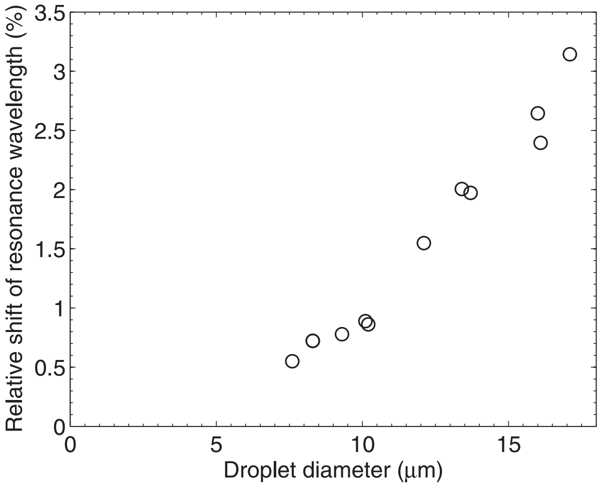

Figure 40: *WGM tunability as a function of droplet diameter.* Relative tunability of TM_l^2 modes when at an applied field of 2.6 $\mathrm{V_{RMS}}$ for different sizes of the droplets.

We can also estimate the maximum possible tunability at very high electric fields. In this case, all the molecules align perfectly in the direction of the electric field making an uniform director field configuration. The refractive index for TM modes can be calculated as

$$n(\phi) = \frac{n_o n_e}{\sqrt{{n_o}^2 \sin^2 \phi + {n_e}^2 \cos^2 \phi}}, \tag{83}$$

where ϕ is the angle between the direction perpendicular to the electric field and the position on the circumference of the droplet. By integrating this equation around the droplet we calculate the average refractive index. For E12 the difference in refractive index and therefore the optical path between radial and uniform configuration is 6.7%, enabling the tuning by 41 nm at 600 nm.

The experimentally achieved relative shift of modes (3%) in LC droplets is one to two orders of magnitude larger compared to already published values for electrical tuning. Electric tuning of WGMs has been till now achieved in a number of ways [12–15] including using liquid crystals [12, 13].

In the WGM spectrum, as the field is increased, we do not observe just shifting of the modes to shorter wavelength but also the intensity of the modes changes (Figure 39). At certain values of electric field a sharp enhancement of the intensity of the modes as well as the fluorescent background is observed (Figure 41a). This happens when a WGM frequency is matched to the frequency of the argon pump laser (514.5 nm) [97], schematically shown in Figure 41b. When this condition is met, more excitation light is coupled into the microresonator increasing the intensity of the fluorescence and therefore the intensity of all the modes and of the fluorescent background.

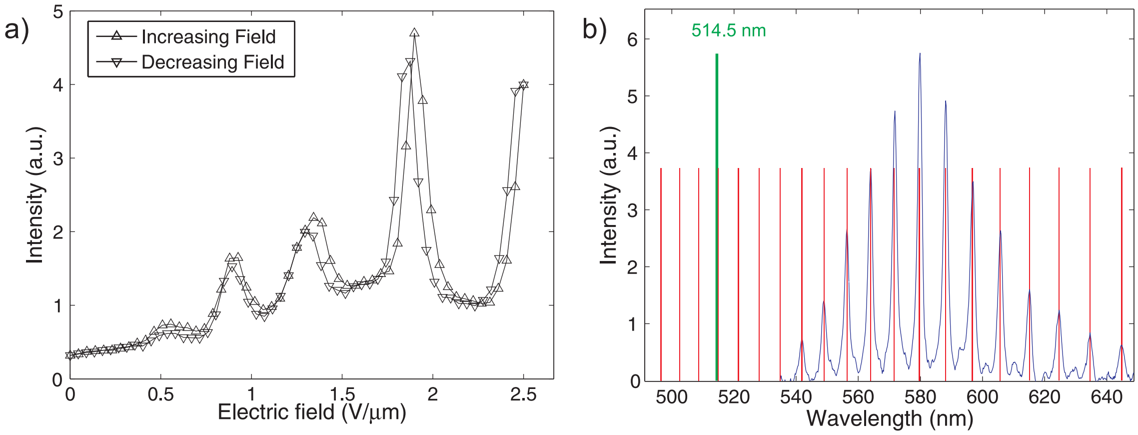

Figure 41: *Intensity oscillation under field.* a) Summed intensity of all WGMs calculated from Figure 39 as the electric field is increased and back decreased. b) Background corrected spectrum from a LC droplet fitted with calculated positions of WGMs. The electric field shifts positions of all the modes by the same percentage. When one mode matches the excitation laser wavelength (green vertical line) the intensity increase is observed.

Another very important aspect of tuning is the speed, so how fast we can switch the frequencies. At the time of these measurements we did not have a spectrometer fast enough to measure the switching speed, therefore we used a different method. A droplet was switched between two electric field amplitudes, where at one amplitude a WGM matched the argon pump laser, and at the second amplitude it did not. In the first case more light was coupled into the droplet, so it was emitting more light. The intensity of light was measured by photomultiplier. The switching time was found to be approximately 10 ms for both switching the field on or off. The time is a little bit faster for smaller droplets and slower for larger. This is not nearly fast enough for fast speed modulation, especially nowadays when the optical telecommunications have achieved enormous speeds. However, it still fast enough to be used for some slower applications that need large tunability.

4.3.3 Tuning of multiple droplets

In Section 4.1 we have shown that the droplets can be assembled into structures so that they are positioned close to each other. The coupling between the LC microcavities enables the light to be transferred from one to the other. However, for the process to be effective, the frequencies of two neighboring microcavities should match precisely. The frequencies can be matched already when manufacturing the microcavities, but in the case of LC droplets this is not possible, since they are made just by mechanical mixing and are very polydispersed. However, the LC microcavities are tunable. If we have two droplets of different size, their tunability is also different, and when increasing the electric field, at one point, the mode frequencies match (Figure 42). At that point, the light in the two droplets is coupled and can be transferred from one to the other. However, this works just for two droplets, with three or more, we can not achieve frequency matching. In this case, more electrodes should be made so that each droplet could be addressed and tuned independently.

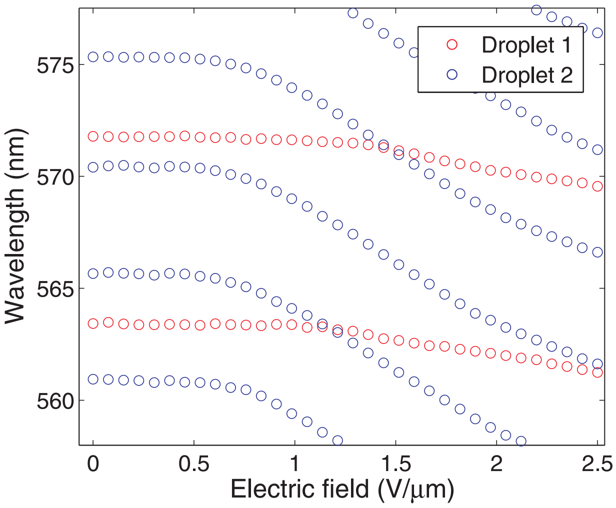

Figure 42: *Tunability of two droplets.* Positions of WGMs in two separated LC microdroplets of different size as the electric field is increased. Droplet 1 has the diameter of 7.8 µm and droplet 2 has the diameter of 12.8 µm.

4.3.4 In-plane electric field

To confirm and better understand the results of electric field tunability, we also used in-plane electric field. A gap of 60 µm was etched into ITO that was used as an electrode. Voltage of 70 V_{RMS} was applied between the electrodes and the droplets in the gap were observed under optical microscope and the spectra of WGMs was measured. The electric field in between the electrodes is not uniform, but still good enough to see its effects and make good estimations of tunability. When applying electric filed, we clearly see that the distortion of the director field (Figure 43) matches the configuration shown in Figure 37b. However, the field is not strong enough to induce the configuration with the ring in the droplet (Figure 37c).

The WGMs were measured in two orthogonal directions, perpendicular to the electric field (Figure 44a) and parallel to the field (Figure 44b). This was simply achieved by selecting the appropriate laser excitation point. The positions of one mode in the perpendicular and in the parallel direction as the amplitude of the electric field is increases are shown in Figure 44c. In the disc through the center of the droplet, perpendicular to the field, there is no reorientation of the LC molecules, since they point all the time perpendicular to the electric field. Therefore, in the perpendicular direction the modes do not shift considerably. In the

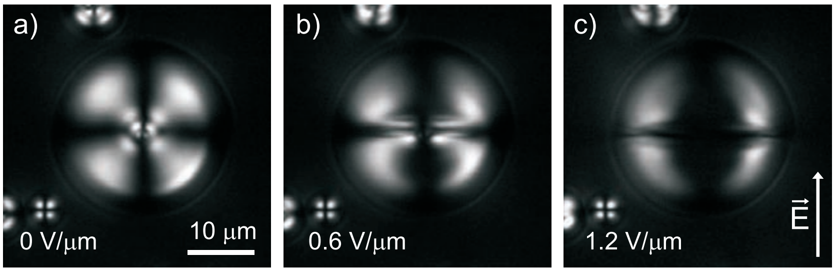

Figure 43: *Images of a droplet with in-plane field.* The electric field is applied in the direction perpendicular to the direction of viewing. A clear distortion is visible with a non-distorted disc in the center.

other direction the situation is the same as with planar electrodes (Figure 38a). The mode shift is of 0.9 nm, which is however considerably less than we get with planar electrodes at similar electric fields and size of the droplet. The difference can probably be explained by the non-uniformity of the electric field between the electrodes. The droplet was not in the center between the electrodes and it was also at a vertical distance from the electrodes that is comparable to the gap distance. Because the droplet is embedded in polymerized PDMS, we did not observe any geometrical deformation, so that the tuning is purely caused by director reorientation and therefore the change in the refractive index.

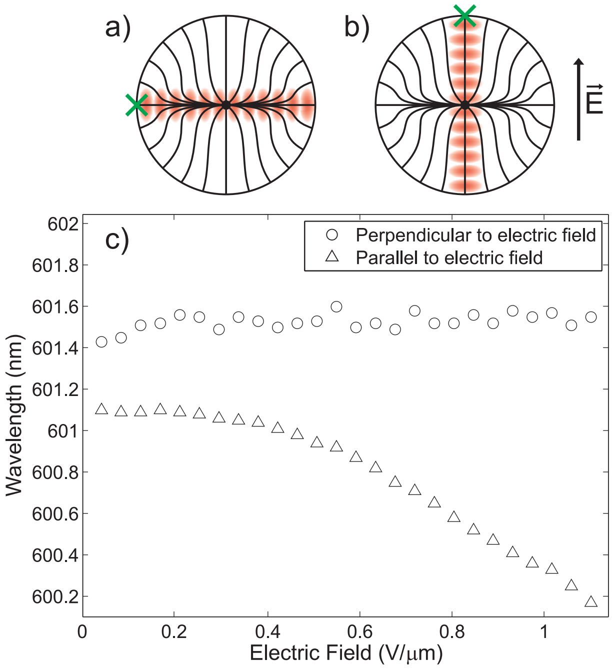

Figure 44: *Tunability with in-plane field.* Scheme of the WGMs circulating in a plane a) perpendicular to the electric field and b) parallel to the filed. The green cross represents the point of the excitation laser. c) Position of a WGM in a 17 µm diameter droplet for the two directions as the electric field is increased up to 1.1 V/µm.

4.3.5 Electric field with droplets containing particles

We have shown in Section 4.1 that droplets containing microparticles can be produced easily. We have tried to apply electric field to them. If there is just one particle in the center of the droplet, by applying electric field, it does not move or change in other way the properties of the droplet. But if there are two particles in the droplet, when applying electric field, they move to the surface (Figure 45). This can be useful for selecting modes with different radial mode numbers. The particles should be in this case fluorescent. Depending on their position inside the droplet, the fluorescent light from the particles would excite different radial modes. This is possible because the higher the radial mode, more deep into the droplet it is extending.

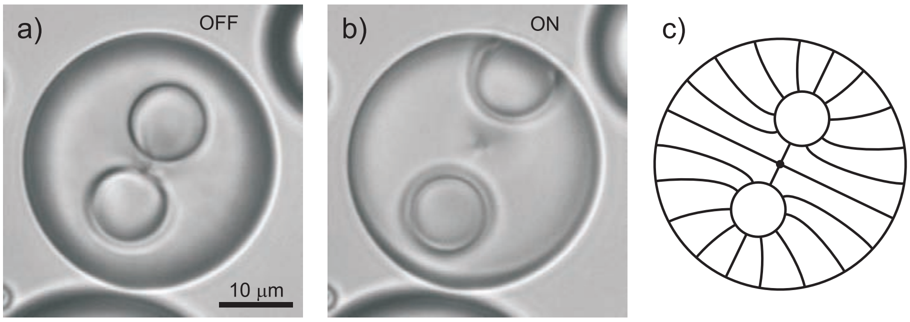

Figure 45: *A LC droplet containing pericles.* A 34 μm droplet of LC in PDMS containing two melamine formaldehyde particles a) at zero electric field and b) at applied electric field.

4.4 Temperature tuning

WGMs from a E12 droplet in 20 mM SDS solution in water were studied as temperature was increased from room temperature to above the clearing point of the LC. Spectrum for a 24 µm droplet as a function of temperature is presented in Figure 46. Several distinct spectral lines are observed, which shift at different rates and in different directions. There are six sets of modes with different polarization and radial mode number: TM_l^1, TM_l^2, TM_l^3, TM_l^4, TE_l^1 and TE_l^2. The TM modes shift to shorter wavelengths, while the TE modes shift to longer wavelengths. The TM polarization is associated with extraordinary refractive index, which decreases with temperature and the TE polarization is associated with ordinary refractive index, which on the other hand increases with temperature. This agrees with the negative shift of TM WGMs and positive shift of TE WGMs. The shift is almost proportional to the change of the refractive index and qualitatively matches with the plot of refractive index change (Figure 15).

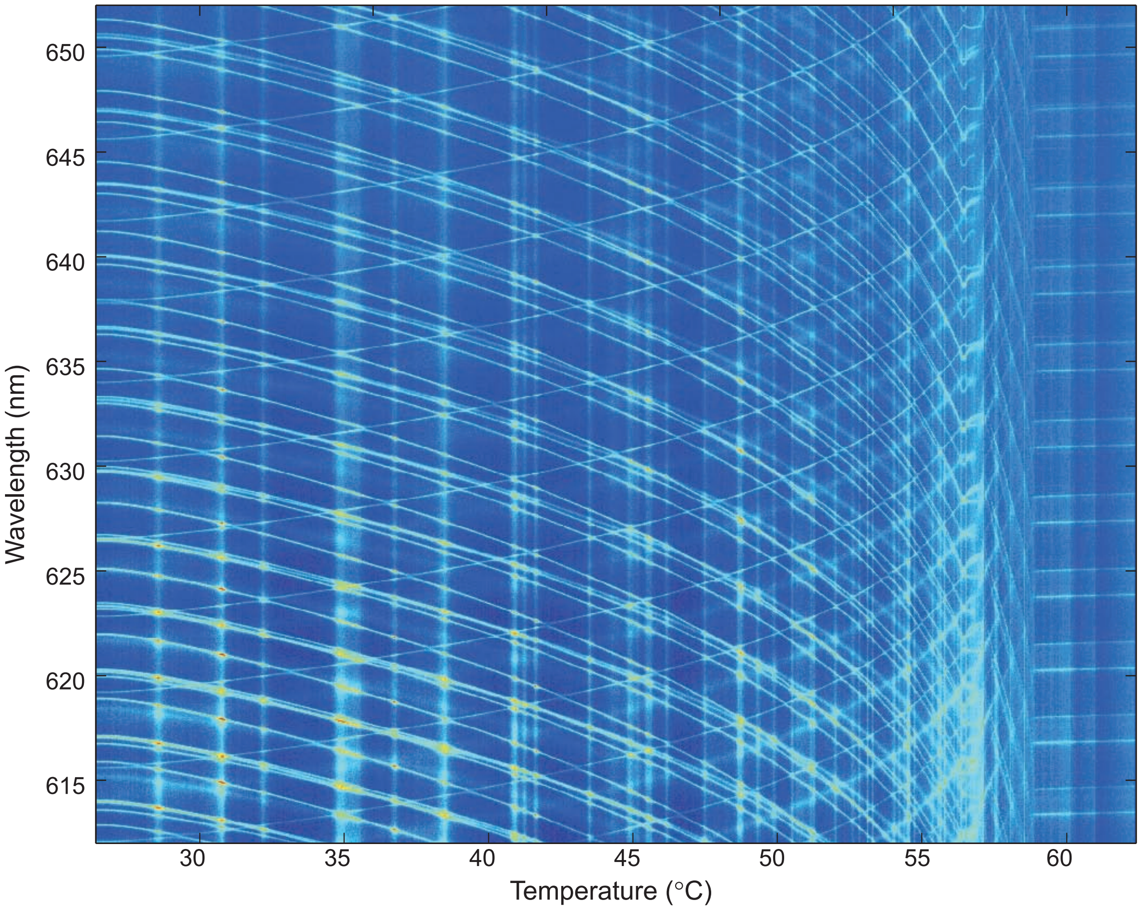

Figure 46: *Temperature tunability of WGMs.* Positions of the optical modes in a 24 µm diameter E12 droplet as the temperature is increased.

Figure 47 shows the calculated positions of the modes for a 24 µm E12 droplet as the temperature is increased. The refractive index was calculated using (74) and (75). Refractive index was than used in (39) to calculate the positions of the WGM modes. The calculations agree well with the experimental data.

Both in the experiment and in the calculations the modes with different radial mode numbers have slightly different tunability. The WGMs with higher radial mode numbers shift less that the WGMs with lower. We believe that the reason for this is the lower confinement of higher modes. That means that for modes with higher radial mode number a larger part of the total optical electric field of the mode is outside the droplet. This part is

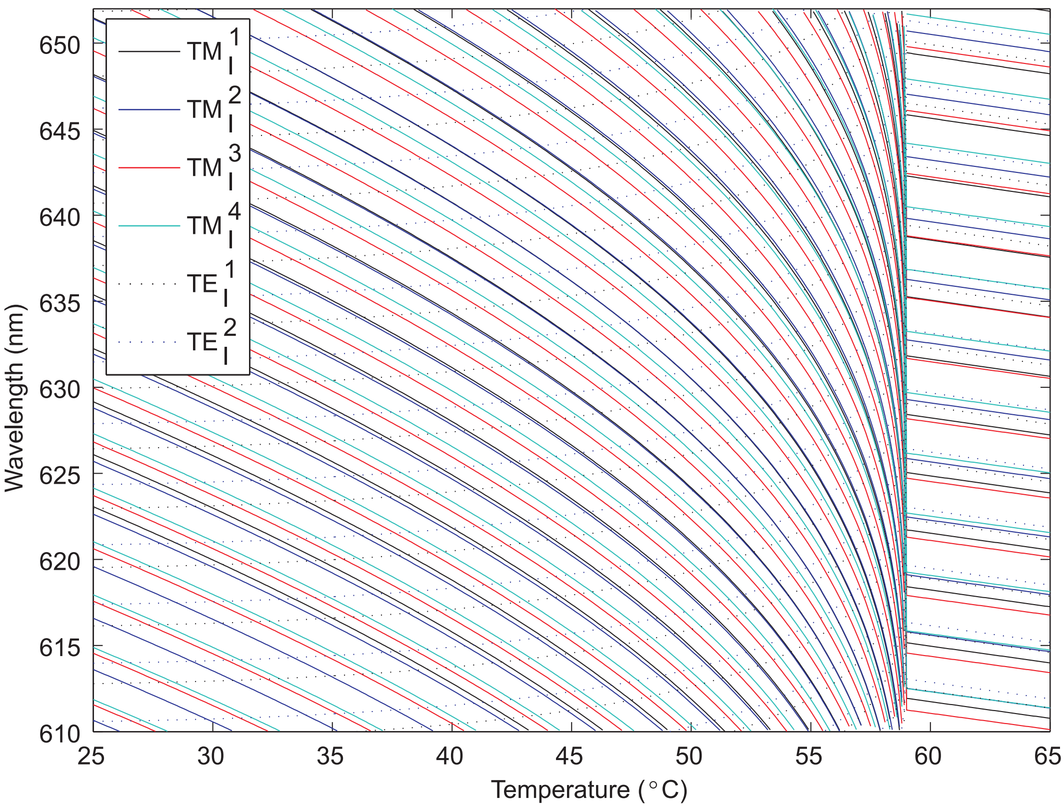

Figure 47: *Calculation of temperature tunability of WGMs (large droplet).* Calculated positions of six different WGMs in a 24 µm E12 droplet.

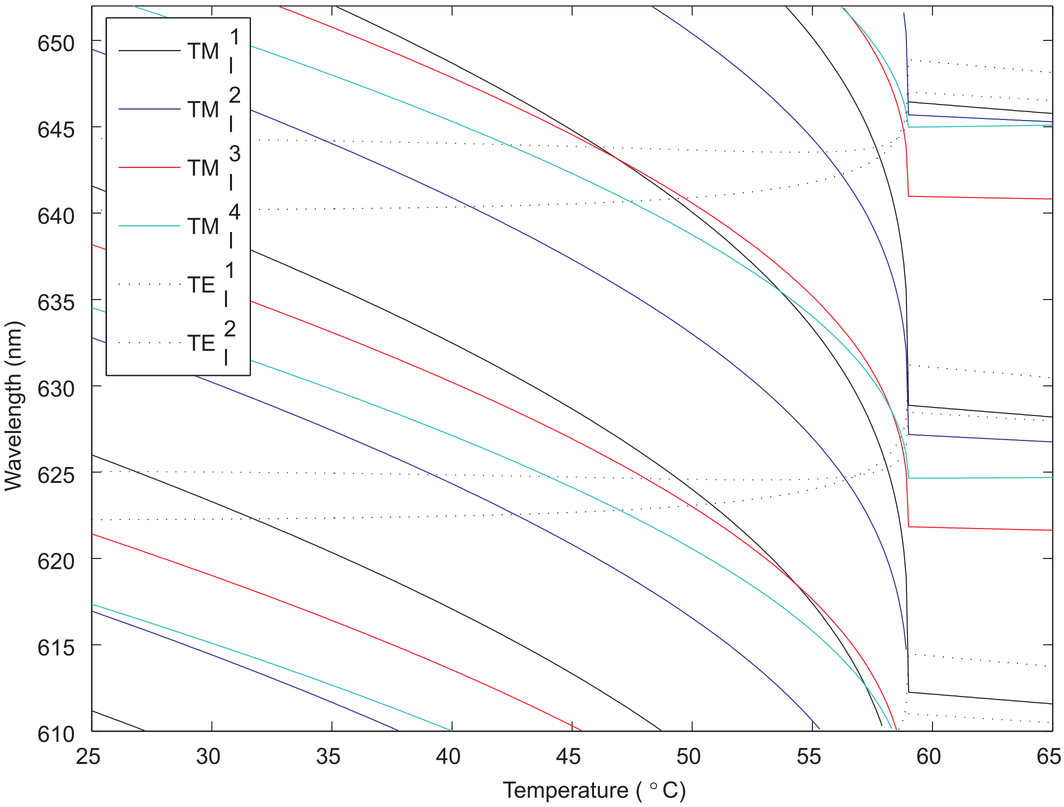

Figure 48: *Calculation of temperature tunability of WGMs (small droplet).* Calculated positions of six different WGMs in a 5 µm E12 droplet.

dependent on the refractive index of the surrounding medium, that doses not change much with temperature. This effect is more pronounced in small droplets where the higher modes are less confined. As an illustration, mode shifts were calculated for a 5 µm droplet (Figure 48). The lower shift of the higher modes is evident, since this is more pronounced that in larger droplets.

However, the different shift of modes with different radial mode numbers may not be adequately explained by just different confinement of the modes. There are other factors that may need to be considered. The calculations take into account the bulk refractive index, however, the WGMs circulate close to the interface between the LC and water. The anchoring can have an effect on the refractive index, since in can impose additional order to the LC molecules. Additionally, we have a liquid interface covered by surfactant that can absorb/desorb when the temperature is changed, thus changing the size of the droplet as well as the anchoring.

The shift in TM WGMs wavelengths is approximately 15 nm for the temperature change from 25°C to 55°C. The thermal coefficient is changing with temperature, the average coefficient in this temperature range is 0.5 nm/°C. The LC microresonator can be in this case also used as a thermometer. The accuracy with which it is possible to measure the position of a single WGM can be approximated by the FWHM of the spectral line. For LC droplets the highest Q-factor measured was 12.000 limited by the resolution of the spectrometer, corresponding to linewidth of 0.05 nm. From this number and thermal coefficient we calculate that the resolution of our temperature sensor is 100 mK. This is not a very good thermometer. However, this number is possibly lower, since the Q-factor is probably larger. The thermal coefficient can also be increased by using the LC microresonator close to the transition temperature.

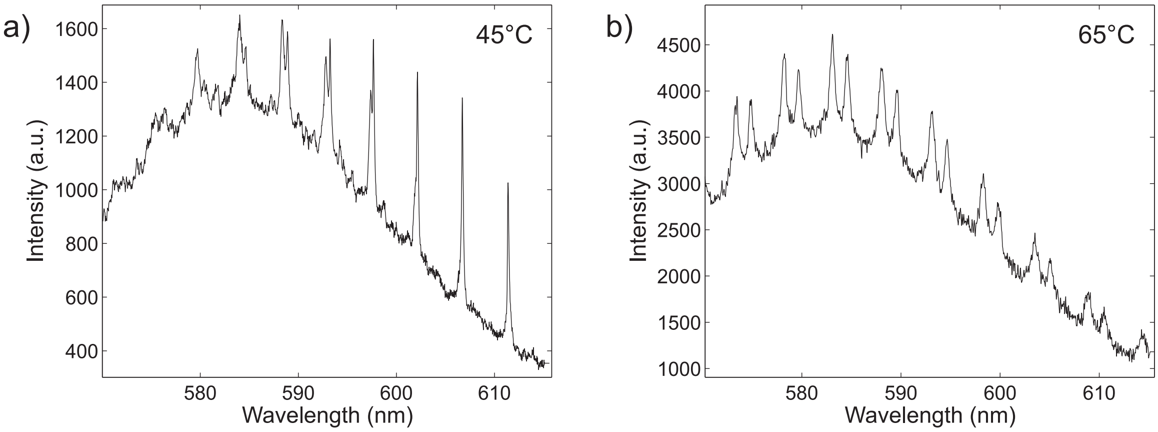

Figure 49: *WGM spectra at two temperatures.* a) In nematic phase we can observe first and second radial mode with TM polarization. b) In isotropic phase a typical doublets of TE/TM modes are visible.

When we further increase the temperature and approach the clearing temperature (59°C) the modes begin to shift in a more chaotic way. The chaotic temperature range is just around two degree wide and as soon as we reach the isotropic phase the modes are again clearly visible. The changes in the spectra in the chaotic temperature range can be explained by changes in the director configuration inside the LC droplet and local melting of the LC. In Figure 50 an image sequence of a LC droplet under crossed polarizers is presented as the temperature is slowly increased. As the clearing point is approached, the internal configuration of the nematic director is changing, but can not be clearly identified. A ring seems to appear in the center and then expand to the surface. At even higher temperature melting into isotropic phase starts at one part of the droplet and fast spreads to the entire LC.

These changes happen in an unpredictable way and are not repeatable nor reversible. That is why this temperature range is not useful for tuning the resonator or using it as a temperature sensor. Furthermore, the refractive index in this temperature range is nonuniform across the droplet. This can lead to scattering of light, splitting of modes and a reduction in Q-factor. In some cases, especially with smaller droplets the modes also disappear in this range.

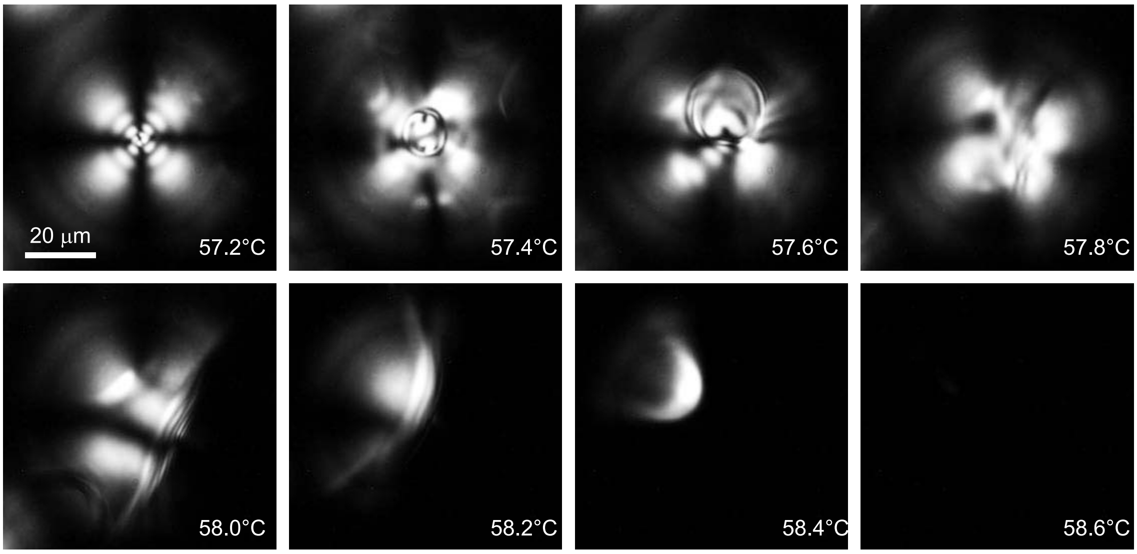

Figure 50: *Image of a LC droplet with increasing temperature.* A droplet of E12 under crossed polarizers when the temperature is increased from 57.2°C to 58.6°C. At first a ring can be observed expanding from the center, changing the director configuration. Close to the clearing temperature a part of the droplets starts to melt to isotropic phase.

Above $\sim 59°C$ the transition into isotropic phase is complete. Now both TE and TM modes have the same refractive index and are visible as pairs. However, it is not clear why less modes are visible in the isotropic phase than in the nematic. The average refractive index remains almost unchanged when the transition occurs, so almost the same number of modes should be visible. With further increasing temperature, the modes do not experience any large shift any more. This is reasonable, since the refractive index does not change much in isotropic phase. However, the calculations of the refractive index show that the modes should shift to shorter wavelengths, but in the experiment they shift slightly to longer wavelengths. The refractive index decreasing with temperature in isotropic phase is attributed mainly to the decrease in the density of the material because of thermal expansion. With decreasing density also the size of the droplet increases. The increase of size has the opposite effect to the WGMs as the decrease in refractive index, so that this two effects approximately cancel out. This matches the almost zero shift of modes in isotropic phase observed in the experiment.

In the temperature dependance of WGMs (Figure 46) a hint of mode splitting can be observed. When a TM mode intersects with a TE mode, they do not cross each other, but they are rather 'repelled' from each other. The mode splitting is dependent on coupling strength between the two modes in this case the modes with different polarizations. The two polarizations should be somehow coupled to explain the mode splitting. In liquid crystals this is possible through scattering on thermal fluctuations of the director [98]. The fluctuations are larger at higher temperatures, which matches the experiment where we observe mode splitting just at higher temperature. However, to indubitably confirm the mode splitting, the spectrometer resolution is not high enough. A different technique with higher resolution, such as tapered fiber coupling (Chapter 2.2.5.1) should be used to study this process.

Finally, we can discuss also the change of the Q-factors with temperature. The Q-factor is mainly dependent on absorbtion, surface roughness, leaking of the modes and scattering because thermal fluctuations in LC (Section 2.1.1). Absorbtion and surface roughness are in principle not very temperature dependent. The Q-factor reduction caused by the leaking of modes because of the curvature is dependent on the size of the droplet and the refractive index contrast between the interior and exterior of the droplet. The refractive index of the LC changes with temperature and so does the contrast. For TM modes the index contrast decreases with temperature, so the Q-factor should also decrease. This is indeed observed in the experiment and presented in Figure 51. At temperatures higher than 38°C the TM_l^2 modes become to wide and of too low intensity to measure their widths. The linewidths of TE modes were not measured, since for them to be visible the droplet should be large enough, but then there are a lot of TM modes present that overlap with each other and it is therefore difficult to measure the linewidhts. However, in Figure 46 it can be clearly seen that the TE_l^2 mode is not visible at room temperature, but at higher temperatures is becomes visible and narrower. The contribution to the reduction of the Q-factor because the scattering on thermal fluctuations is difficult to estimate. At least for the TE modes we can say that the leaking has higher contribution than the fluctuations, since the Q-factor increases with temperature. In general the fluctuation contribution should have almost the same effect on all modes. At high temperature some TM modes still have narrower linewidth than the spectrometer resolution. So this contribution probably can not be measured with our spectrometer. Again, a higher resolution technique is needed also in this case (Chapter 2.2.5.1).

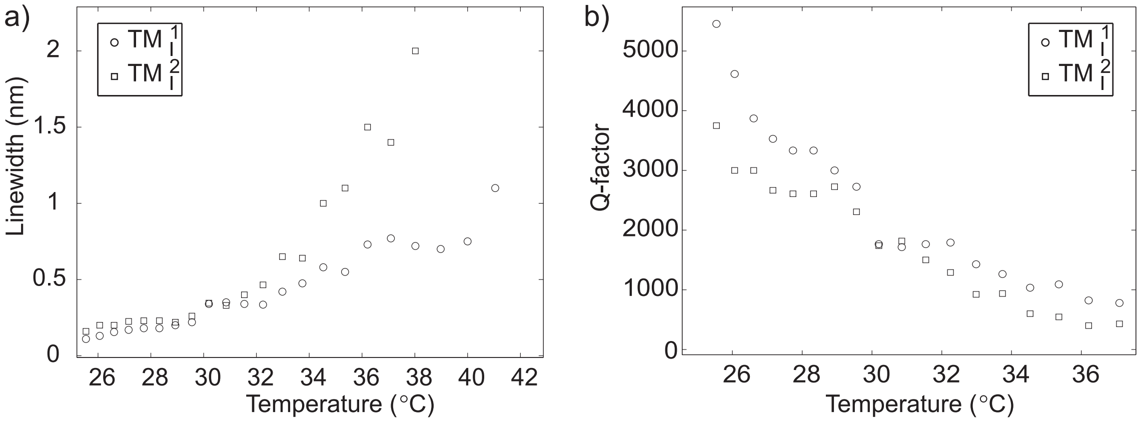

Figure 51: *Linewidth and Q-factor as a function of temperature.* Spectral linewidths of two TM modes were measured in a 16.4 µm diameter droplet. Clear increase in a) linewidth or equivalently b) decrease of the Q-factor can be observed. To measure the linewidth, the spectral lines closest to 600 nm were used.

4.5 Optical tuning

Apart from electric and temperature tuning we have also tried tuning by laser beam. It is known that by using a powerful laser beam, a distortion in the nematic director can be created above the optical Fredericks transition [99]. By changing the director we also change the refractive index and so we should be able to tune the WGMs. Laser tweezers setup was used to tightly focus the IR laser beam (1064 nm) to a droplet. The Ar-ion laser (514.5 nm) was used to excite the WGMs. The IR laser power was slowly increased up to 140 mW and spectra were acquired. The results presented in Figure 52 are almost identical to the case of temperature tuning (Figure 46). This result already suggests that the droplet is heated by the laser beam, which consequently causes mode shifting. We tested this hypothesis by placing two droplets at a distance of 100 µm. Mode tuning was measured on both droplets, but only one droplet was illuminated by IR laser of increasing power. We have found out that the mode shift is almost the same for both droplets. This can be explained by heat transfer through the sample. If a nearby droplet is heated, the heat is transferred also to the other droplets, that also experience the mode tuning. An additional mechanism for mode shifting could also be the mechanical deformation of the droplet by optical forces in the laser trap. This kind of tuning was already observed in isotropic droplets [100]. In the case of deformation (Chapter 2.2.3) the TE and TM modes should shift in the same direction. We have not observed this and we believe that the deformation contribution is negligible in our case.

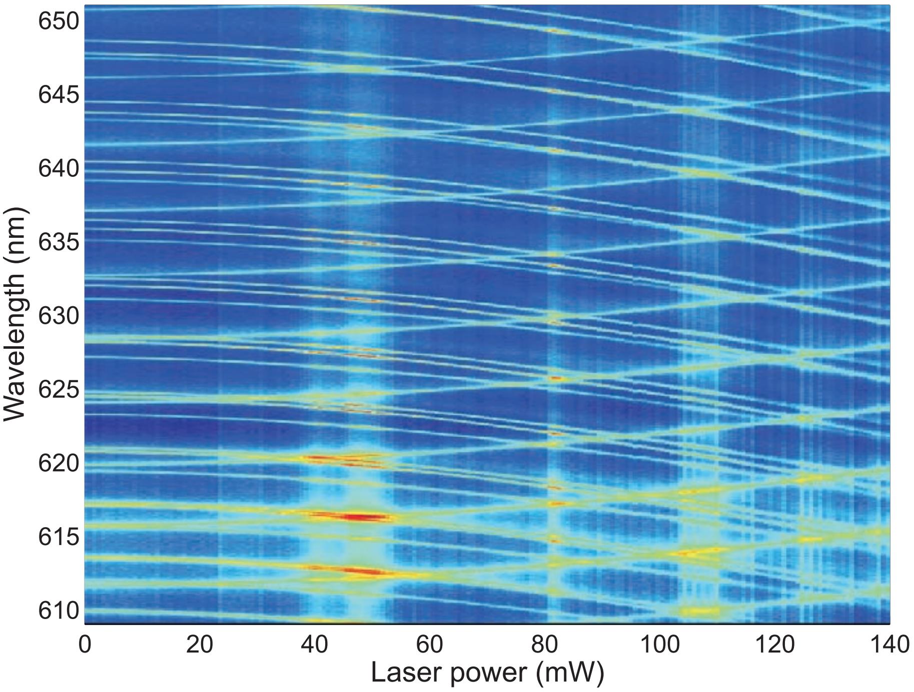

Figure 52: *Optical tuning of WGMs.* Positions of WGMs in a 16 µm 5CB droplet as it is illuminated by IR laser tweezers with the power increasing from 0 to 140 mW.

We further confirmed the absence of optical tuning by directly observing the internal structure of the droplet when illuminated by the laser beam (Figure 53). The droplets were embedded in PDMS which was polymerized to fix the droplets. The focused laser beam was then moved across the droplet and images under crossed polarizers were taken. It can be clearly observed that we can actually move the central point defect by pushing it with the trap. However, because of strong homeotropic anchoring, we can not change the director configuration close to the edge of the droplet. The WGMs are located very close to the surface and if the index can not be changed there, the WGMs are not affected by the laser beam. We could of course increase the laser power, but then the thermal effects are already very large and the LC finally melts to isotropic phase.

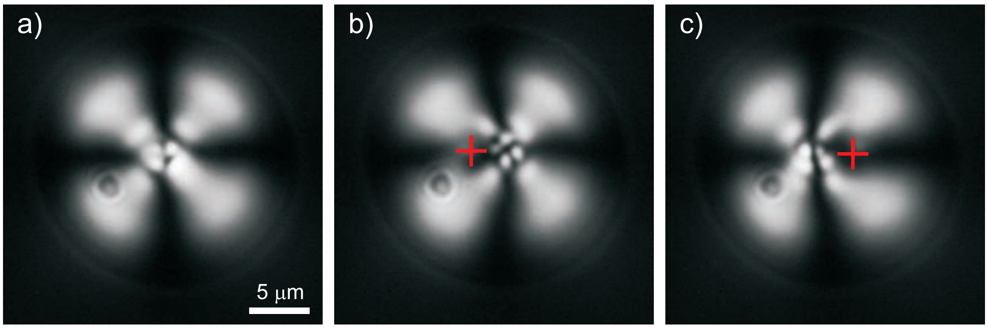

Figure 53: *Optical manipulation of the LC in a droplet.* Manipulation of the director configuration in a 22 μm 5CB droplet using the IR tweezers imaged under crossed polarizers. a) The laser is off and the droplet is showing typical cross. b) and c) laser trap (red cross) is moved across the droplet pushing the central defect slightly.

4.6 Strain tuning

One way of tuning the WGM microcavities is also by mechanical deformation. When strain is applied the microcavities the geometrical path of the light is changed, usually in different way in different directions. Strain tuning has been achieved before in a number of different geometries and materials. Two examples are droplets of a liquid in a PDMS polymer [19] and fused silica microresonators [16]. In both cases the achieved tunability was approximately 1 nm in visible light.

The shift of WGM modes was observed as the free standing PDMS film containing the 5CB droplets was stretched. All the droplets in the film were in the beginning of a spherical shape (Figure 54a) and by applying strain they deformed into prolate ellipsoids (Figure 54b). To excite WGMs, an Ar+ laser was focused to the rim of the droplet on one side of longer ellipsoid axis, so that the light was circulating in the plane parallel to the deformation (Figure 54c). After the spectrum was measured, the micrometer screw was rotated and the film further stretched. This caused the droplet to move towards the stretching direction, so the sample was than manually repositioned back, so that the laser beam was again in the original position. This was repeated in small steps until the maximal strain of 15% was achieved. In the spectra only one set of WGM modes were observed, matching the TM_l^1 modes. Because of small droplet size higher radial modes did not have large Q-factor enough to be observed. As well the TE_l^1 were not present since they sense the ordinary refractive index that is much lower than for TM modes.

The results presented in Figure 54d show position of modes from TM_{114}^1 to TM_{134}^1 plotted versus strain. When the strain is increased all the WGMs shift to longer wavelengths. The shift is caused by the increase in the optical path of the light traveling around the droplet in the plane parallel to the applied strain. When the strain was increased from zero to the maximal value, the mode at 590.4 nm shifted to 622.1 nm (Figure 54d), the tunability being 31.7 nm or 5.4%. Modes at other wavelengths were shifted by the same percentage.

Taking into account the applied strain we can calculate the change in the circumference of the droplet. We have measured the actual major and minor axes of the droplet using optical micrographs (Figure 54a and b). The diameter of the droplet before the applied strain was 14.4 µm. After the strain the axes were 13.2 µm and 16.9 µm corresponding to a relative change of −6.4% and 15.8%. The major axis length change agrees with the applied strain of 15.1%. The initial circumference of the droplet was 90.2 µm. After the stretching the ellipsoid circumference is calculated as

$$C = 4aE(\varepsilon) \tag{84}$$

where

$$\varepsilon^2 = 1 - \left(\frac{b}{a}\right)^2 \tag{85}$$

is the ellipsoid eccentricity, E is complete elliptic integral of the second kind, a is the semi-major axis and b is semi-minor axis. The new circumference now being 94.9 µm, corresponding to a relative change of 5.2%. This change agrees well with the actual optical mode shift of 5.4%

We know that for non-spherical shape WGM microcavities the modes with different azimuthal mode numbers are not degenerate any more (see Section 2.2.3). Light in different planes of circulation travels different optical path, therefore we should observe mode splitting. By using (44) we calculate that the mode splitting at 15.1% strain should be equal to 0.65 nm. However, no mode splitting is observed in the experiments. The reason for this is the use of an old spectrometer with the resolution of 1.5 nm, which is clearly not enough for the discrimination of single modes. By using tightly focused laser as a illumination, probably just few modes near the illumination spot were excited, corresponding to different azimuthal mode numbers. These modes were measured by the spectrometer as a single broader line.

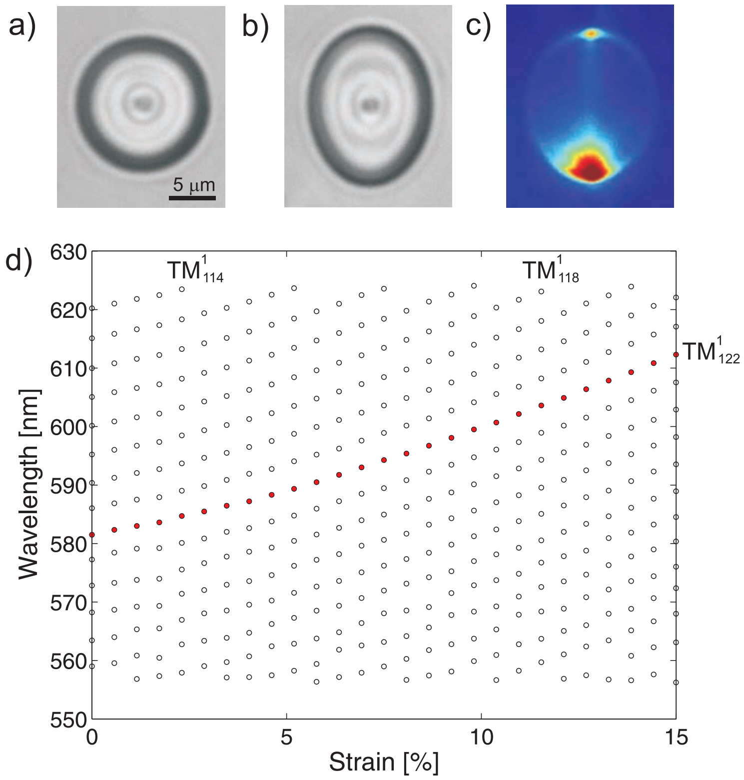

Figure 54: *Images and WGM positions of a LC droplet under increasing strain.* a) A LC droplet 14.4 μm in diameter embedded in PDMS polymer at 0% strain and b) at 15% strain. c) Fluorescent intensity at 7.4% strain. The droplet was illuminated by a laser near its rim at the lower part of the image. d) Positions of the optical modes as the strain is increased.

The shift of the WGMs could be also a consequence of change in the director configuration in the droplet. The mechanical deformation of the droplet could induce significant changes in the director configuration. This would change the refractive index and additionally modify the optical path for the circulating light. However, in the experiment we can not see any change of the texture under crossed polarizers. The director field is just stretched as if the droplet was solid. The magnitude of the tuning also well matches to just mechanical deformation. Therefore, we are confident that the tuning of WGMs is purely caused by physical length change of the light path. One could now ask, why not to use just an droplet of isotropic liquid, since the tuning would be the same. There are several advantages in using a LC droplet. First of all, the TE and TM modes are dependent on different refractive indices, the ordinary and extraordinary and are therefore decoupled. By choosing the right indices we can change the free spectral range and positions of both polarization individually. If one index is much higher than the other one, just one polarization can have the Q-factor large enough to be visible. In this case the mode structure in the droplet simplifies considerably. This is indeed the case in our experiments. Furthermore, by using LC microresonators we can at the same time tune the modes also by temperature and electric field.

4.7 Chemical sensors based on WGMs in LC droplets

The idea was to combine two chemical sensing methods, the fist one based on anchoring of liquid crystals (Section 1.3.3) and the second, sensing by using WGM (Section 1.1.2). A dye doped nematic droplet is used as a sensor. In this case, a molecule attaching to the resonator does not change the index of refraction only because its dielectric properties, but has an long range effect on other LC molecules. It reorients the LC molecules thus causing a change in the index of refraction of a large area on the resonator surface. A single molecule could in this way shift the resonance peak much more that with the existing WGM sensors.

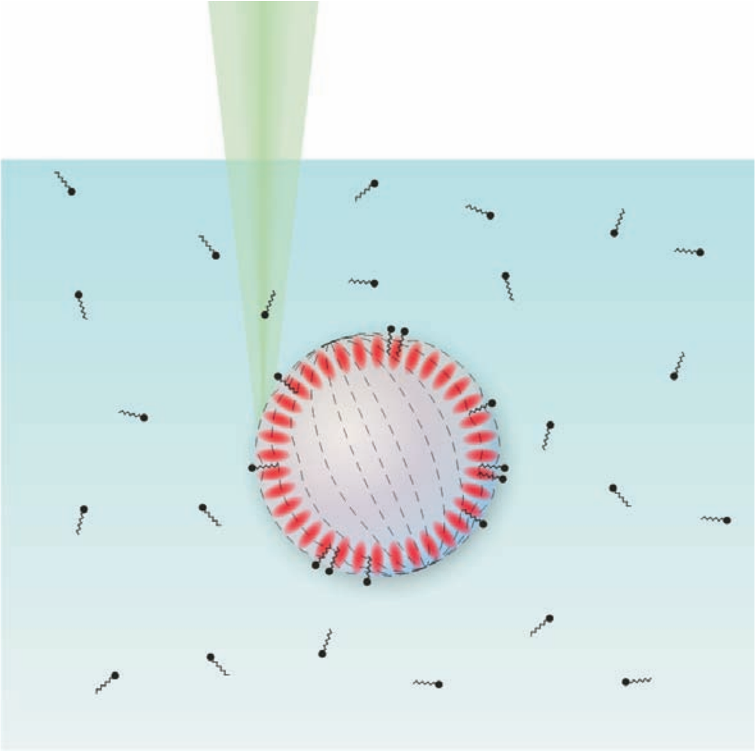

Figure 55: *Artist impression of a WGM LC chemical sensor.* A LC droplet is floating in a solution of surfactant molecules that are adsorbed on the surface and change the LC anchoring. A laser is used to excite the WGMs in the droplet through which the changes in molecular orientation ca be detected.

4.7.1 LC droplets at different surfactant concentrations

Before we have started measuring the optical modes inside LC droplets for sensing purposes, we have first repeated previously published results on director configuration in the droplets at different surfactant concentrations [65]. We have studied the same combination of liquid crystal (5CB) and surfactant (SDS) since it is a well known system. We have observed LC droplets under the microscope under different concentrations of SDS, ranging from 0 to 2 mM. In these experiments the microfluidic device was not used, but instead dispersions of different concentrations were prepared, filled in between two clean glasses and sealed. In Figure 56 there are the proposed nematic director configurations in droplets (Figure 56a), bright field (Figure 56b) and crossed polarizers (Figure 56c) images of selected 17 μm 5CB droplets at increasing SDS concentrations. In pure water the anchoring is planar and the structure should be bipolar with two surface boojums at the two ends. However, the two boojums are rarely observed in the experiment, probably because the anchoring is not perfectly planar, because of impurities in water. If we add for example 5% PVA to the water, strong planar anchoring is achieved, and the two boojums are clearly visible. However, in our experiments in pure water, the boojums are probably outside the droplet and the director field is more uniform. When the concentration of SDS is increased, the anchoring tilt angle continuously and spatially uniformly changes from planar to completely homeotropic [91]. At the SDS concentration of 0.2 mM, the bipolar configuration transforms into a single defect loop, encircling the microdroplet at the equator. When the concentration is further increased, the ring starts to move to the surface in one direction and gradually shrinks into a surface radial hedgehog point defect. The point defect than sinks into the center of the droplet, finally making the perfect radial structure at approximately 2 mM concentration of SDS. The whole sequence of director configuration transformations is quasi continuous, except for the formation of the ring at low concentrations.

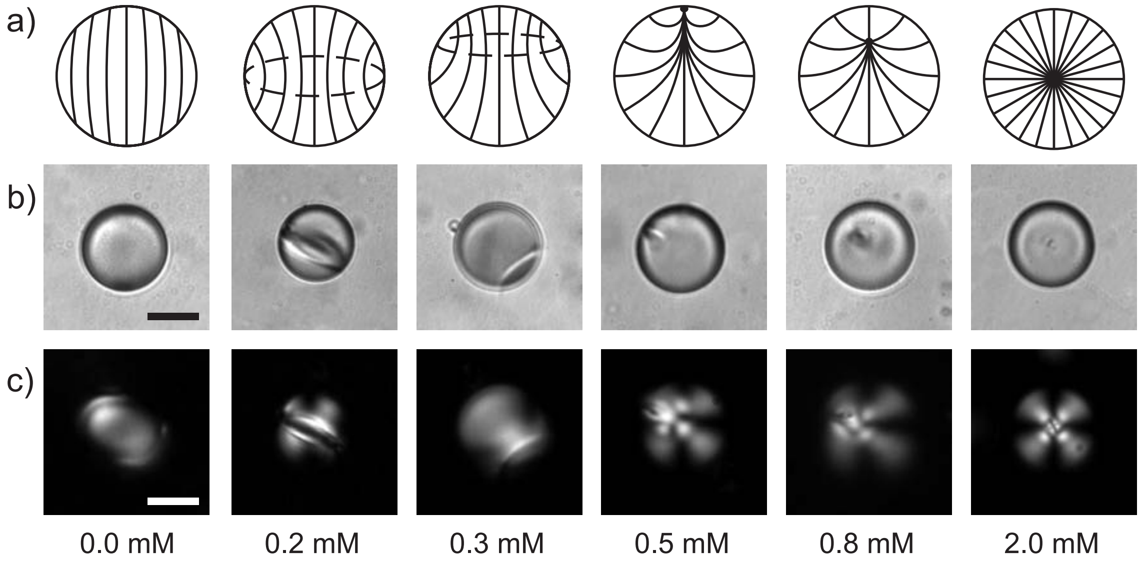

Figure 56: *Sequence of LC droplets at increasing SDS concentration.* The concentration ranges from 0 to 2 mM. a) Proposed nematic liquid-crystal director configuration in droplets at this concentrations. b) Bright field optical microscope images of ∼ 17 µm diameter 5CB microdroplets in SDS solutions. c) The same images as in b), taken between crossed polarizers. Scale bar 10 µm.

4.7.2 Lasing in LC droplets

Optical modes for the two outermost cases of bipolar and radial configuration were studied into detail. A 13.7 µm 5CB microdroplet was illuminated by a pulsed laser and the spectrum was measured with the spectrometer. The spectrum of WGMs in the droplet at 4 mM SDS concentration, when the droplet is in radial configuration, is shown in Figure 57a and c. At low pump power, sharp spectral lines, corresponding to TM_l^1 and TM_l^2 WGMs are observed in the spectrum (Figure 57a). When the pump power is increased, some TM_l^1 modes in the wavelength region where the dye has the highest gain, start to lase. In contrast, for bipolar configuration, no modes are observed at low pump energies (Figure 57b). This is probably because the nematic director is not uniform for the path of light around the droplet and the trajectories and modes are therefore not stable and do not have high Q-factors. However, at higher intensity, above the lasing threshold, sharp peaks appear (Figure 57d). Instead of single lines, like in radial droplets, the modes are split and are present as groups of spectral lines. The mode splitting within each group is of the order of 0.5 nm and the width of the lasing lines is 0.05 nm, limited by the spectrometer resolution. The mode splitting can be explained by the droplet not any more spherically symmetric. In spherical radial droplet the modes with different azimuthal mode numbers are degenerate, because of the spherical symmetry. But as soon as the modes in different planes of circulation posses different optical path length, mode splitting occurs (Section 2.2.3). The optical path difference can be caused by geometrical deformation or in our case, since we do not observe any deformation, the difference is caused by non-uniformities of refractive index. In terms of optical path, the bipolar droplet is a prolate ellipsoid and can be therefore also approximated by an ellipsoid with uniform refractive index. The optical path difference can be in this case calculated from the mode splitting using (45). The calculated mode splitting corresponds to the optical path difference of 8% between the two perpendicular planes. This number can be compared to the optical path difference in the case when the director field is completely uniform. We have calculated this in Section 4.3 using (83). For the 5CB droplet the optical path difference for the two perpendicular planes is 5.4%, which is a little bit less than calculated from mode splitting. Just as an observation, the droplet configuration with the two boojums at the surface can not adequately explain such large mode splitting. Namely, in this case the LC molecules have planar alignment on all of the droplet surface, except very near the defects. This introduces just a minute difference in optical paths that go through the defect or away from it. Therefore, this is an additional indication that the bojooms are expelled out of the droplet and the director configuration in the droplet is nearly homogenous.

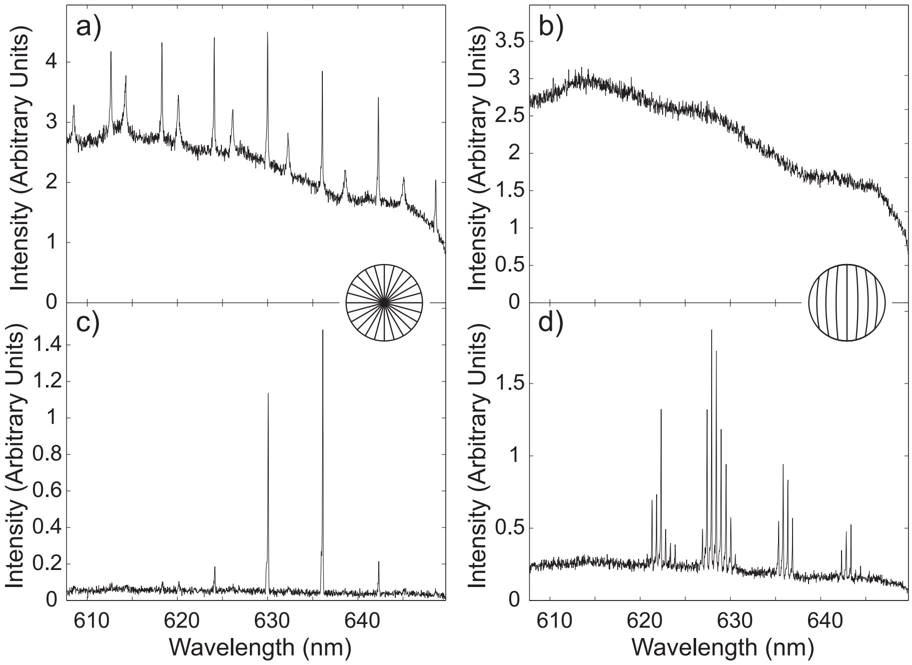

Figure 57: *Fluorescent spectra for radial and bipolar droplets.* Spectra of light emitted from a 13.7 μm 5CB microdroplet were measured when exited by a pulsed laser. a) For radial droplet at low intensity, WGM peaks are clearly visible. b) In contrast, for the bipolar configuration no spectral lines can be observed at low pump power. c) Above the lasing threshold of 0.25 mJ/cm^2 some WGMs start to lase, which is visible as very high peaks compared to the fluorescent background. d) In bipolar droplet also spectral lines appear above lasing threshold of 0.7 mJ/cm^2. Each mode is split in a number of closely spaced lines.

To confirm that the observed spectral features are really lasing, intensity of the spectral lines was measured as the pump energy was increased. The results in Figure 58 show clear thresholds for both radial and bipolar droplets. For a 13.7 μm 5CB microdroplet the threshold for the radial configuration is 0.25 mJ/cm^2 and for bipolar configuration is 0.7 mJ/cm^2. The radial configuration has three times lower threshold as well as more steep slope above the threshold. Above the lasing threshold we can also see that the points are more scattered for bipolar droplet (Figure 58b) than for radial one (Figure 58a), meaning that the lasing is more stable in radial droplets. The insets in Figure 58 show the image of the droplet above the threshold. For radial droplet configuration there are two distinct bright spots that are a typical indication of lasing. However, for bipolar configuration the light intensity is more nonuniform suggesting a little more complicated light paths in the droplet.

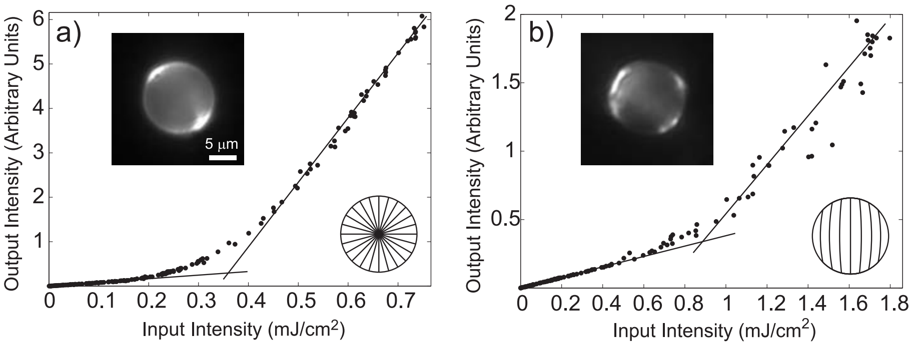

Figure 58: *Lasing intensity for radial and bipolar droplets.* Laser line intensity for a 13.7 µm LC droplet as the pump energy is increased for a) radial configuration and b) bipolar configuration. The lines are just a guide for the eye indicating a clear lasing threshold. The insets show image of the fluorescent light coming from the droplet above the threshold for the two cases.

4.7.3 Sensing characteristics

Fluorescent spectrum from a single trapped droplet was measured as the SDS concentration was gradually increased. In the case of non-radial director configuration, the trapping laser rotated the droplet so, that the rotational symmetry axis was lying in the plane of the microfluidic cell, perpendicular to the direction of the laser beam. Results in Figure 59 show significant changes in the spectrum at different concentrations. For concentrations below 0.1 mM the droplet is in bipolar configuration and the spectra shows typical groups of lasing lines separated by 0.5 nm. As the SDS concentration is increased to 0.1 mM, when the defect ring appears, the spectrum begins to change. There are still groups of lines present, but at slightly different positions. When the concentration is increased beyond 0.3 mM the split modes join into a single spectral line and shift strongly. The spectrum is then changing quite chaotically with spectral lines appearing and disappearing and changing postings quite randomly. At 0.5 mM when the defect ring closes into a point defect, single strong spectral lines appear and do not shift considerably all the way the droplet changes to radial configuration at high SDS concentrations. For bipolar and radial droplets we have proven lasing by measuring the threshold characteristics, but for intermediate droplet configurations, the spectral lines may not always be lasing. For the concentration range between 0.3 mM and 0.4 mM where the "chaotic" change in the spectral features occurs, a more detailed measurement was performed on a 16 µm droplet by changing the concentration in 0.02 mM steps (Figure 59c). The spectral lines are clearly visible, but they are quite wide. As the concentration is increased the lines change position and width in a non-monotonic and unpredictable way. Also if the experiment is repeated multiple times on the same droplet, the spectrum is changing in slightly different ways in each experiment.

At this point, it is not possible to precisely measure the concentration of SDS using the spectral features. Even though the spectrum is sensitive to small variations in the concentration, it just not changes in a predictable way nor following monotonically the concentration. We can however, see from the spectrum if the SDS concentration is below 0.2 mM or above 0.5 mM. So the sensor can not in this way measure the concentration, but it can be used as an indicator of the presence of a targeted molecule. The concentration sensitivity of such a sensor can be dramatically reduced by using different target molecules. It has been recently demonstrated for endotoxins [67], that already a million times smaller concentrations than for SDS, can induce the change from bipolar to the radial configuration.

The changes induced by different surfactant concentrations are reversible, since the sur-

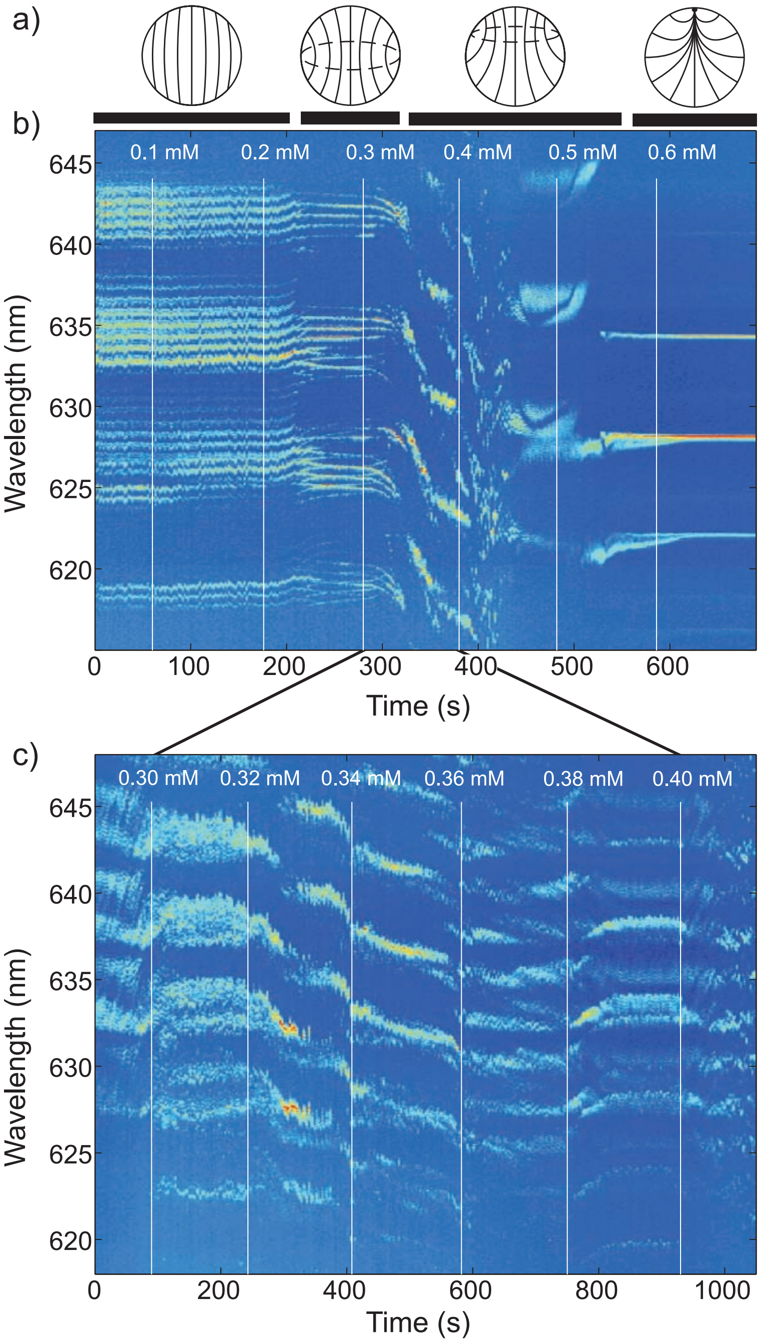

Figure 59: *Lasing spectrum as the concentration is increased.* a) The director configurations for different concentrations corresponding to b) spectrum of fluorescent emitted from a 13 µm 5CB droplet as the concentration of SDS was gradually increased. c) The range from 0.3 to 0.4 mM where chaotic changes in the spectrum occur, was measured more into detail on a 16 µm droplet with concentration steps of 0.02 mM.

factant molecules on the interface are in thermodynamic equilibrium with the surrounding water solution [101] and can therefore adsorb and desorb from the surface. Droplets can be multiple times transformed from bipolar to radial and vice versa by changing the contraction of SDS, which can also be seen in the lasing spectrum (Figure 60). The equilibrium states, the bipolar and radial configuration have well defined spectrum. However, within the transition between these two states, the spectrum does not change in the same way in one or the other direction. What is more, as already explained before, even one way transition on the same droplet is different every time.

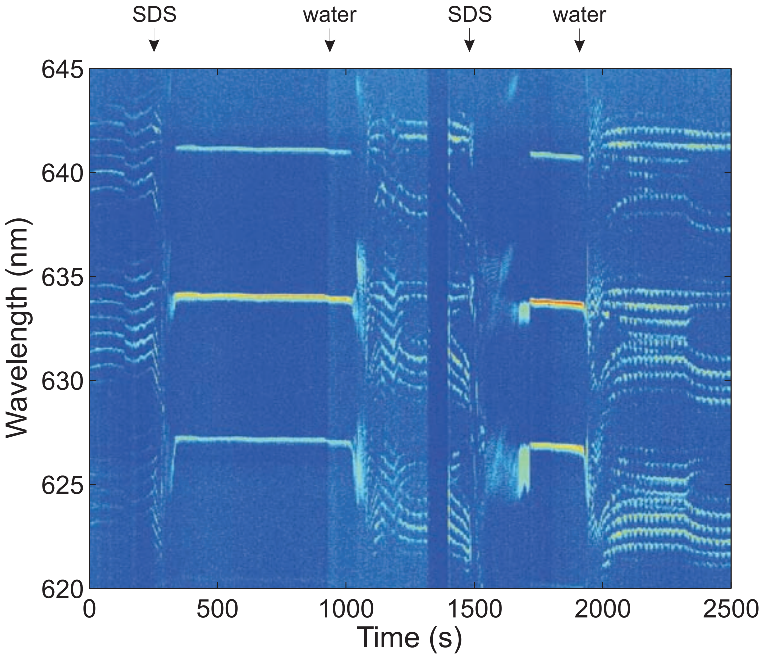

Figure 60: *Lasing spectrum as water and SDS ar added.* Lasing spectrum from a single trapped droplet when pure water and 4 mM SDS are alternately added to the microfluidic chip.

4.7.4 Sensing in non-lasing regime

The droplets can also be excited with a CW laser, so in the regime below lasing threshold. In this case, below 0.5 mM, similar as in a bipolar droplet, there are no WGM lines in the spectrum. Above this concentration, when the droplet is in radial configuration, WGMs appear. So, the sensor is working as a indicator of the presence of surfactant molecules. In Figure 61 spectrum as a function of time is shown when the droplet is first in 4 mM SDS solution and then pure water is added. The spectral lines at first start to shift, and soon disappear. From this kind of graph we can conclude if the surfactant is present or not.

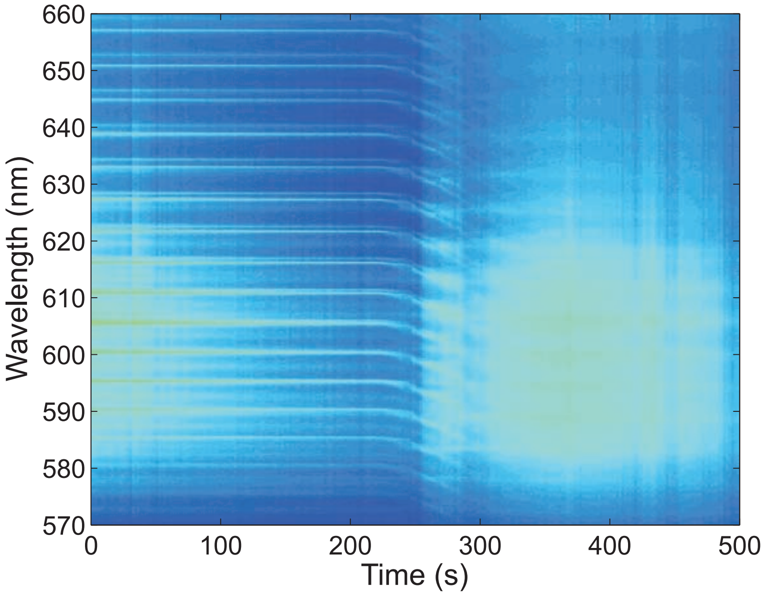

Figure 61: *Fluorescent spectrum in a non-lasing regime.* Spectrum of fluorescent light from a single trapped droplet excited with the CW Argon laser. At first the droplet is in 4 mM SDS. At 250 s pure water is added.

4.8 3D laser

4.8.1 Cholesteric liquid-crystal droplets

First, we have tried to make a dispersion of CLC droplets and to reproduce the results already published years ago [45, 102]. We have prepared a mixture of a nematic liquid crystal and a chiral dopant so, that the pitch of 2 µm was achieved. This pitch does not produce a photonic bandgap in visible light, but the periodic structure can be see under optical microscope. To have high the contrast of the cholesteric layers on the images, a high birefringence material was used. By mechanical mixing, spherical polydispersed droplets are readily formed. Periodic concentric rings of alternating light-dark colors are observed in the droplets (Figure 62a and b). The stripes are observed because of modulation of the refractive index, their periodicity corresponding to half the pitch. The cholesteric helix is pointing from the center of the droplet in all directions outwards to the surface as it is schematically shown in Figure 63.

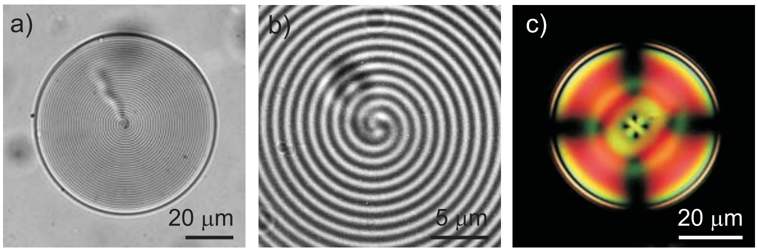

Figure 62: *CLC droplets micrographs.* a) A CLC droplet with the pitch of $p = 2.2\,\mu\text{m}$ in glycerol. The perfect structure with nearly concentric shells is clearly visible. From the center to the surface there is a defect line, that is out of focus. b) A magnification of the central part of a droplet when viewing along the defect line. c) A short pitch CLC droplet viewed in crossed polarizer.

The degenerate planar anchoring on the surface promotes this configuration. At the center it should be a defect, where the orientation of the director is not defined. Because of topological reasons the director configuration cannot be uniform across the whole droplet, but a defect line should be formed. From literature [45,102] we know that director configuration should be of a spherulite-type with a radial defect, which is a $s = 2$ disclination line going from the center of the droplet to the surface. This kind of structure was observed before in the experiments [103–105]. The second configuration that can be found in cholesteric droplets and has been observed in experiments [103,106], is also of spherulite-type, but with a $s = 1$ diametrical defect structure, where the defect line runs diametrally from one surface through the center to the other surface. In all our experiments with CLC droplets we have observed only radial defect structure [2]. Nearly all of the droplets smaller than approximately 100 µm have this perfect spherulite structure, without any additional defects or imperfections. Most larger droplets have additional defects or they are deformed or in contact with the surface because of their large size. Heating into isotropic phase and back to cholesteric phase does not help to get read of unwanted defects in large droplets. What is more, the heating and annealing introduces a lot of additional defects into the droplets. Therefore, it is optimal to prepare the dispersion of the droplets at temperature where cholesteric phase exists.

---

[2] In some preliminary experiments with ferroelectric liquid crystal (SmC*) droplets having homeotropic anchoring on the surface, we have observed mainly diametrical defect structure.

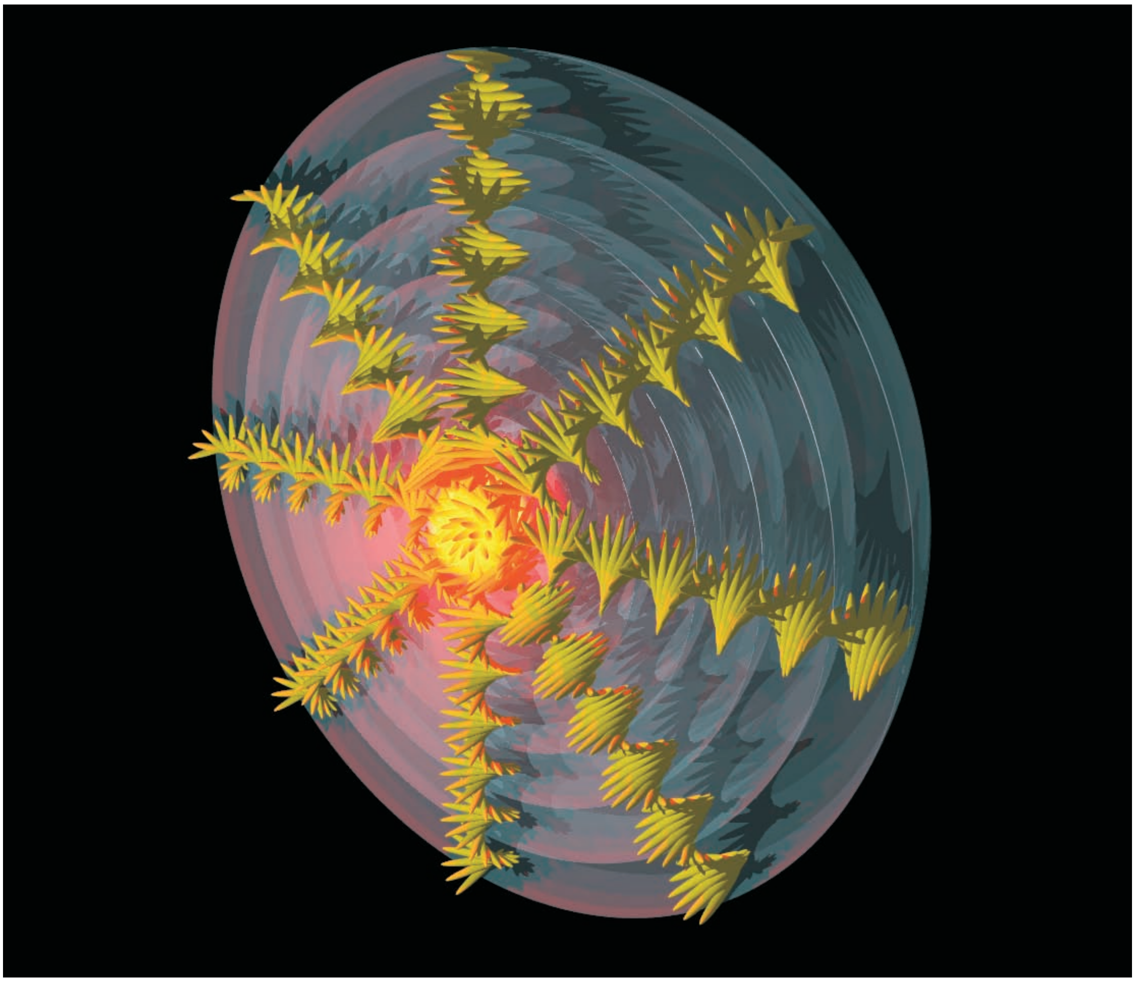

Figure 63: *An artist's impression of a 3D CLC laser.* The yellow rods represent LC molecules that form a helix from the center of the droplet outwards. The helix is seen as a concentric shells that act as a spherical Bragg mirror. When the droplet is excited by an external laser, it emits light from its center.

4.8.2 Simulation of the CLC droplet configuration

To better understand the structure inside the CLC droplet, numerical modeling was performed by David Seč and Tine Porenta [107] from Prof. Slobodan Žumer's soft matter theoretical group, Faculty of mathematics and physics, University of Ljubljana. To model the droplets, a continuum, single elastic constant Landau-de Gennes approach based on the nematic order parameter tensor Q_{ij} was used. The model takes into account the Frank elasticity due to deformation of the liquid crystal, as well as the local variations of the scalar order parameter. The minimal free energy configurations of the director field and the scalar order parameter were obtained by solving a system of coupled partial differential equations with appropriate boundary conditions using an explicit Euler finite difference relaxation algorithm on a cubic mesh. At the droplet surface strong degenerate planar anchoring conditions were taken into account. The diameter of the droplet in the simulations was 4.5 µm and the pitch was 0.75 µm, so that the ratio between the droplet diameter and the pitch was a factor of 6. The results are presented in Figure 64. We can see a defect structure that extends from the center of the droplet to its surface. On the surface there are two point defects that are close together and can not be really distinguished in the experimental pictures as two separate defects.

To compare the experimental micrographs of the long pitch droplets (Figure 62a and b) with the simulations of the director field, David Seč also simulated the appearance of the

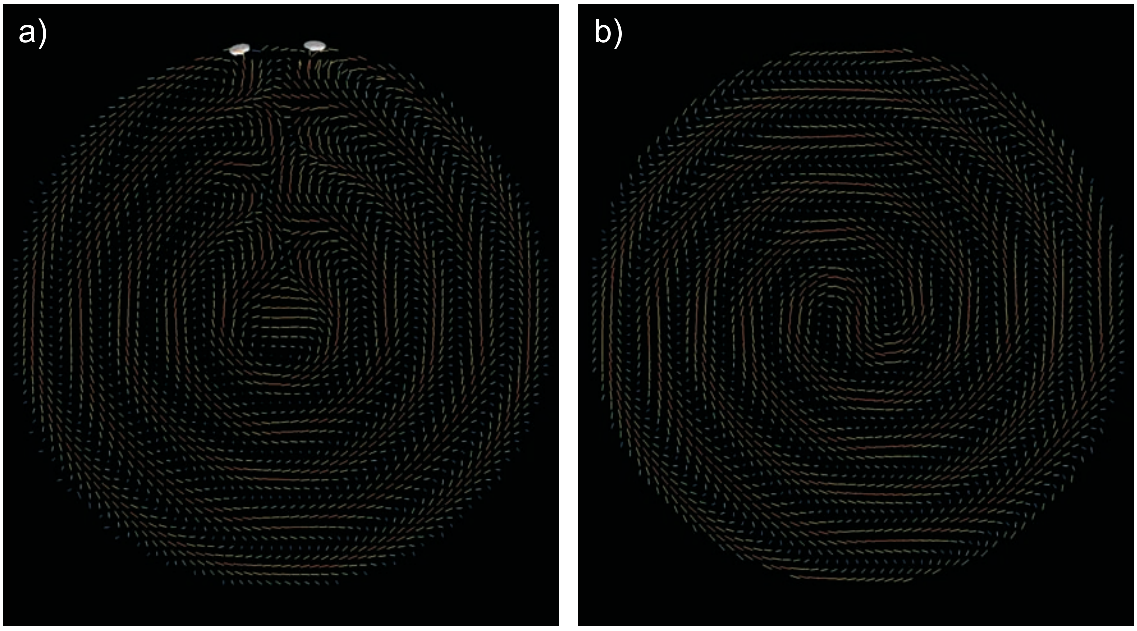

Figure 64: *CLC droplet director configuration simulation.* Director configuration in a 4.5 µm diameter droplet for two perpendicular planes a) y-z and b) x-y. The pitch length is 0.75 µm. The director orientation in the plane of the image is represented by the orientation of the lines. The orientation out of the plane is presented as different colors and line lengths. a) A complex defect structure extending from the droplet to the surface is clearly visible. At the surface there are two point defects represented by white points.

droplets under crossed polarizers [107]. The previously calculated director field configuration in the droplets was upscaled to a larger diameter so that the pitch was 4.5 µm. The refractive indices were $n_o = 1.5$ and $n_e = 1.7$. The transmission of white light through the structure of the droplet was calculated using Jones 2×2 matrix formalism, where just the birefringence because of the director orientation was taken into account. In this case, refraction and reflection were not taken into account, just the phase difference between the ordinary and extraordinary ray due to the director orientation. As a white light, ten wavelengths from the spectrum of an approximate black body radiation were taken. Transmission for each wavelength was calculated separately and the final picture (Figure 65a and b) is their sum. The experimental results (Figure 65c and d) match the calculations. The colors are not the same, since the pitch, droplet size and refractive indices are not the same in the experiments compared to theory. The illumination in the experiments is also not completely parallel and the light is captured by a high numerical aperture objective. The colors of the layers also change when changing the focus of the microscope.

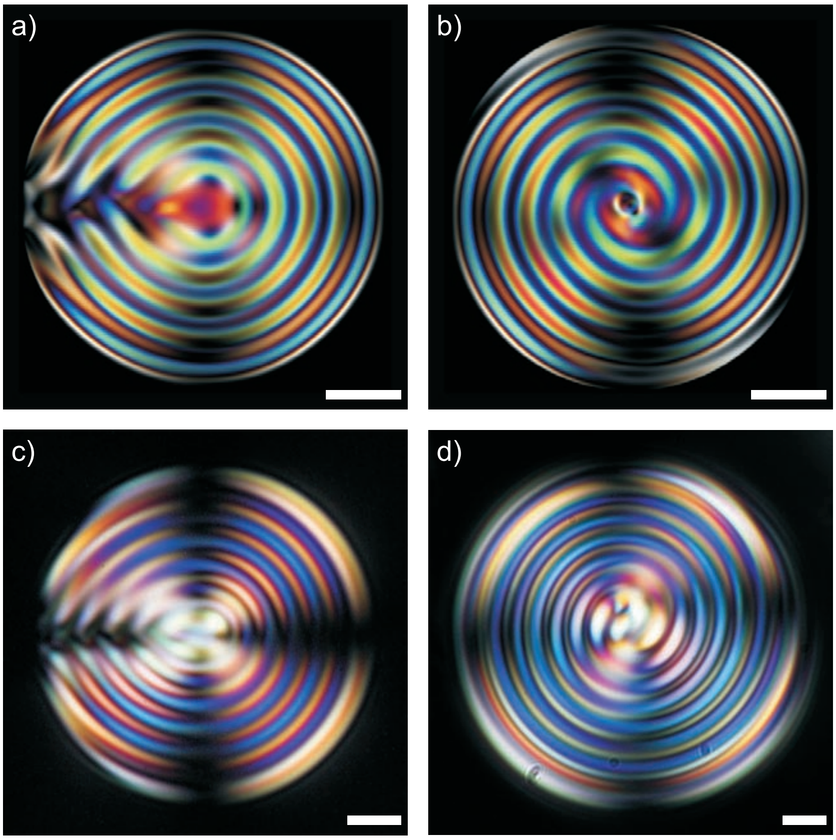

Figure 65: *Transmission through a CLC droplet: simulation and experiment.* Calculation of the transmission of white light through a cholesteric droplet for two directions a) perpendicular to the line defect and b) along the defect. The pitch is 4.5 µm. c) and d) experimental images of two cholesteric droplets under crossed polarizers for the same light propagation direction as for calculated transmission. The pitch is 4.3 µm. Scale bar in all the images is 5 µm.

4.8.3 Lasing characterization

When we were able to make droplets with nice internal structure, we have used higher chiral dopant concentration, to reduce the pitch, so that the reflection bandgap was in visible light. Such a droplet is shown in Figure 62c in crossed polarizers. Fluorescent dye was added as well. The droplets were also nice up to 100 µm and the radial defect was still visible. A single droplet was observed through a 20x objective and illuminated with the 532 nm green Q-switched laser with repetition rate of 200 Hz and a waist diameter on the sample of $\sim$ 100 µm.

At low excitation laser power, the whole droplet is emitting fluorescent light (Figure 66a). When increasing the power of the pump laser, a bright spot suddenly appears in the center of the droplet (Figure 66b and c). The intensity of the emitted light is slightly fluctuating and speckles are observed, suggesting coherent light emission. When further increasing the input laser the light intensity from the center of the droplet becomes really strong and a bright spot on the sample can be seen even with naked eye.

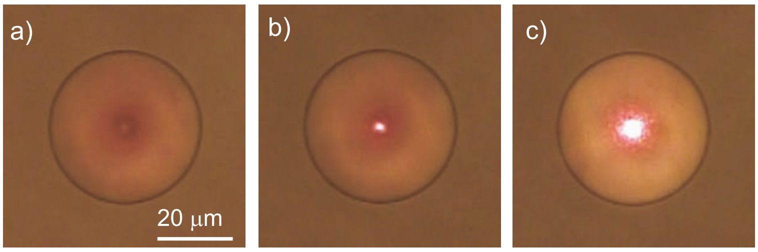

Figure 66: *Emission of light from a 3D laser when the intensity of the pump laser is gradually increased.* a) Below the lasing threshold at 1.6 mJ/cm^2 only some fluorescence is observed in the droplet. b) Just above the threshold (1.9 mJ/cm^2), a bright spot is observed in the center of the droplet corresponding to omnidirectional lasing. c) At high pump power (12 mJ/cm^2) the lasing becomes very intense.

Next, the light from the droplet was analyzed as a function of the pump intensity by using the spectrometer (Figure 67a). At lower intensity, when no bright spot is present in the center of the droplet, just typical fluorescent background in red light is observed. But at higher intensities a single sharp spectral line positioned at around 600 nm appears in the spectrum indicating threshold behavior. Indeed, when spectral line intensity is measured as a function of pump intensity, typical lasing threshold behavior is observed (Figure 67b) with a threshold of 1.7 mJ/cm^2, equivalent to the pulse energy of 20 nJ for a 1 ns pumping pulse, focused to uniformly illuminate a 40 µm diameter droplet. As a comparison, the threshold for planar cell filled with the same mixture with 40 µm thickness was 1.3 mJ/cm^2. The threshold is dependent upon the size of the droplet and increases with small diameter droplets (Figure 67c). The reflectivity for the light trapped in the center decreases with smaller number of layers and therefore increasing the threshold. The smallest droplets made of high-birefringence cholesteric liquid crystal that were still lasing were 15 µm in diameter. Nearly all the droplets larger than this diameter were lasing when illuminated with high enough intensity. Also the droplets that did not posses perfect internal structure, but contained defects, were also lasing but usually the lasing was multimode with multiple spectral lines and non-point-like emission intensity. We have achieved a maximum average power of a CLC Bragg laser of 0.05 mW at a 200 Hz repetition rate. The maximum power is limited by photobleaching of the dye as well as thermal heating and optical force of the pump laser, that pushes the droplet to the cover glass. At lower powers the lasing at 200 Hz repetition rate can be maintained for more than 10 minutes. The lasing time is dependent on photobleaching of the dye, that in contrast to lasing in planar CLC cell, can not be replaced by diffusion from other parts of the cell, since single droplets are isolated systems.

The laser line spectral width is typically $\sim$ 0.1 nm (Figure 67d). This is comparable

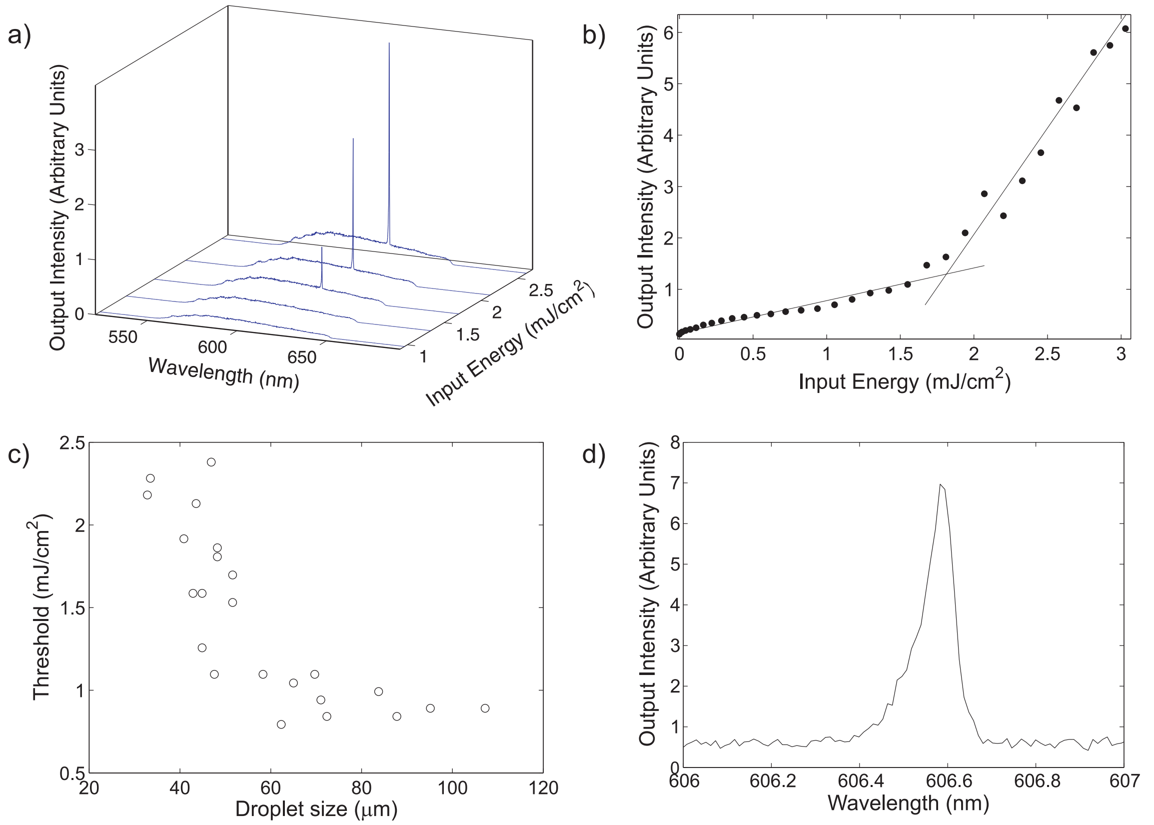

Figure 67: *Optical properties of a spherical CLC laser.* a) Spectra of light from a single CLC droplet when the pump power is increased. b) The intensity of the laser line as the pump intensity is increased. A clear laser threshold can be observed at $\sim 1.8\,\mathrm{mJ/cm^2}$. c) The laser threshold as a function of droplet diameter. d) High resolution spectra of the laser line shows spectral width of 0.1 nm.

to lasing in planar CLC [55] and lasing in blue phase II [5]. However, if the acquisition time of the spectrometer is below 50 ms, the laser line width is below the resolution of the spectrometer (0.05 nm) and the laser line fluctuates in time (Figure 68). This is probably due to the thermal fluctuations of the liquid crystal director as well as the distortions and heating induced by the pump laser. The characteristic flickering of the laser light from the center of the droplet can also be observed by the naked eye.

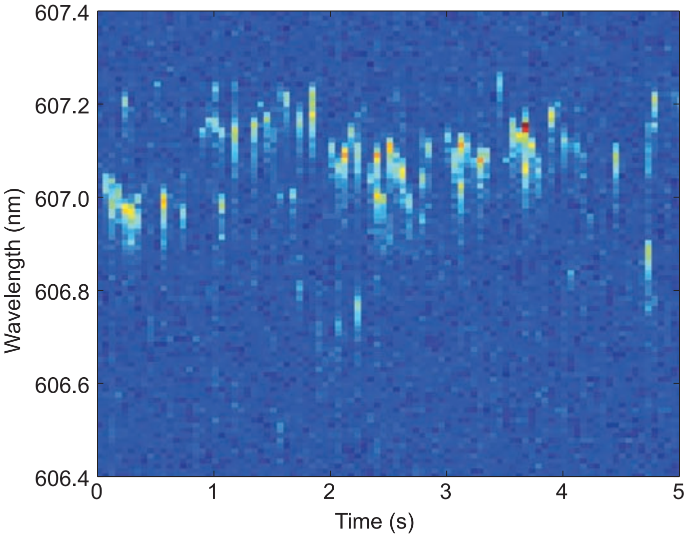

Figure 68: *Temporal spectral properties of a spherical CLC laser.* High speed spectral acquisition of lasing from a 34 µm droplet. The acquisition time is 50 ms. Fluctuation of the laser line position as well as the intensity are clearly visible. The time averaged linewidth is 0.18 nm.

We have also measured if the laser wavelength and linewidth are dependent on the size of the droplets. In the case of lasing wavelength there is a slight trend of increasing wavelength with larger size (Figure 69a). This can simply be due to heating of the droplets with the pump laser, since for smaller droplets more power is needed because of higher threshold. At higher temperature the laser line should be shifted to shorter wavelengths which is in agreement with the results. In general the difference between droplets with different size is just 5 nm. Since with our procedure we can not make monodisperse droplets, it is important that the lasing is not size dependent. Linewidth is also size dependent, with larger droplets having narrower lasing line (Figure 69b). This can be explained in two ways. Firstly, as already explained, smaller droplets need more power to start lasing, so the heating introduces more thermal flotations which time averaged, broaden the laser line. Secondly, smaller droplets have fewer layers, which can reduce the Q-factor of the resonator and make the laser line wider.

The lasing in planar CLC cell can be either photonic bandedge lasing or defect mode lasing [55]. In the first case, the laser line appears either on the short or at the long edge of the photonic bandgap, depending where the dye has the optimal gain. The defect lasing is present when a few hundred nanometers thick layer of usually isotropic material is placed inside the CLC active material [3]. In this case, the lasing occurs in the middle of the photonic bandgap. For the CLC microdroplet it could be the case of the defect mode lasing, since in the center of the droplet there is a LC structure, that is comparable to the wavelength of the light (Figure 64a, 65a and c). The alternating layers of low-high refractive index confine the light to the center of the droplet where the optical defect is located. However,

---

[3] We have to distinguish between *optical defects* and *defects in LCs*. An optical defect is a structure with size comparable to the wavelength of light that is embedded in a photonic structure and supports optical modes. Whereas, a defect in a LC is an isotropic region, typically few nanometers in size. It is too small to act as an optical defect, so is not able to support optical modes.

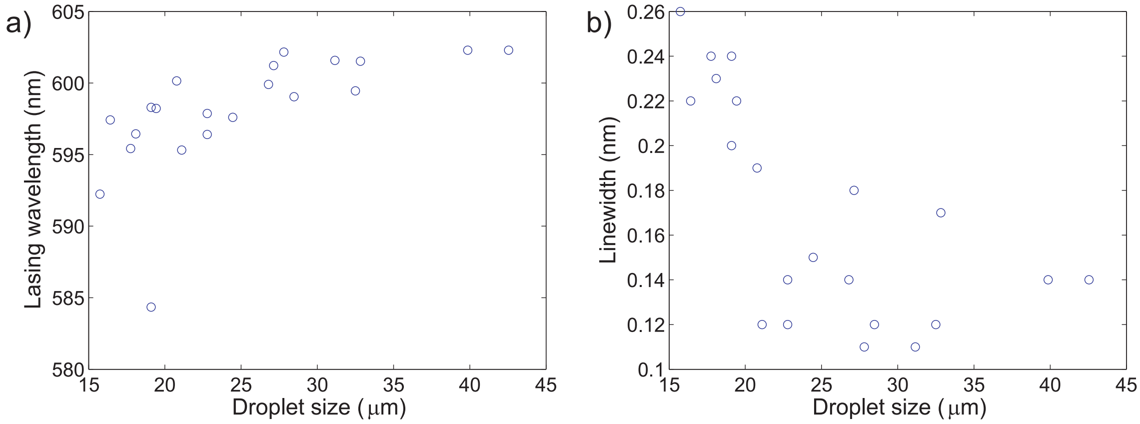

Figure 69: *Lasing properties as a function of droplet diameters.* a) Lasing wavelengths and b) lasing linewidths of droplets with different diameters. Both measurers were performed using high refractive index LC.

when viewing the droplet from other direction, there is no such structure present, but just holesteric layers that end in the center of the droplet (Figure 64b, 65b and d).

To find out which type of lasing is occurring in the droplets, the position of the reflection bandgap should be compared to the lasing line. The reflection bandgap of the same material as used to make the droplets, was measured in a planar cell. The central position of the reflection bandgap is 595 nm, equivalent to the pitch of 400 nm. The lasing occurs at the longer bandedge (Figure 70) and is therefore a bandedge lasing. This is true for all the directions of lasing, as we will see in Section 4.8.5. The lasing mechanism for our CLC microdroplets is therefore the same as in planar CLC lasers that do not contain a defect. In that case the lasing occurs in the direction of the helical axis. In the droplet, the helix is pointing in all the directions from the center and also lasing is than occurring in all the directions corresponding to many independent lasers emitting light in different directions.

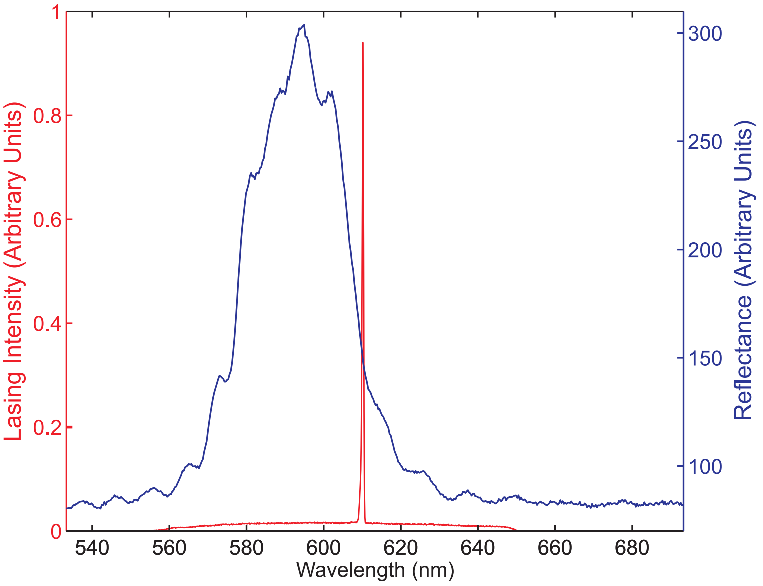

Figure 70: *Lasing and reflection spectrum.* Laser spectrum above the threshold (red) compared to the reflection spectrum (blue) of white light on planar cell 30 μm in thickness filled with the same CLC material.

4.8.4 Polarization

Polarization of the laser light emitted by 3D Bragg laser is an important parameter that should be measured. For planar CLC lasers the polarization is circular, so also for spherical CLC lasers circular polarization is expected. First, the lasing intensity from a single droplet was measured as the polarizer was rotated. The intensity was extracted from the spectra separately just for the laser line and just for the fluorescent background (spontaneous emission). In Figure 71a a small modulation of light can be seen, so the fluorescent background light is slightly linearly polarized. This can be explained by a slight ellipticity of the excitation light, that is generated when the circularly polarized excitation light is reflected by the dichroic mirror. Since the excitation light is slightly linearly polarized, so is also the emitted light. The laser line of the 3D laser is not linearly polarized, as can be seen from Figure 71c. For measurement of circular polarization a quarter-wave plate was added before the polarizer with its axis at 45°. The fluorescent background is slightly circularly polarized (Figure 71b), which can be explained by suppression of the spontaneous emission of just one circular polarization caused by the PBG. For the laser line, a large amplitude modulation can be observed (Figure 71d), therefore it is highly circularly polarized. However, we have to emphasize that the results for different droplets varied greatly and we can not say for certain that the output of the 3D lasers is really circularly polarized. We have also not measured in detail the polarization of the light emitted along the defect line. In all the experiments the defect line was oriented randomly.

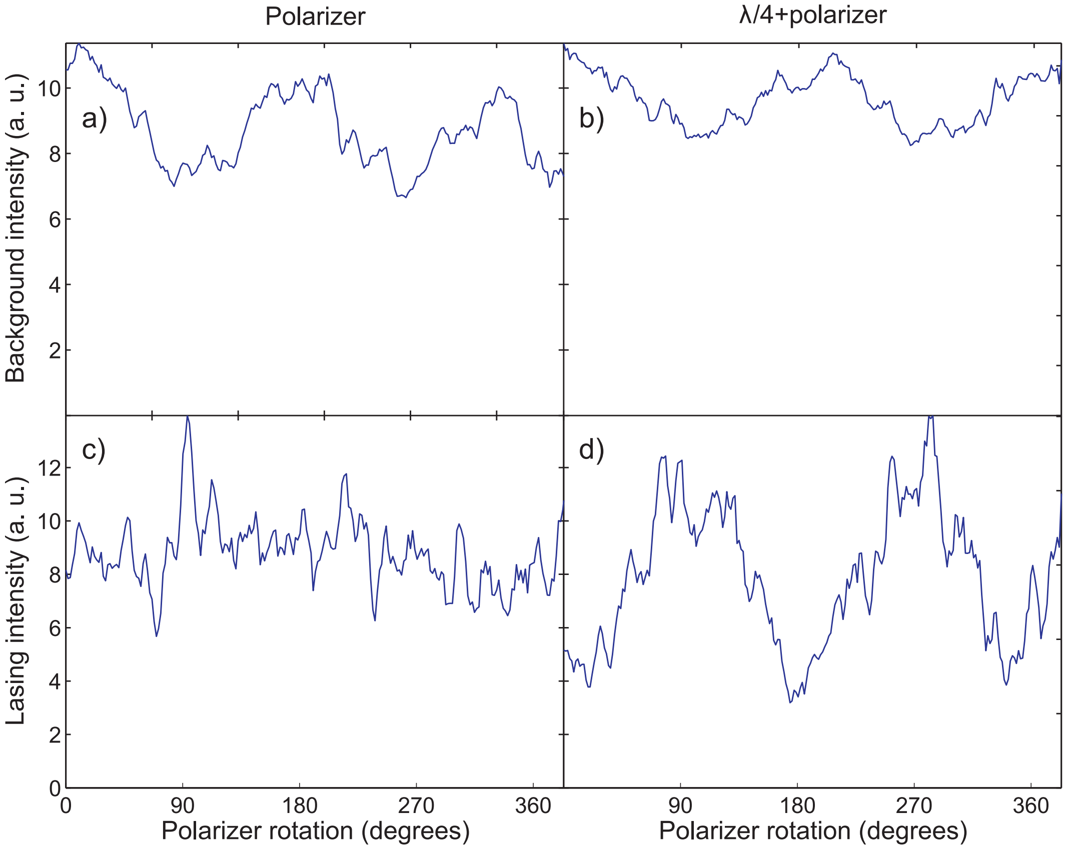

Figure 71: *Polarization measurements of the 3D laser.* Intensity of the fluorescent background (top row) and intensity of the laser line (bottom row) as the polarizer is rotated (left column) and with an additional quarter-wave plate added (right column).

4.8.5 Angle dependance

Since the laser cavity in the CLC droplet is almost spherically symmetric, we expect the laser to emit light in all the directions equally. In most applications the highly directional emission is needed, but in some special cases, such as holography, sensing or imaging, a point source of coherent light that emits light in all directions is a better choice or even necessary. Therefore, the directionality of the emission was measured. The results in Figure 72a show that the lasing intensity is indeed highly directionally uniform. The wavelength is also nearly constant across the entire solid angle (Figure 72b). We have to emphasize that the angle measurements are time averaged, which means that for each point on the graphs, many laser pulses were measured. It could be possible that each individual pulse could have a random specific direction of lasing, but when many of them are averaged, uniform lasing in all directions is achieved. To find out if the laser is emitting in all the directions simultaneously, intensity of the emitted light should be measured at high speed from at least two different angles and correlation should be calculated.

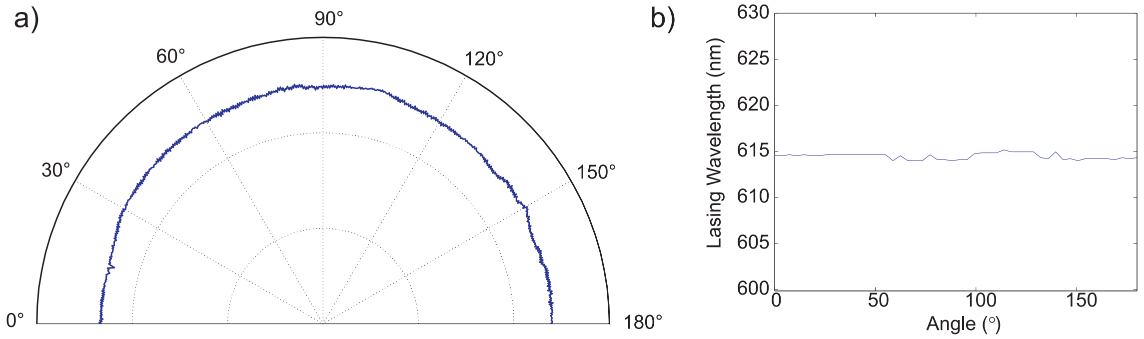

Figure 72: *Angle dependance of lasing.* a) Time averaged lasing intensity from a single 50 μm CLC droplet when the camera was rotated around the capillary. The results show very uniform angle dependance. b) Lasing wavelength as a function of angle is also very uniform.

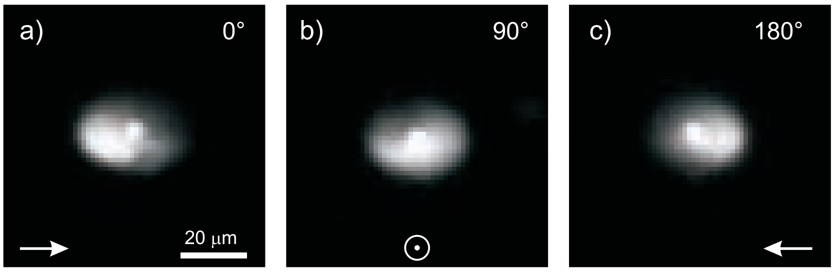

Figure 73: *A micrograph of a CLC laser from different view directions.* Images of a single 3D laser in a capillary excited above the threshold from three different perspectives. A bright spot in the center corresponds to lasing and it is visible from all the directions. The droplet is of a elongated shape because of the optical distortion when observing through a curved surface of the capillary. The arrows show the direction of the excitation laser.

4.8.6 Tunability

By selecting the appropriate dye and chiral dopant concentration, lasing in planar cells has been achieved by other groups in a wide range of wavelengths from UV to IR [41, 108] and should also be possible in CLC droplets. The cholesteric pitch is known to be temperature dependent [42], either elongating or shortening with temperature, depending on the LC and the chiral dopant used. The change in pitch also changes the position in the photonic bandgap and therefore the lasing wavelength. In the case of CLC droplets we were able to tune the lasing wavelength by almost 50 nm when increasing the temperature by just

15°C (Figure 74a). The spectral shift is almost linear with temperature (Figure 74b), the tuning coefficient being 3.5 nm/K and completely reversible. Phototunability has also been demonstrated in cholesteric lasers [109] and should be interesting for application in phototunable spherical lasers.

Furthermore, by applying electric field, the lasing characteristics should also be changed. In the case of positive dielectric anisotropy of the CLC, the electric field should unwind the helix [88], thus changing the directionality and wavelength of lasing. At even higher fields we expect that the lasing will cease, because of the helix would be too much deformed. More interesting could be using a negative dielectric anisotropy LC. In this case the electric field should induce planar CLC structure [110] such as in planar cells, making the laser unidirectional. Some experiments with electric field have been already done, however with liquid matrix such as glycerol the problem is that the field deforms the droplets and pushes them to one surface. Therefore, a solid carrying medium with planar anchoring has to be used. No appropriate material has been found till now.

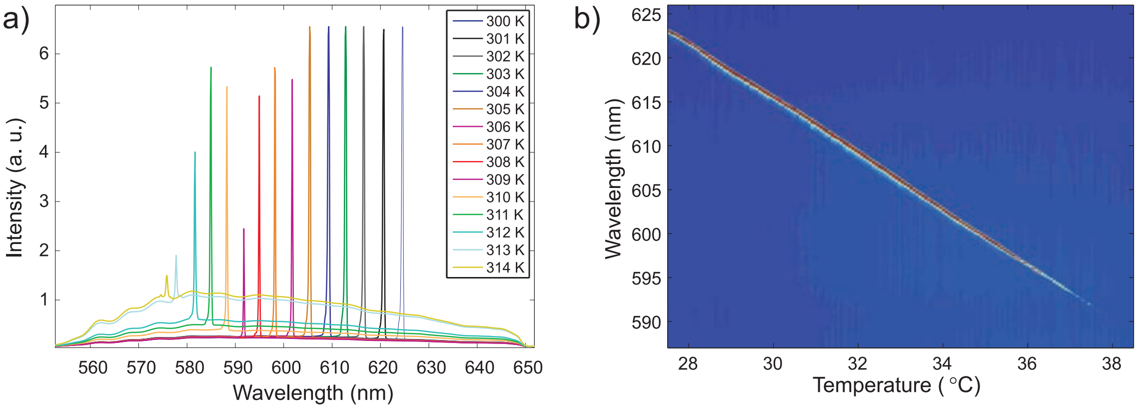

Figure 74: *Temperature tunability.* a) Lasing spectra from a single droplet when the temperature was increased. At temperatures higher than 310 K the bandgap was not in the optimal range of the fluorescent dye and the lasing ceased. Therefore, the excitation power had to be increased, also increasing the fluorescent background. b) Continuous temperature change shows almost linear dependence.

4.8.7 Lasing of higher Bragg modes

Till now we were focusing only on completely radial lasing in cholesteric droplets, having a single sharp spectral line and the light coming from the center of the droplet. In cholesteric droplets we can also achieve lasing of higher Bragg modes that also have angular momentum. By using lower concentration of chiral dopant the PBG can be pushed to infrared part of the spectrum, so that it is out of the gain region of the dye and the droplet does not lase any more. This is true just for light with the incidence along the helical axis. Following the Bragg's law, at smaller angles, light with shorter wavelengths is reflected from the periodic structure. In the droplet this means, that the red fluorescent light from the dye is not any more reflected in radial direction, but instead reflects multiple times from the layers at a smaller angle and so circulates in the droplet. This is similar to WGMs, where the light is multiply reflected from the surface and circulates around the droplet. The difference in cholesteric droplet is, that the light is not reflected because of total internal reflection, but because of Bragg structure. The light also does not circulate close to the surface, but in the interior of the droplet. In Figure 75 lasing spectra and images of three droplets with increasing pitch length are shown. When a droplet is pumped by a pulsed laser, a ring of light is clearly visible in the interior of the droplet. As the pitch length becomes longer, the ring of light becomes larger. Also at longer pitch, the droplet needs to be larger, in order to support these modes. In the spectrum there are multiple modes visible and as we go to longer pitch the number of lasing modes increases. Overall, these are still preliminary results and we do not know exactly which modes are lasing, what is the mode spacing and what is the radius of the light circulation dependent on.

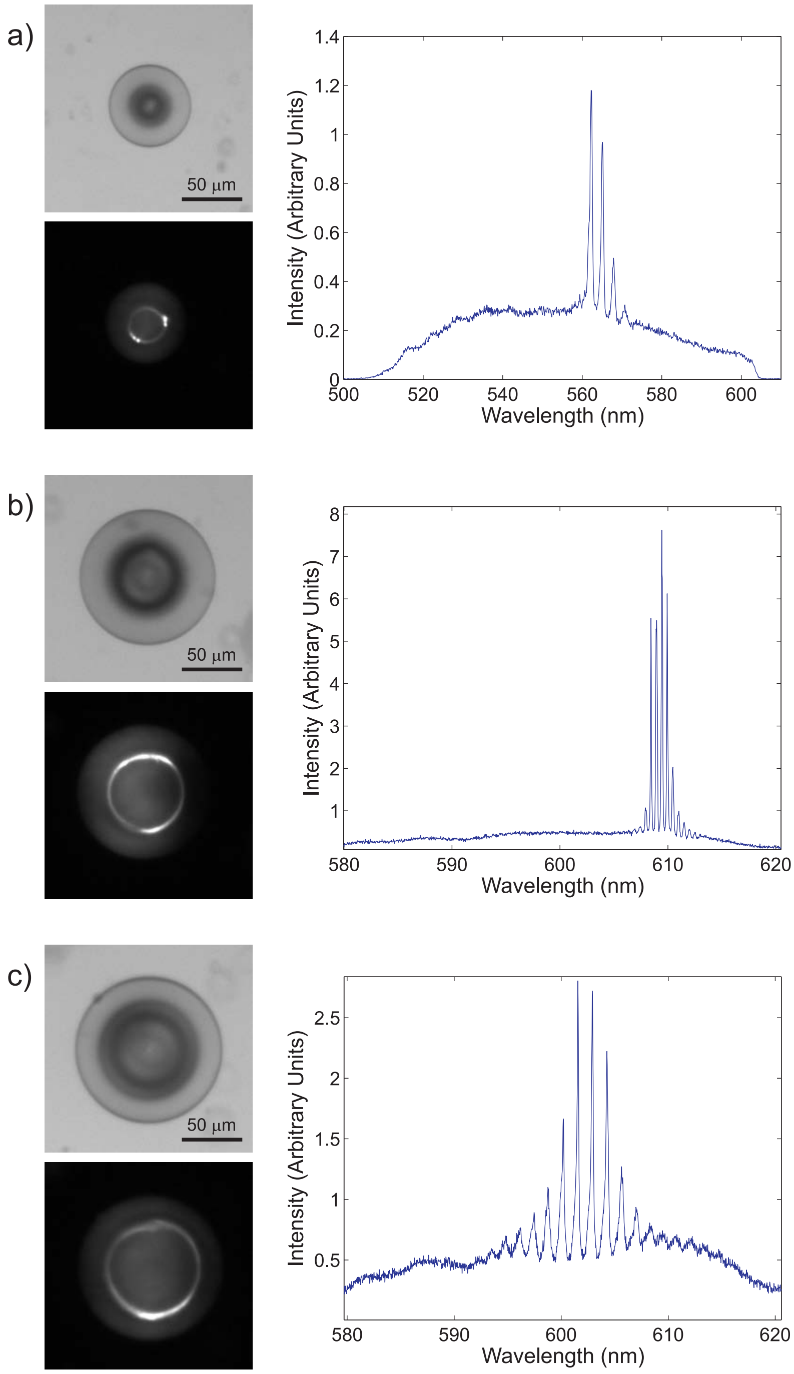

Figure 75: *Lasing of higher Bragg modes in longer pitch droplets.* Images of three cholesteric droplets with different pitch in white light, under excitation and their lasing spectrum. a) Droplet with pitch of 470 nm, corresponding to central position of the PBG of 700 nm. b) Droplet with pitch of 510 nm, corresponding to the PBG at 770 nm and c) Droplet with pitch of 550 nm, corresponding to the PBG at 830 nm.

In most experiments we have used low refractive index LC and high refractive index of the outside medium, so that the index contrast is as low as possible in order to suppress WGMs on the surface of the droplet. By using a high refractive index LC (MLC-2132) also WGMs can start to lase at the same time as the Bragg lasing (Figure 76a). The WGMs

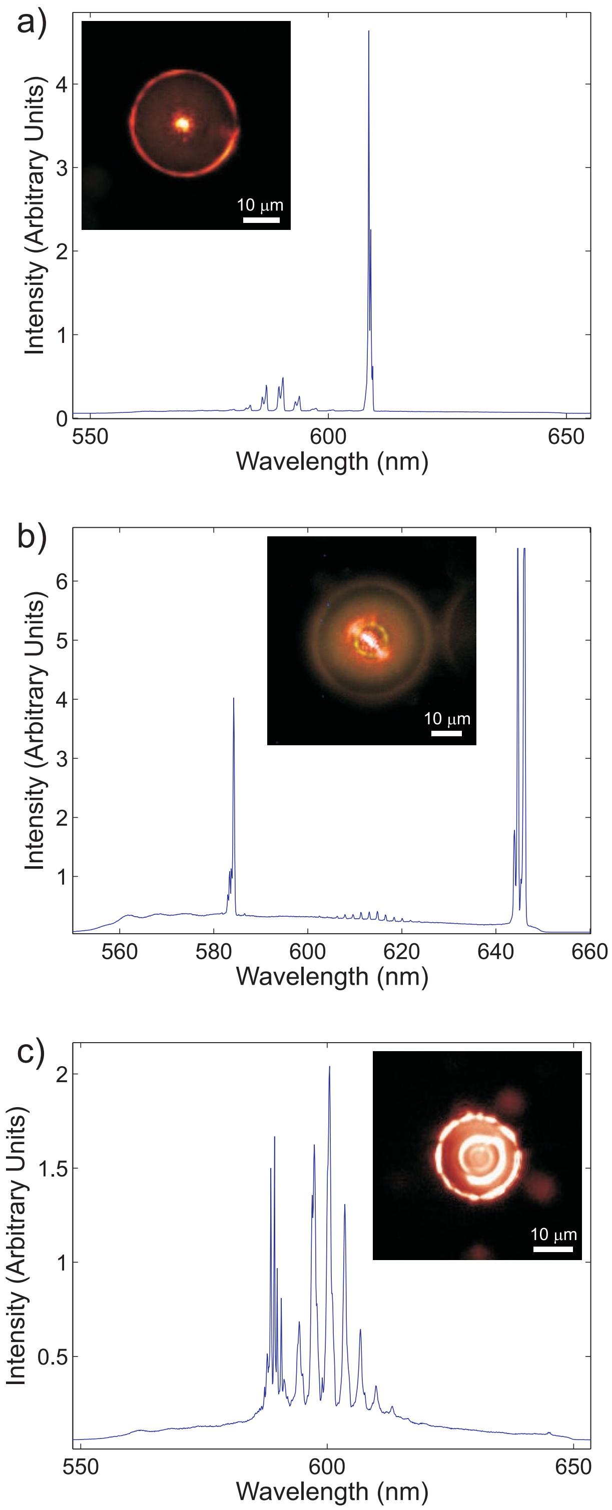

Figure 76: *Lasing of higher Bragg modes and WGM lasing in longer pitch droplets.* Lasing from droplets made of high refractive index cholesteric droplets with different pitch length. a) At short pitch we observe radial mode Bragg lasing and WGM lasing, as a bright spot in the center of the droplet and a ring on the surface, respectively (chiral dopant concentration is 26%). b) Both radial mode lasing and lasing of higher Bragg modes are observed as well as WGM lasing, as a bright spot in the center of the droplet, a ring in the interior of the droplet and a ring on the surface, respectively. (chiral dopant concentration is 24%) c) At even longer pitch just lasing of higher Bragg modes and WGM lasing is observed, a ring in the interior of the droplet and a ring on the surface, respectively. (chiral dopant concentration is 20%)

are visible as an ring on the surface of the droplet and the Bragg lasing is coming from the center of the droplet. In the spectrum several peaks at shorter wavelength correspond to WGMs and a single peak at 610 nm corresponds to Bragg lasing. When we increase the pitch length, lasing of higher Bragg modes appear as a ring visible in the droplet (Figure 76b). WGMs are visible as well. At even longer pitch the radial Bragg mode is not lasing any more. Lasing of higher Bragg modes is visible as a set of closely spaced spectral lines at shorter wavelengths and WGMs are visible as peaks at longer wavelengths (Figure 76c).

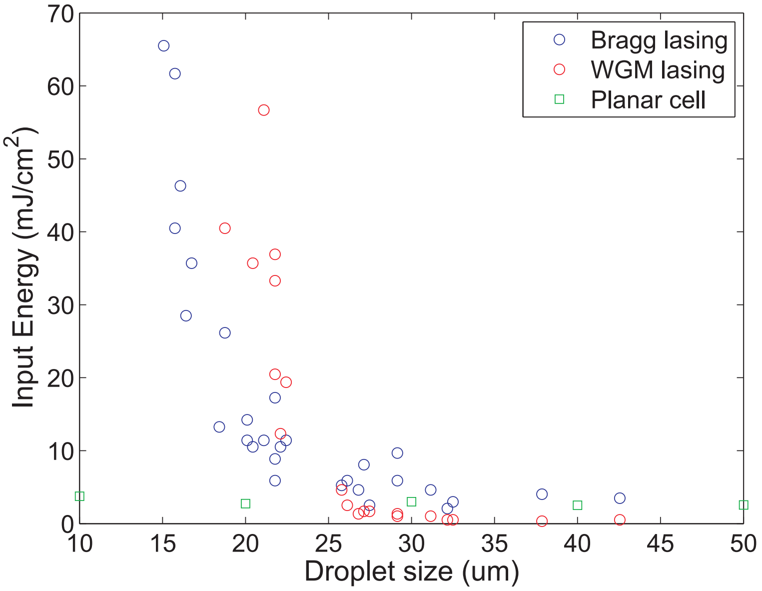

Figure 77: *WGM and Bragg thresholds.* Thresholds for WGMs and radial Bragg lasing in high refractive index LC droplets and corresponding planar cells with the same thickness.

Thresholds for both Bragg and WGM lasing are dependent on droplet size and are lower in bigger droplets because of higher Q-factors (Figure 77). The threshold for WGMs decreases faster with the droplet diameter than for Bragg lasing. The droplets below 25 µm have lower threshold for Bragg lasing, whereas above 25 µm the threshold is lower for WGMs. The smaller droplet with Bragg lasing is 15 µm in diameter and the smallest with WGM lasing is 19 µm in diameter. For planar cell filled with the same mixture as used for the droplets, the threshold is nearly constant with the thickness and is comparable to threshold for larger droplets.

4.8.8 Polymerizable 3D laser

It has been shown that lasing can also be achieved in polymerizable cholesteric LCs [111, 112] and cholesteric liquid crystalline elastomers [113]. The advantage of polymerizing the structure is that it can be stabilized. After polymerization the director structure remains the same, the order parameter does not change a lot, usually it increases and the thermal fluctuations are quenched. The LC is also not sensitive to changes in temperature and external fields any more. This is an advantage to achieve stable optical properties of the CLC, but on the other hand also a disadvantage, since the system is not tunable anymore. In the case of CLC lasers, the polymerization stabilizes the lasing, both the wavelength and the pulse-to-pulse energy. Since there are no more thermal fluctuations, the refractive index and the pitch are also not fluctuating and the lasing wavelength is more stable. The pump laser locally heats and reorients the LC causing even larger fluctuations, which is avoided by polymerization. Unfortunately, the polymerization increases the lasing threshold. Why this happens is not clear. In the case of droplets, the polymerization has additional advantage, in the sense, that we can also mechanically stabilize the droplets. They can be then extracted from the carrier fluid in the form of dry powder and can be incorporated in other materials or used as a single probes.

We have used a mixture of two photocurable cholesteric liquid crystals, CLC 03-008 (35.1 wt%) and CLC 03-009 (64.9 wt%) from Merck and DCM dye (1.2 wt%) [114]. The mixture was prepared by F. Araoka from Prof. H. Takazoe's laboratory. A small quantity of non-polymerizable ZLI-2293 was added to the mixture to precisely tune the PBG to the emission of the fluorescent dye. The droplets were prepared with the same procedure used for the non-polymerizable LCs. The dispersion was then introduced in between two glasses and illuminated with UV light for 5 minutes.

Droplets made in this way are similar in appearance as of non-polymerizable CLCs and the appearance does not change after polymerization (Figure 78b). However, almost all droplets larger than 30 μm have irregular defects inside. The reason for the formation of the defects is very large viscosity of the CLC which prevents the annihilation of defects. To reduce the viscosity, the CLC mixture can be heated to just bellow the clearing point before mixing with glycerol.

When illuminating a single polymerized droplet with a pulsed laser, a bright spot appears in the center as well as a ring on the surface (Figure 78c), corresponding to Bragg lasing and lasing of WGMs, respectively. Both can also be observed in the spectrum (Figure 78a). If the polymerized droplets would be transferred to a high refractive index material the WGMs would be suppressed and only Bragg lasing would be observed.

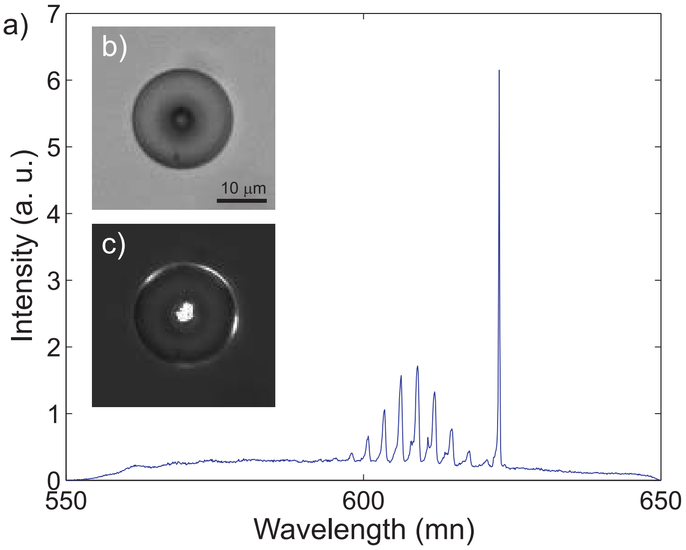

Figure 78: *Polymerized CLC spherical laser.* a) Lasing spectrum from a 20 μm polymerized CLC droplet. b) Optical micrograph of the same droplet and c) when it is illuminated by a pulsed laser.

Pulse-to-pulse stability of polymerized Bragg lasers was also measured. In Figure 79 the output energy versus the input energy is plotted. Each point represents a single 1 ns pulse. The energy of each pulse from the pump laser is not very stable, therefore to determine the input energy, the intensity of the non-lasing part of the spectrum (the fluorescent background) from the droplet was used as the reference for the input energy. The plotted output intensity is calculated as the surface below the laser peak. In the plot for polymerized droplet we can clearly see the lasing threshold (Figure 79a). In a small part of input intensities around the threshold, the laser is sometimes lasing, sometimes not. For the non-polymerizable sample (Figure 79b) this region of intermittent lasing is much wider and in general the points are much more scattered. Therefore, with polymerization we have achieved more stable lasing as also mechanically stabilized the droplets.

Polymerized CLC droplets without the dye could be also used as an material with interesting optical properties. The droplets could be introduced in a carrying medium that has

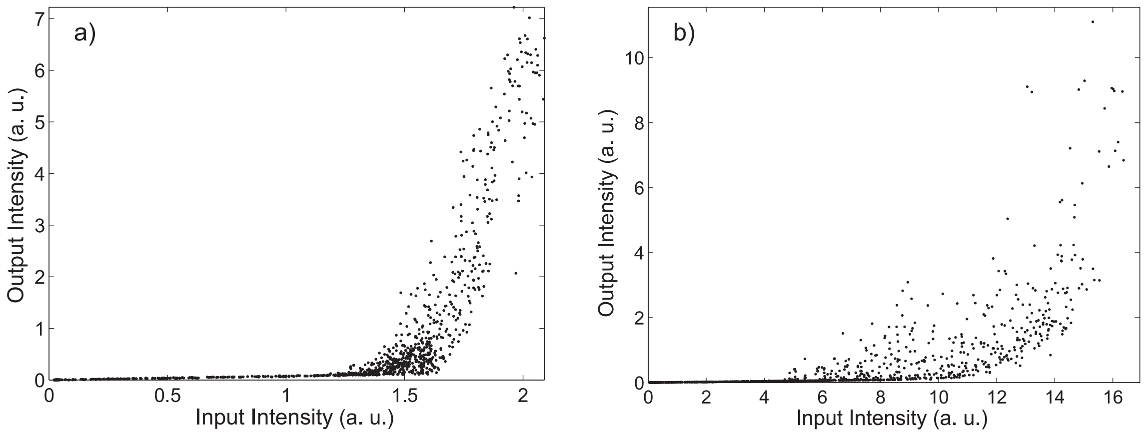

Figure 79: *Output intensity versus input intensity of single laser pulses.* Output intensity for a) polymerized droplet and b) non-polymerizable sample.

the refractive index the same as the average refractive index of the LC. The refractive index matching would prevent the droplets to act as lenses and the light to be scattered. Only the periodic structure would have an effect on the optical properties of such material. Because the droplets are spherically symmetric, they have photonic bandgap in all the directions, therefore their dispersion could also have an isotropic photonic bandgap.

4.8.9 Particles incorporated into a CLC droplet

In all the experiments with spherical CLC lasers the dye was dissolved in the CLC and was therefore distributed in the whole droplet. More efficient pumping could be achieved by only having the dye in the center of the droplet where there is the highest light intensity. In this way, also suppression of the spontaneous emission could be achieved. This could be done by introducing a fluorescent hard particle to the center of the droplet. The other reason for including a particle to the center of the droplet is to achieve defect mode lasing [53]. The same as in planar CLC cell where a thin layer of isotropic material is introduced in between layers of CLC, in the droplet this would be achieved by a spherical particle. Furthermore, a plasmon particle or nonlinear core material for second-harmonic generation could be used as an active core.

In the case of nematic droplets, the introduced particle is stable in the center of the droplet, where the defect is located (Section 4.1). We would expect something similar also in cholesteric droplets. In this case, planar anchoring on the surface of the particle would match the director configuration. To try to achieve this, we have first dispersed the solid particles into the CLC and then mixed this into the carrier medium using the same procedure as for nematic shells. We have used silica colloids with diameters from 150 nm up to 10 μm with either planar or homeotropic anchoring or gold nanoparticles without surface treatment. The results were in all case the same. The particles did not go into the center of the droplet, but rather to the radial defect line and most of the times where the defect line was pinned to the surface of the droplet.

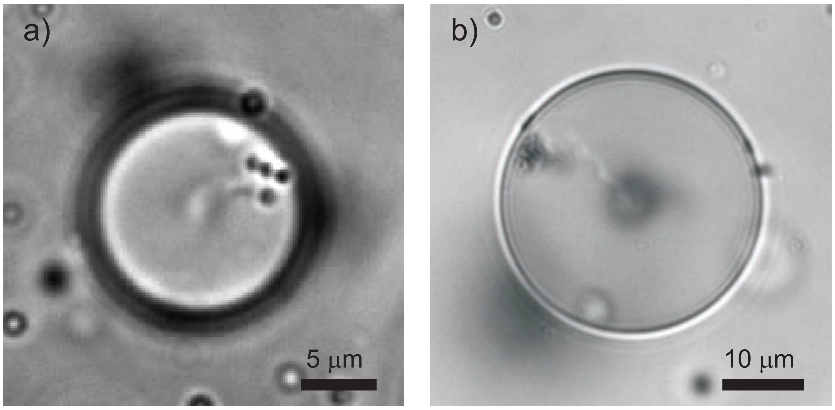

Figure 80: *A CLC spherical laser with included particles.* a) A CLC droplet in glycerol with incorporated 500 nm silica colloids and b) with gold nanoparticles. In both cases the defect line from the center of the droplet to the surface is visible. The particles aggregate on the surface where the defect line comes to the surface.

5 Conclusions

In the research work covered by this thesis, we have started a new area of research by using for the first time liquid-crystal droplets as optical microcavities. The use of LC droplets was before limited mostly to PDLC, where the optical modes were not supported inside the droplets, mostly because their small size. It has been shown already many years ago by theoretical and experimental groups, that liquid-crystal droplets are a very rich system. The variety of structures in the droplets reflects also in a variety of possible optical modes and their many possible applications. The structures in the droplets are self assembled because of elastic forces in LCs, which is a great advantage over solid state optical components, since no complicated fabrication methods are necessary. We have shown that nematic and cholesteric droplets can support optical modes. The modes in the two types of droplets are different in their properties, such as the intensity distribution, number of modes, polarization and direction of emission.

To observe, manipulate, excite and analyze the droplets and their spectral properties, an optical setup build around an inverted microscope was used. The old setup that included a green and an infrared tweezers was upgraded with a pulsed laser and a spectrometer with a cooled EMCCD camera. Software was written to control most of the devices in the optical setup including temperature, electric field and position of the sample.

First, radial nematic droplets were used as optical microcavities [83]. They were prepared just by mechanical mixing of a nematic LC and a carrying fluid. It was found that PDMS is a good choice as a carrying medium, since it gives homeotropic anchoring and can be polymerized to fix the droplets. Prior to the polymerization, single droplets can also be manipulated by the laser tweezers and assembled into arbitrary structures. Instead of using just LC also hard particles can be introduced in droplets, and can sit in the center of the droplet making a thin shell of LC. The LC used in most experiments was doped with a fluorescent dye and a single droplet was illuminated by a laser through a microscope objective. Droplets can also be excited by introducing a fiber into the sample. Fluorescent signal was sent to a spectrophotometer and analyzed. Narrow spectral peaks in the spectrum were identified as WGM and by fitting to theory, the mode numbers were identified. Compared to isotropic spheres, the two polarizations (TE and TM) of the modes sense different refractive indices and are decoupled from each other. In our case the TM modes have much higher Q-factors and is small droplets no TE modes are observed. The Q-factor of WGMs in droplets larger than 30 μm is up to 12,000, limited by the resolution of the spectrometer used to analyze the signal. For both radial and bipolar nematic droplets also low-threshold lasing has been achieved by using a pulsed laser as an excitation source.

After showing that LC droplets can support WGMs, the natural next step was to apply electric field to the droplets. The electric filed changes the nematic director orientation inside the droplets, which has an effect on the average refractive index for the light traveling inside the droplet. By applying moderate field of up to 2.6 V/μm we were able to tune the WGMs by almost 20 nm for the modes near 600 nm [83, 115]. This is one or two orders of magnitude more than achieved before in solid state microresonators. The tunability is almost linear and completely reversible. It exceeds the free spectral range of the cavity, so that the modes can be shifted to any wavelength.

The WGMs in a LC droplet can also be tuned by temperature [116]. The refractive indices of LCs are highly temperature dependent. By increasing the temperature the ordinary index increases and the extraordinary index decreases. Therefore, also the TE and the TM modes are shifted to longer or shorter wavelengths, respectively. The tunability for E12 LC droplets is approximately 15 nm for temperature change of 30 K. The tunability, except very near the transition temperature, is completely reversible and exceeds the FSR. The tuning of single droplets can also be achieved by local heating with a laser. The LC WGM cavities can also be used as temperature sensor, a single droplet indicating local temperature in a sample.

The third way of achieving tunability is by mechanical deformation [116]. A thin free standing film of polymerized PDMS containing the droplets was mechanically stretched and the positions of the modes were measured. At 15% strain the mode shift is more than 30 nm. The tuning mechanism is in this case not connected to the nematic director configuration or order, but it has pure geometrical origin. Namely, the deformation changes the geometrical path of the light, which is the same as it would be in an isotropic droplet. The tunability is also in this case completely reversible and exceeds the FSR.

We have further demonstrated, that by observing optical modes in dye doped nematic LC droplets in water, they can be used as versatile chemical sensor [117]. Foreign surfactant molecules adsorb to the LC-water interface influencing the surface anchoring, which in turn changes the LC ordering inside the droplet and effects the frequencies of the WGMs. In contrast to solid WGM microresonators, the molecules that bind to the LC-water interface, do not change refractive index just locally, but the perturbation is propagated into the bulk LC by long range interactions. We demonstrate that the presence of 0.3 mM concentration of SDS in water induces significant and clearly detectable changes in the lasing spectrum from WGMs. The developed sensing method could be easily integrated into existing microfluidics chips. Monodispersed LC droplets could be formed within a microchannel and the excitation and detection of fluorescent light could be achieved through the integrated optical fibers [118]. Monitoring and automated recognition of the lasing spectra from LC microdroplets has therefore a clear advantage in comparison to the conventional observation of individual droplets under an optical microscope and could provide efficient and automated readout of the presence of targeted molecules in water surrounding the LC microdroplet sensor.

We have extended lasing principle in cholesteric liquid crystals from planar geometry into a spherical one [119, 120]. A small quantity of dye doped cholesteric liquid crystal was mechanically mixed with an external carrier fluid such as glycerol. In the process of mechanical mixing thousands of droplets with different sizes were produced. Each droplet has a spherulite structure that corresponds to the helical pitch having radial direction and being equivalent to a Bragg onion resonator. When a single droplet was illuminated by a Q-switched doubled Nd:YAG laser, a narrow spectral line appeared above the lasing threshold. The linewidth was 0.1 nm and the laser line was positioned at 620 nm, matching the longer wavelength photonic bandgap edge. Lasing could also be observed as a bright spot in the center of the droplet. The lasing wavelength is not dependent on the droplet size and can be arbitrarily selected from UV to IR by utilizing liquid crystal with proper pitch length and a proper fluorescent dye. By changing the temperature of the droplet, the cholesteric pitch is varied and the position of the laser line can be tuned by several tens of nanometers. The temperature change of 13 K shifts the laser line by 40 nm. By measuring the angle dependence of the emission we have found that the emission is highly uniform and the laser is really emitting light isotropically, thus the laser is acting as a coherent, point-like, omnidirectional source of light. A number of other characteristics of the laser, such as the polarization, stability, linewidth as a function of droplet size and thresholds have been measured. Also multimode lasing has been achieved. A number of applications of the cholesteric onion microlasers is anticipated, such as holography, telecommunications, optical computing, imaging, sensing and even as a material for paints [47] or light sources that emit coherent light in all directions. By polymerizing the liquid crystal itself, a more mechanically stable microlaser can be made, useful for example in biological imaging. Furthermore, the 3D cholesteric laser is also one of the simplest lasers to make in general. Only four commercially available substances are needed: a nematic liquid crystal, a chiral dopant, a fluorescent dye and a fluid as the external medium. No complicated mixing procedures are needed and the whole process can be completed in less than fifteen minutes in any laboratory. Coupled regular arrays of thousands and even millions of CLC microlasers could also be made. We anticipate that by using better materials and optimized material parameters, such as the concentration of the chiral dopant and of the fluorescent dye, it will be possible to further reduce the size and increase the tunability and the functionality of the cholesteric onion lasers. The CLC onion microlasers could also be combined with optical fiber waveguides to collect radiating light into the waveguides. Omnidirectional laser emission is one of the more relevant results of the dissertation, since there are just few known lasers that emit light in all directions in space. This is probably the only such laser source that is also highly tunable at the same time. We also have to emphasize that lasing in a spherical Bragg structure has been achieved for the first time.

By using different LC materials such as smectic, ferroelectric, discotic, blue phase and others, plus different shapes of the droplets and by applying external fields, an almost infinite number of combinations are possible. The final idea is not to use the LC droplets as single optical components integrated in some other solid state optics, but to have the whole integrated photonic structure made from soft materials. This opens a new area of research called *soft photonics*. All living creatures have extraordinary complexity and are made mostly of soft matter, the single building blocks being self assembled by complex interactions. Why not to have an artificially made photonic circuit that is entirely composed of soft materials and the single components being self assembled to the right positions. Bottom-up approach would in this case enable cheap, large scale production of such photonic structures without the need of complex procedures such as lithography that is limited just to planar geometries. Such soft structures would also have a number of useful properties such as tunability, real time reconfigurability and self healing. There is still a lot of work to be done in order for this self assembled structures to be realizable. However, some simple cases could be manufactured with current knowledge and technology. It has been shown that hard particles embedded in a LC can be self assembled in a variety of structures [68–72]. In this way, the microcavities could be self assembled in various structures such as CROWs and connected to other solid state components. Coupling the resonators with waveguides could lead to efficient extraction of light from cavities, as well as a potential to use them as filters and routers.

The work in this dissertation has great potential in future micro-optics circuits as well as in basic research. Form application point of view this work could have impact on the development of a number of tunable optical elements, such as microlasers, narrow filters, optical switching and routing, ultrasensitive biosensing, temperature and displacement measurements, high resolution spectroscopy, etc. Liquid-crystal resonators, could be useful not just for commercial applications, but also in various studies such as nonlinear optics, cavity quantum electrodynamics and single photon sources.

6 Acknowledgements

First, great thanks to my supervisor Prof. Igor Muševič for remarkable guidance over the entire duration of the PhD, giving wonderful scientific ideas, objective criticism, but at the same time allowing me enough scientific freedom to develop my own ideas and methods.

Special thanks to Asst. Prof. Miha Škarabot for teaching me the experimental work as well as giving me countless advices and making my work at the institute especially pleasant. As well I would like to thank Prof. Denis Arčon that introduced me to the research work in the first place and encouraged me to work in science.

I am very grateful to my coworkers Dr. Andriy Nych, Dr. Uliana Ognysta, Dr. Uroš Tkalec, Dr. Rok Žitko, Dr. Anna V. Ryzhkova, Venkata Subba Rao Jampani, Maryam Nikkhoo and Huan Peng that we spent together infinite number of days in the laboratory and office, for sharing the knowledge and making my working days enjoyable.

I would also like to thank Prof. Slobodan Žumer, Dr. Miha Ravnik, David Seč and Iztok Bajc for the insight into the theoretical background, for handing simulation results as well as for many fruitful suggestions.

I also express my thanks to Ivan Kvasić, Silvano Mendizza, Silvija Pirš, Dr. Janez Pirš, Dr. Laura Ramón Giménez, Dr. Polona Umek, Dr. Blaž Zupančič, Dr. Erik Zupanič, Nika Košir, Dr. Fumito Araoka, Prof. Hideo Takezoe, Dr. Manca Logar, Mag. Slavko Kralj, Dr. Stane Pajk, Prof. Slavko Pečar, Dr. Polonca Ropret, Dr. Daniele Biglino, Prof. Janez Štrancar, Asst. Prof. Zoran Arsov and Dr. Tilen Koklič. They helped me with small, but important details, that made my work possible.

Thanks to Andreja Eršte and Dr. Erik Zupanič for the LaTeX template that greatly simplified the writing of the thesis.

Finally, I would like to sincerely thank my parents Marjan and Vera, grandfather Milan, as well as Maja for the support they offered me all along. To them I dedicate this thesis.

7 Zahvala

Najlepša hvala Prof. Dr. Igorju Muševiču za izjemno pomoč in usmerjanje preko celotnega doktorskega raziskovanja, za posredovanje odličnih znanstvenih idej, objektivne kritičnosti in hkrati omogočanja razvoja lastnih znanstvenih idej in metod.

Posebna zahvala gre Doc. Dr. Mihi Škarabotu, ki me je vpeljal v eksperimentalno delo. Hvala za številne nasvete in pozitivno energijo pri delu. Hvala tudi Prof. Dr. Denisu Arčonu za prvo seznanitev z raziskovalnim delom, ter spodbudo za nadaljevanje dela v znanosti.

Zelo sem hvaležen sodelavcem Dr. Andriyu Nychu, Dr. Uliani Ognysti, Dr. Urošu Tkalcu, Dr. Roku Žitkotu, Dr. Anni V. Ryzhkovi, Venkati Subba Rao Jampaniju, Maryam Nikkhoo in Huanu Pengu s katerimi sem preživel številne ure v laboratoriju in pisarni, za izmenjavo izkušenj in znanja, ter ustvarjanja prijetnega delovnega vzdušja.

Zahvaljujem se tudi Prof. Dr. Slobodanu Žumru, Dr. Mihi Ravniku, Davidu Seču in Iztoku Bajcu za vpogled v teoretično delo, za rezultate simulacij in številne uporabne nasvete.

Hvala tudi Ivanu Kvasiću, Silvanu Mendizzi, Silviji Pirš, Dr. Janezu Piršu, Dr. Lauri Ramón Giménez, Dr. Poloni Umek, Dr. Blažu Zupančiču, Dr. Eriku Zupaniču, Niki Košir, Dr. Fumitu Araoki, Prof. Dr. Hideu Takezoi, Dr. Manci Logar, Mag. Slavku Kralju, Dr. Stanetu Pajku, Prof. Dr. Slavku Pečarju, Dr. Polonci Ropret, Dr. Danielu Biglinu, Prof. Dr. Janezu Štrancaru, Doc. Dr. Zoranu Arsovu in Dr. Tilnu Kokliču za pomoč pri majhnih, ampak zato nič manj pomembnih detajlih, brez katerih moje delo ne bi bilo mogoče.

Hvala Andreji Eršte in Dr. Eriku Zupaniču za LaTeX predlogo, ki mi je olajšala pisanje doktorske disertacije.

Na koncu se iskreno zahvaljujem mojim staršem Marjanu in Veri, dedku Milanu, kot tudi Maji za neprecenljivo podporo. Njim tudi posvečam to doktorsko disertacijo.

8 References

[1] Vahala, K. J. Optical microcavities. *Nature* **424**, 839–846 (2003).

[2] Painter, O.; Lee R. K., Scherer A., Yariv A., O'Brien J. D., Dapkus P. D., Kim I. Two-dimensional photonic band-gap defect mode laser. *Science* **284**, 1819–1821 (1999).

[3] Jewell, J. L.; McCall, S. L.; Lee, Y. H.; Scherer, A.; Gossard, A. C.; English, J. H. Lasing characteristics of GaAs microresonators. *Appl. Phys. Lett.* **54**, 1400–1402 (1989).

[4] Treussart, F.; Dubreuil, N.; Knight, J. C.; Sandoghdar, V.; Hare, J.; Lefcvre-Seguin, V.; Raimond, J.-M.; Haroche, S. Microlasers based on silica microspheres. *Ann. Telecommun.* **52**, 557–568 (1997).

[5] Cao, W.; Munoz, A.; Palffy-Muhoray, P.; Taheri, B. Lasing in a three-dimensional photonic crystal of the liquid crystal blue phase II. *Nat. Mater.* **1**, 111–113 (2002).

[6] Noginov, M. A.; Zhu, G.; Belgrave, A. M.; Bakker, R.; Shalaev, V. M.; Narimanov, E. E.; Stout, S.; Herz, E.; Suteewong, T.; Wiesner, U. Demonstration of a spaser-based nanolaser. *Nature* **460**, 1110–1112 (2009).

[7] Hill, M. T.; Oei, Y.-S.; Smalbrugge, B.; Zhu, Y.; de Vries, T.; van Veldhoven, P. J.; van Otten, F. W. M.; Eijkemans, T. J.; Turkiewicz, J. P.; de Waardt, H.; Geluk, E. J.; Kwon, S.-H.; Lee, Y.-H.; Notzel, R.; Smit, M. K. Lasing in metallic-coated nanocavities. *Nat. Photonics* **1**, 589–594 (2007).

[8] Ashkin, A.; Dziedzic, J. M. Observation of resonances in the radiation pressure on dielectric spheres. *Phys. Rev. Lett.* **38**, 1351–1354 (1977).

[9] Vernooy, D. W.; Ilchenko, V. S.; Mabuchi, H.; Streed, E. W.; Kimble, H. J. High-Q measurements of fused-silica microspheres in the near infrared. *Opt. Lett.* **23**, 247–249 (1998).

[10] Armani, A.; M. Kulkarni, R. P.; Fraser, S. E.; Flagan, R. C.; Vahala, K. J. Label-free, single-molecule detection with optical microcavities. *Science* **317**, 783–787 (2007).

[11] Chang, R. K.; Campillo, A. J. *Optical Processes in Microcavities* (World Scientific, Singapore, 1998).

[12] Maune, B.; Lawson, R.; Gunn, C.; Scherer, A.; Dalton, L. Electrically tunable ring resonators incorporating nematic liquid crystals as cladding layers. *Appl. Phys. Lett.* **83**, 4689–4691 (2003).

[13] Piegdon, K. A.; Matthias, H.; Meier, C.; Kitzerow, H.-S. Tunable optical properties of photonic crystals and semiconductor microdisks using liquid crystals. *Proc. SPIE Int. Soc. Opt. Eng.* **6911**, 69110J (2008).

[14] Wang, T.-J.; Chu, C.-H.; Lin, C.-Y. Electro-optically tunable microring resonators on lithium niobate. *Opt. Lett.* **32**, 2777–2779 (2007).

[15] Kiraz, A.; Karadag, Y.; Coskun, A. F. Spectral tuning of liquid microdroplets standing on superhydrophobic surface using electrowetting. *Appl. Phys. Lett.* **92**, 191104 (2008).

[16] von Klitzing, W.; Long, R.; Ilchenko, V. S.; Hare, J.; Lefevre-Seguin, V. Tunable whispering gallery modes for spectroscopy and CQED experiments. *New. J. Phys.* **3**, 14.1–14.14 (2001).

[17] Ma, Q.; Rossmann, T.; Guo, Z. Whispering-gallery mode silica microsensors for cryogenic to room temperature measurement. *Meas. Sci. Technol.* **21**, 025310–025317 (2010).

[18] Dong, C.-H.; He, L.; Xiao, Y.-F.; Gaddam, V. R.; Ozdemir, S. K.; Han, Z.-F.; Guo, G.-C.; Yang, L. Fabrication of high-Q polydimethylsiloxane optical microspheres for thermal sensing. *Appl. Phys. Lett.* **94**, 231119 (2009).

[19] Saito, M.; Shimatani, H.; Naruhashi, H. Tunable whispering gallery mode emission from a microdroplet in elastomer. *Opt. Express* **16**, 11915–11919 (2008).

[20] Ioppolo, T.; Kozhevnikov, M.; Stepaniuk, V.; Otugen, M. V.; Sheverev, V. Micro-optical force sensor concept based on whispering gallery mode resonators. *Appl. Optics* **47**, 3009–3014 (2008).

[21] Vollmer, F. *Resonant Detection of Nano to Microscopic Objects Using Whispering Gallery Modes* (Thesis, Rockefeller University, New York, 2004).

[22] Vollmer, F.; Arnold, S. Whispering-gallery-mode biosensing: label-free detection down to single molecules. *Nat. Methods* **5**, 591–596 (2008).

[23] Heebner, J. E.; Grover, R.; Ibrahim, T.; Ibrahim, T. A. *Optical Microresonators: Theory, Fabrication, And Applications* (Springer, London, 2008).

[24] Mukaiyama, T.; Takeda, K.; Miyazaki, H.; Jimba, Y.; Kuwata-Gonokami, M. Tight-binding photonic molecule modes of resonant bispheres. *Phys. Rev. Lett.* **82**, 4623–4626 (1999).

[25] Rakovich, Y. P.; Donegan, J. F.; Gerlach, M.; Bradley, A. L.; Connolly, T. M.; Boland, J. J.; Gaponik, N.; Rogach, A. Fine structure of coupled optical modes in photonic molecules. *Phys. Rev. A* **70**, 051801–051801 (2004).

[26] Poon, J. K. S.; Zhu, L.; DeRose, G. A.; Yariv, A. Polymer microring coupled-resonator optical waveguides. *J. Lightwave Technol.* **24**, 1843–1849 (2006).

[27] Chen, Z.; Taflove, A.; Backman, V. Highly efficient optical coupling and transport phenomena in chains of dielectric microspheres. *Opt. Lett.* **31**, 389–391 (2006).

[28] Shaw, A.; Roycroft, B.; Hegarty, J.; Labilloy, D.; Benisty, H.; Weisbuch, C.; Krauss, T. F.; Smith, C. J. M.; Stanley, R.; Houdre, R.; Oesterle, U. Lasing properties of disk microcavity based on a circular Bragg reflector. *Appl. Phys. Lett.* **75**, 3051–3053 (1999).

[29] Scheuer, J.; Green, W. M. J.; DeRose, G. A.; Yariv, A. InGaAsP annular Bragg lasers: theory, applications and modal properties. *IEEE J. Sel. Top. Quant.* **11**, 476–484 (2005).

[30] Scheuer, J.; Green, W. M. J.; DeRose, G.; Yariv, A. Low-threshold two-dimensional annular Bragg lasers. *Opt. Lett.* **29**, 2641–2643 (2004).

[31] Sullivan, K. G.; Hall, D. G. Radiation in spherically symmetric structures, I. The coupled-amplitude equations for vector spherical waves. *Phys. Rev. A* **50**, 2701–2707 (1994).

[32] Brady, D.; Papen, G.; Sipe, J. E. Spherical distributed dielectric resonators. *J. Opt. Soc. Am. B* **10**, 644–657 (1993).

[33] Burlak, G. N. Optical radiation from coated microsphere with active core. *Phys. Lett. A* **299**, 94–101 (2002).

[34] Xu, Y.; Liang, W.; Yariv, A.; Fleming, J. G.; Lin, S.-Y. Modal analysis of Bragg onion resonators. *Opt. Lett.* **29**, 424–426 (2004).

[35] Tandaechanurat, A.; Ishida, S.; Aoki, K.; Guimard, D.; Nomura, M.; Iwamoto, S.; Arakawa, Y. Demonstration of high-Q (>8600) three-dimensional photonic crystal nanocavity embedding quantum dots. *Appl. Phys. Lett.* **94**, 171115 (2009).

[36] Gourevich, I.; Field, L. M.; Wei, Z.; Paquet, C.; Petukhova, A.; Alteheld, A.; Kumacheva, E.; Saarinen, J. J.; Sipe, J. E. Polymer multilayer particles: A route to spherical dielectric resonators. *Macromolecules* **39**, 1449–1454 (2006).

[37] Scheuer, J. Radial Bragg lasers: optimal design for minimal threshold levels and enhanced mode discrimination. *J. Opt. Soc. Am. B* **24**, 2178–2184 (2007).

[38] de Gennes, P. G.; Prost, J. *The Physics of Liquid Crystals, 2nd ed.* (Oxford Science, Oxford, 1993).

[39] Song, M.; Park, B.; Nishimura, S.; Toyooka, T.; Chung, I.; Takanishi, Y.; Ishikawa, K.; Takezoe, H. Electrotunable non-reciprocal laser emission from a liquid-crystal photonic device. *Adv. Funct. Mater.* **16**, 1793–1798 (2006).

[40] Hands, P. J. W.; Morris, S. M.; Wilkinson, T. D.; Coles, H. J. Two-dimensional liquid crystal laser array. *Opt. Lett.* **33**, 515–517 (2008).

[41] Munoz, A.F.; Palffy-Muhoray, P.; Taheri, N. Ultraviolet lasing in cholesteric liquid crystals. *Opt. Lett.* **26**, 804–806 (2001).

[42] Moreira, M. F.; Carvalho, I. C. S.; Cao, W.; Bailey, C.; Taheri, B.; Palffy-Muhoray P. Cholesteric liquid-crystal laser as an optic fiber-based temperature sensor. *Appl. Phys. Lett.* **85**, 2691–2693 (2004).

[43] Morris, S. M.; Ford, A. D.; Pivnenko, M. N.; Coles, H. J. Enhanced emission from liquid crystal lasers. *J. Appl. Phys.* **97**, 023103 (2005).

[44] Humar, M.; Škarabot, M.; Ravnik, M.; Žumer, S.; Poberaj, I.; Babič, D.; Muševič I. Electrically tunable diffraction of light from 2D nematic colloidal crystals. *Eur. Phys. J. E* **27**, 73–79 (2008).

[45] Drzaic, P. S. *Liquid Crystal Dispersions* (World Scientific, Singapore, 1995).

[46] Doane, J. W.; Vaz, N. A.; Wu, B.-G.; Žumer, S. Field controlled light scattering from nematic microdroplets. *Appl. Phys. Lett.* **48**, 269–271 (1986).

[47] Hands, P. J. W.; Gardiner, D. J.; Morris, S. M.; Mowatt, C.; Wilkinson, T. D.; Coles, H. J. Band-edge and random lasing in paintable liquid crystal emulsions. *Appl. Phys. Lett.* **98**, 141102 (2011).

[48] Lee, C.-R.; Lin, S.-H.; Guo, C.-H.; Chang, S.-H.; Mo, T.-S.; Chu, S.-C. All-optically controllable random laser based on a dye-doped polymer-dispersed liquid crystal with nano-sized droplets. *Opt. Express* **18**, 2406–2412 (2010).

[49] Kopp, V. I.; Fan, B.; Vithana, H. K. M.; Genack, A. Z. Low-threshold lasing at the edge of a photonic stop band in cholesteric liquid crystals. *Opt. Lett.* **23**, 1707–1709 (1998).

[50] Taheri, B.; Munoz, A.; Palffy-Muhoray P.; Twieg, R. Low threshold lasing in cholesteric liquid crystals. *Mol. Cryst. Liq. Cryst.* **358**, 73–82 (2001).

[51] Alvarez, E.; He, M.; Munoz, A. F.; Palffy-Muhoray, P.; Serak, S. V.; Taheri, B.; Tweig, R. Mirrorless lasing and energy transfer in cholesteric liquid crystals doped with dyes. *Mol. Cryst. Liq. Cryst.* **369**, 75–82 (2001).

[52] Ford, A. D.; Morris, S. M.; Coles, H. J. Photonics and lasing in liquid crystals. *Mater. Today* **9**, 36–42 (2006).

[53] Jeong, S. M.; Ha, N. Y.; Takanishi, Y.; Ishikawa, K.; Takezoe, H.; Nishimura, S.; Suzaki, G. Defect mode lasing from a double-layered dye-doped polymeric cholesteric liquid crystal films with a thin rubbed defect layer. *Appl. Phys. Lett.* **90**, 261108 (2007).

[54] Araoka, F.; Shin, K.-C.; Takanishi, Y.; Ishikawa, K.; Takezoe, H.; Zhu, Z.; Swager, T. M. How doping a cholesteric liquid crystal with polymeric dye improves an order parameter and makes possible low threshold lasing. *J. Appl. Phys.* **94**, 279–283 (2009).

[55] Coles, H.; Morris, S. Liquid-crystal lasers. *Nat. Photonics* **4**, 676–685 (2010).

[56] Rasing, T.; Muševič, I. *Surfaces and Interfaces of Liquid Crystals* (Springer, Berlin, Heidelberg, New York, 2004).

[57] Brake, J. M.; Daschner, M. K.; Abbott, N. L. Formation and characterization of phospholipid monolayers spontaneously assembled at interfaces between aqueous phases and thermotropic liquid crystals. *Langmuir* **21**, 2218–2228 (2005).

[58] Brake, J. M.; Daschner, M. K.; Luk, Y. Y.; Abbott, N. L. Biomolecular interactions at phospholipid-decorated surfaces of liquid crystals. *Science* **302**, 2094–2097 (2003).

[59] Luk, Y. Y.; Tingey, M. L.; Dickson, K. A.; Raines, R. T.; Abbott, N. L. Imaging the binding ability of proteins immobilized on surfaces with different orientations by using liquid crystals. *J. Am. Chem. Soc.* **126**, 9024–9032 (2004).

[60] Jang, C.-H.; Cheng, L.-L.; Olsen, C. W.; Abbott, N. L. Anchoring of nematic liquid crystals on viruses with different envelope structures. *Nano Lett.* **6**, 1053–1058 (2006).

[61] Sivakumar, S.; Wark, K. L.; Gupta, J. K.; Abbott, N. L.; Caruso, F. Liquid crystal emulsions as the basis of biological sensors for the optical detection of bacteria and viruses. *Adv. Funct. Mater.* **19**, 2260–2265 (2009).

[62] Kinsinger, M. I.; Sun, B.; Abbott, N. L.; Lynn, D. M. Reversible control of ordering transitions at aqueous/liquid crystal interfaces using functional amphiphilic polymers. *Adv. Mater.* **19**, 4208–4212 (2007).

[63] Shah, R. R.; Abbott, N. L. Principles for measurement of chemical exposure based on recognition-driven anchoring transitions in liquid crystals. *Science* **293**, 1296–1299 (2001).

[64] Lockwood, N. A.; Abbott, N. L. Self-assembly of surfactants and phospholipids at interfaces between aqueous phases and thermotropic liquid crystals. *Current Opinion in Colloid & Interface Science* **10**, 111–120 (2005).

[65] Gupta, J. K.; Zimmerman, J. S.; de Pablo, J. J.; Caruso, F.; Abbott, N. L. Characterization of adsorbate-induced ordering transitions of liquid crystals within monodisperse droplets. *Langmuir* **25**, 9016–9024 (2009).

[66] Tjipto, E.; Cadwell, K. D.; Quinn, J. F.; Johnston, A. P. R.; Abbott, N. L.; Caruso, F. Tailoring the interfaces between nematic liquid crystal emulsions and aqueous phases via layer-by-layer assembly. *Nano Lett.* **6**, 2243–2248 (2006).

[67] Lin, I-H.; Miller, D. S.; Bertics, P. J.; Murphy, C. J.; de Pablo, J. J.; Abbott, N. L. Endotoxin-induced structural transformations in liquid crystalline droplets. *Science* **332**, 1297–1300 (2011).

[68] Poulin, P.; Stark, H.; Lubensky, T. C.; Weitz, D. A. *Science* **275**, 1770–1773 (1997).

[69] Muševič, I.; Škarabot, M.; Tkalec, U.; Ravnik, M.; Žumer, S. Two-dimensional nematic colloidal crystals self-assembled by topological defects. *Science* **313**, 954–958 (2006).

[70] Ravnik, M.; Škarabot, M.; Žumer, S.; Tkalec, U.; Poberaj, I.; Babič, D.; Osterman, N.; Muševič, I. Entangled nematic colloidal dimers and wires. *Phys. Rev. Lett.* **99**, 247801 (2007).

[71] Škarabot, M.; Ravnik, M.; Žumer, S.; Tkalec, U.; Poberaj, I.; Babič, D.; Muševič, I. Hierarchical self-assembly of nematic colloidal superstructures. *Phys. Rev. E* **77**, 061706 (2008).

[72] Tkalec, U.; Ravnik, M.; Čopar, S.; Žumer, S.; Muševič, I. Reconfigurable knots and links in chiral nematic colloids. *Science* **333**, 62–65 (2011).

[73] Ognysta, U.; Nych, A. B.; Škarabot, M.; Muševič, I. 3D dipolar structure in nematic liquid crystal. In: *Book of abstracts of the* 11th *European Conference on Liquid Crystals.* O62 (Maribor, 2011).

[74] Wua, S.-T. Absorption measurements of liquid crystals in the ultraviolet, visible, and infrared. *J. Appl. Phys.* **84**, 4462–4465 (1998).

[75] Spillane, S. M. *Fiber-coupled Ultra-high-Q Microresonators for Nonlinear and Quantum Optics* (Thesis, California Institute of Technology, Pasadena, 2004).

[76] Tona, M. *Study on Spherical Microlasers Levitated in an Ion Trap* (Thesis, Kochi University of Technology, 2002).

[77] Novotny, L.; Hesht, B. *Principles of Nano-Optics*, (Cambridge University Press, Cambridge, 2006).

[78] Bohren, C. F.; Huffman, D. R. *Absorption and Scattering of Light by Small Particles* (Wiley Science, New York, 1998).

[79] Lam, C. C.; Leung, P. T.; Young, K. Explicit asymptotic formulas for the positions, widths, and strengths of resonances in Mie scattering. *J. Opt. Soc. Am. B* **9**, 1585–1592 (1992).

[80] Schiller, S. Asymptotic expansion of morpliological resonance frequencies in Mie scattering. *Appl. Optics* **32**, 2181–2185 (1993).

[81] Gorodetsky M. L.; Fomin A. E., Geometrical theory of whispering-gallery modes. *IEEE J. Sel. Top. Quant.* **12**, 33–39 (2006).

[82] Cohoon, D.K. An exact solution of Mie type for scattering by a multilayer anisotropic sphere. *J. Electromagnet. Wave.* **3**, 421–448 (1989).

[83] Humar, M.; Ravnik, M.; Pajk, S.; Muševič, I. Electrically tunable liquid crystal optical microresonators. *Nat. Photonics* **3**, 595–600 (2009).

[84] Hecht, E. *Optics* (Addison Wesley, San Francisco, 2002).

[85] Saleh, B. E. A.; Teich, M. C. *Fundamentals of Photonics* (Wiley-Interscience, New York, 1991).

[86] Kaliteevski, M. A.; Brand, S.; Abram, R. A.; Nikolaev, V. V. Optical eigenmodes of a multilayered spherical microcavity. *J. Mod. Optic.* **48**, 1503–1516 (2001).

[87] Sun X.; Yariv, A. Surface-emitting circular DFB, disk- and ring- Bragg resonator lasers with chirped gratings: a unified theory and comparative study. *Opt. Express* **16**, 9155–9164 (2008).

[88] Yang, D.-K.; Wu, S.-T. *Fundamentals of Liquid Crystals Devices* (John Wiley & Sons Ltd, Chichester, 2006).

[89] Li, J.; Wen, C.-H.; Gauza, S.; Lu, R.; Wu, S.-T. Refractive indices of liquid crystals for display applications. *IEEE/OSA J. Disp. Technol.* **1**, 51–61 (2005).

[90] http://www.sigmaaldrich.com/ (accessed November 2011).

[91] Lockwood, N. A.; Gupta, J. K.; Abbott, N. L. Self-assembly of amphiphiles, polymers and proteins at interfaces between thermotropic liquid crystals and aqueous phases. *Surf. Sci. Rep.* **63**, 255–293 (2008).

[92] Hamlington, B. D.; Steinhaus, B.; Feng, J. J.; Link, D.; Shelley, M. J.; Shen, A. Q. Liquid crystal droplet production in a microfluidic device. *Liq. Cryst.* **34**, 861–870 (2007).

[93] Stark, H. Physics of colloidal dispersions in nematic liquid crystals. *Phys. Rep.* **351**, 387–474 (2001).

[94] Smalyukh, I. I.; Shiyanovskii, S. V.; Lavrentovich, O. D. Three-dimensional imaging of orientational order by fluorescence confocal polarizing microscopy. *Chem. Phys. Lett.* **336**, 88–96 (2001).

[95] Bodnar, V. G.; Lavrentovich, O. D.; Pergamenshchik, V. M. Threshold of structural hedgehog-ring transition in drops of a nematic in an alternating electric field. *Sov. Phys. JETP* **74**, 60–67 (1992).

[96] Gu, Y.; Abbott, N. L. Observation of Saturn-ring defects around solid microspheres in nematic liquid crystals. *Phys. Rev. Lett.* **85**, 4719–4722 (2000).

[97] Eversole, J. D.; Lin, H-B.; Campillo, A. J. Input/output resonance correlation in laser-induced emission from microdroplets. *J. Opt. Soc. Am. B* **12**, 287–296 (1995).

[98] Demus, D. (ed.); Goodby, J. (ed.); Gray, G. W. (ed.); Spiess, H.-W. (ed.); Vill V. (ed.) *Handbook of Liquid Crystals, Vol. 1: Fundamentals* (Wiley-VCH, Weinheim, 1998).

[99] Muševič, I.; Škarabot, M.; Babič, D.; Osterman, N.; Poberaj, I.; Nazarenko, V.; Nych, A. Laser trapping of small colloidal particles in a nematic liquid crystal: clouds and ghosts. *Phys. Rev. Lett.* **93**, 188101 (2004).

[100] Kiraz, A.; Yavuz, Ç.; Karadag, Y.; Kurt, A.; Sennaroglu, A.; Çankaya, H. Large spectral tuning of liquid microdroplets standing on a superhydrophobic surface using optical scattering force. *Appl. Phys. Lett.* **91**, 231102 (2007).

[101] Rey, A. D. Thermodynamics of soft anisotropic interfaces. *J. Chem. Phys.* **120**, 2010–2019 (2004).

[102] Bezić, J.; Žumer, S. Structures of the cholesteric liquid crystal droplets with parallel surface anchoring. *Liq. Cryst.* **11**, 593–619 (1992).

[103] Bouligand, Y.; Livolant, F. The organization of cholesteric spherulites. *J. Phys.-Paris* **45**, 1899–1923 (1984).

[104] Yang, D. K.; Crooker, P. P. Field-induced textures of polymer-dispersed chiral liquid crystal microdroplets. *Liq. Cryst.* **9**, 245–251 (1991).

[105] Kitzerow, H.-S.; Crooker, P. P. Behaviour of polymer dispersed cholesteric droplets with negative dielectric anisotropy in electric fields. *Liq. Cryst.* **11**, 561–568 (1982).

[106] Kurik M. V.; Lavrentovich O. D. Negative-positive monopole transitions in cholesteric liquid crystals. *Pis'ma Zh. eksp. teor., Fiz.* **35**, 445–447 (1992).

[107] Seč, D.; Porenta, T.; Žumer, S. private communications.

[108] Sonoyama, K.; Takanishi, Y.; Ishikawa, K.; Takezoe, H. Position-sensitive cholesteric liquid crystal dye laser covering a full visible range. *Jpn. J. Appl. Phys.* **46**, 874–876 (2007).

[109] Furumi, S.; Yokoyama, S.; Otomo, A.; Mashiko, S. Phototunable photonic bandgap in a chiral liquid crystal laser device. *Appl. Phys. Lett.* **84**, 2491–2493 (2004).

[110] Bajc, J.; Bezić, J.; Žumer S. Chiral nematic droplets with tangential anchoring and negative dielectric anisotropy in an electric field. *Phys. Rev. E* **51**, 2176–2189 (1995).

[111] Ohta, T.; Song, M. H.; Tsunoda, Y.; Nagata, T.; Shin, K.-C.; Araoka, F.; Takanishi, Y.; Ishkawa, K.; Watanabe, J.; Nishimura, S.; Toyooka T.; Takezoe, H. Monodomain film formation and lasing in dye-doped polymer cholesteric liquid crystals. *Jpn. J. Appl. Phys.* **43**, 6142–6144 (2004).

[112] Matsui, T.; Ozaki, R.; Funamoto, K.; Ozaki, M.; Yoshino, K. Flexible mirrorless laser based on a free-standing film of photopolymerized cholesteric liquid crystal. *Appl. Phys. Lett.* **81**, 3741–3743 (2002).

[113] Finkelmann, H.; Kim, S. T.; Munoz, A.; Palffy-Muhoray, P.; Taheri, B. Tunable mirrorless lasing in cholesteric liquid crystalline elastomers. *Adv. Mater.* **13**, 1069–1072 (2001).

[114] Manabe, T.; Sonoyama, K.; Takanishi, Y.; Ishikawa, K.; Takezoe, H. Toward practical application of cholesteric liquid crystals to tunable lasers. *J. Mater. Chem.* **18**, 3040–3043 (2008).

[115] Muševič, I.; Škarabot M.; Humar, M. Direct and inverted nematic dispersions for soft matter photonics. *J. Phys.: Condens. Matter.* **23**, 284112 (2011).

[116] Muševič, I.; Humar, M. Tunable liquid crystal optical microcavities. *Proceedings of SPIE* **7955**, 795509 (2011).

[117] Humar, M.; Muševič, I. Surfactant sensing based on whispering-gallery-mode lasing in liquid-crystal microdroplets. *Opt. Express* **19**, 19836–19844 (2011).

[118] Tanyeri, M.; Perron, R.; Kennedy, I. M. Lasing droplets in a microfabricated channel. *Opt. Lett.* **32**, 2529–2531 (2007).

[119] Humar, M.; Muševič, I. 3D microlasers from self-assembled cholesteric liquid-crystal microdroplets. *Opt. Express* **18**, 26995–27003 (2010).

[120] Won, R. Liquid crystals: Tiny tunable 3D lasers. *Nat. Photonics* **5**, 133 (2011).

Index of Figures

1 Schematics of WGMs 2
2 Two examples of tunable WGM resonators 3
3 Silica microtoroid resonator used for biosensing 4
4 CROW simulation 5
5 2D Bragg microcavity laser 6
6 CLC laser 7
7 LC sensor on hard surface interface 8
8 LC sensor on fluid interface 9
9 Proposed CROW structure made from nematic colloids 11

10 Electric field intensity distributions in the equatorial plane of the sphere for TE WGMs with $l = m = 30$ and $n = 1, 2$ and 3 17
11 Radial light intensity for TE WGMs with $l = m = 60$ and $n = 1, 2$ and 3 . . . 19
12 Three basic types of spherical Bragg microcavities 24
13 Intensities for two Bragg defect modes 25
14 LC molecule orientation 25
15 Refractive indices of E12 as the temperature is increased 28
16 Two types of anchoring of a NLC 29

17 Dye molecules 32
18 Schematics of the optical setup 35
19 Photo of the optical setup 37
20 Microfluidic setup for chemical sensing 38
21 Experimental setup for angle dependence measurements 39
22 Experimental setup for 3D laser polarization measurements 40
23 Experimental setup for strain tuning measurements 41

24 Dispersion of E12 droplets in PDMS under crossed polarizers 43
25 Radial NLC droplet 44
26 Assembly of liquid-crystal droplets in PDMS 44
27 Two examples of tubes formed from E12 LC when mixed with PDMS 45
28 A LC shell 45
29 Schematic view of WGMs in a LC droplet 46
30 False color image of fluorescent light intensity from a LC droplet 47
31 Spectrum od fluorescent light captured from a LC droplet 47
32 Fiber excitation of WGMs in LC droplets 48
33 WGM polarization schematics in LC droplets 48
34 WGM spectra at different polarizations 49
35 Fluorescence images at different polarizations 50
36 Spectra of fluorescent light from two E12 droplets in PDMS 51
37 Nematic droplet director configuration under applied electric field 54
38 Schematic drawing of the light circulation in a LC droplet 54

39 WGM spectrum versus applied electric field 55
40 WGM tunability as a function of droplet diameter 55
41 Intensity oscillation under field 56
42 Tunability of two droplets 57
43 Images of a droplet with in-plane field 58
44 Tunability with in-plane field 58
45 A LC droplet containing pericles 59
46 Temperature tunability of WGMs 61
47 Calculation of temperature tunability of WGMs (large droplet) 62
48 Calculation of temperature tunability of WGMs (small droplet) 62
49 WGM spectra at two temperatures. 63
50 Image of a LC droplet with increasing temperature 64
51 Linewidth and Q-factor as a function of temperature 65
52 Optical tuning of WGMs 66
53 Optical manipulation of the LC in a droplet 67
54 Images and WGM positions of a LC droplet under increasing strain 70
55 Artist impression of a WGM LC chemical sensor 71
56 Sequence of LC droplets at increasing SDS concentration 72
57 Fluorescent spectra for radial and bipolar droplets 73
58 Lasing intensity for radial and bipolar droplets 74
59 Lasing spectrum as the concentration is increased 75
60 Lasing spectrum as water and SDS ar added 76
61 Fluorescent spectrum in a non-lasing regime 76
62 CLC droplets micrographs 77
63 An artist's impression of a 3D CLC laser 78
64 CLC droplet director configuration simulation 79
65 Transmission through a CLC droplet: simulation and experiment 80
66 Emission of light from a 3D laser when the intensity of the pump laser is gradually increased 81
67 Optical properties of a spherical CLC laser 82
68 Temporal spectral properties of a spherical CLC laser 83
69 Lasing properties as a function of droplet diameters 84
70 Lasing and reflection spectrum 84
71 Polarization measurements of the 3D laser 85
72 Angle dependance of lasing 86
73 A micrograph of a CLC laser from different view directions 86
74 Temperature tunability 87
75 Lasing of higher Bragg modes in longer pitch droplets 88
76 Lasing of higher Bragg modes and WGM lasing in longer pitch droplets . . . 89
77 WGM and Bragg thresholds 90
78 Polymerized CLC spherical laser 91
79 Output intensity versus input intensity of single laser pulses 92
80 A CLC spherical laser with included particles 93

81 Ferroelectric LC droplets in PDMS 115
82 Lasing in ferroelectric LC droplets 116
83 Electric field switching in ferroelectric LC droplets 116
84 Photonic molecules 117
85 Time response of the 3D laser 119

Index of Tables

1 Properties of LCs . . . 31
2 Carrying materials . . . 33

Appendix A: Further observations

In the appendix I will give some additional preliminary experimental results of the not yet finished work and the results that do not have good enough explanation.

Lasing and switching in ferroelectric LCs

Ferroelectric liquid crystals are known for their fast switching under applied electric field. Therefore, they could be a good candidate as a material for droplets used for WGM microcavities instead of nematic LCs. We introduced nile red fluorescent dye into a ferroelectric liquid crystal (SmC*, Kingston Chemicals) and mixed it with PDMS. The ratios of the materials and the mixing procedures were the same as with nematic droplets (Section 4.1). The produced droplets are unfortunately not completely spherical and their internal structure is also in majority of cases full of defect lines (Figure 81). Some smaller droplets, have however nice structure with a diametral defect line, extending from one surface of the droplets, through the center, to the other surface.

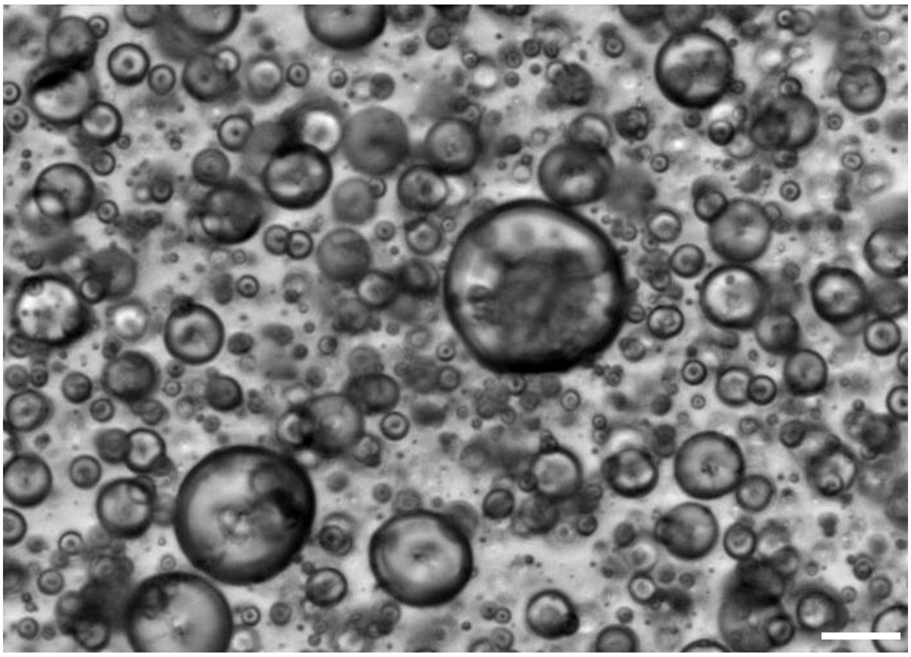

Figure 81: *Ferroelectric LC droplets in PDMS.* Most of the droplets do not have a nice spherical shape or they contain defect structures. Scale bar 20 µm.

We have illuminated the droplets with the CW Ar-ion laser to excite the WGMs. However, in the fluorescent spectrum from a single droplet we did not observe any spectral peaks. We than used the pulsed Nd:YAG doubled laser as an excitation source. In this case we have observed several spectral lines (Figure 82). The lines appear in groups, indicating a non-spherical shape of the droplet.

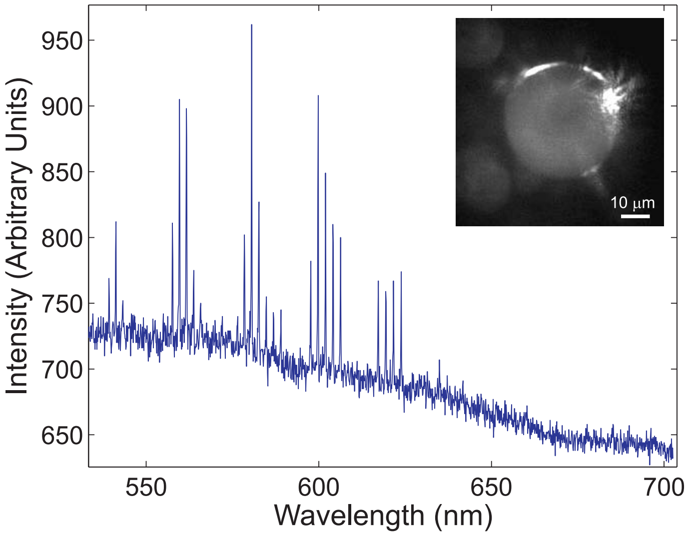

Figure 82: *Lasing in ferroelectric LC droplets.* Spectrum of lasing of a 30 μm diameter droplet. Inset shows a fluorescent image of the lasing droplet.

When the droplet was illuminated with the pulsed laser, an electric field of 1 V/μm was applied to the cell containing the dispersion of droplets. The spectral lines shifted by approximately 2 nm to shorter wavelengths (Figure 83). The tunability is in this case quite small compared to the nematic droplets of the same size. Also the speed of switching is in order of seconds, which is extremely slow even when compared to nematic droplets. When turning the electric field on or off, the change in the internal structure of the droplet can be seen by naked eye, that it is very slow. We believe that unwinding of the helix is taking place when applying electric field, which is a slow process. The droplets should be smaller than the pitch to achieve fast switching, however in such small droplets, no lasing is observed.

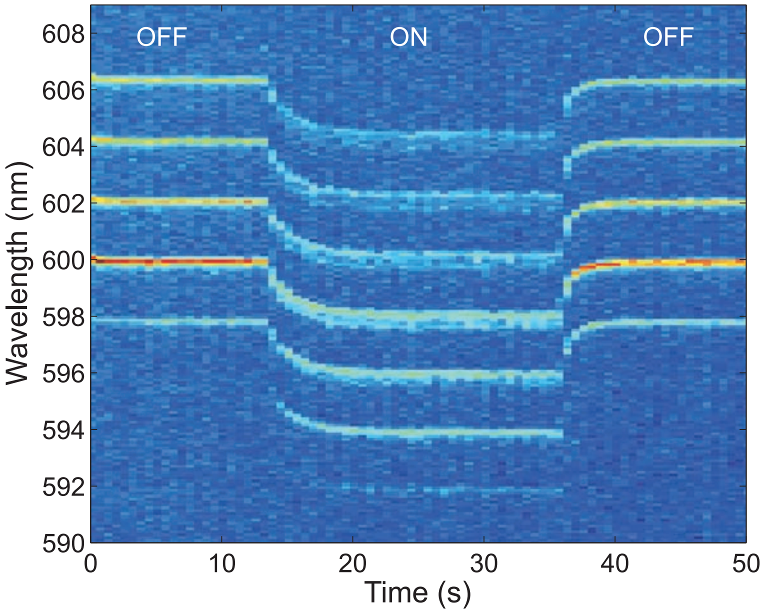

Figure 83: *Electric field switching in ferroelectric LC droplets.* Electric field of 1 V/μm has been applied to the droplet. Shifting of modes to shorter wavelengths is observed with the characteristic time in the order of seconds.

Photonic molecules

The idea was to couple two WGM microcavities and observe tunneling of light from one to another and the splitting of their modes because of coupling. To achieve resonant transfer of light, at least one mode from one microcavity should match one other mode in the other microcavity. With tunable WGMs in liquid-crystal droplets this is easy to achieve by using electric field. Two droplets of different size have different tunabilities and with increasing the electric field, there is a great chance that two modes will match (Section 4.3.3). To have a simpler system we have used 10 μm non-tunable fluorescent solid melamine formaldehyde (MF) particles and non-fluorescent E12 LC droplets. Both the solid particles and the LC were mixed into the PDMS forming a dispersion of both solid and liquid particles. In some cases a droplet was in close contact with a solid particle (Figure 84a). The separation between both could be also controlled by using the IR laser tweezers. The fluorescent MF particle was illuminated by the CW Ar-ion laser and the spectrum was collected from the LC droplet. As the electric field was increased, the positions of WGMs were analyzed (Figure 84b). Instead of a continuous variation of the frequencies of WGMs, steps are observed. This could indicate mode splitting because of coupling of modes in the two resonators. However, further measurements with higher resolution spectrometer have to be performed to confirm the results.

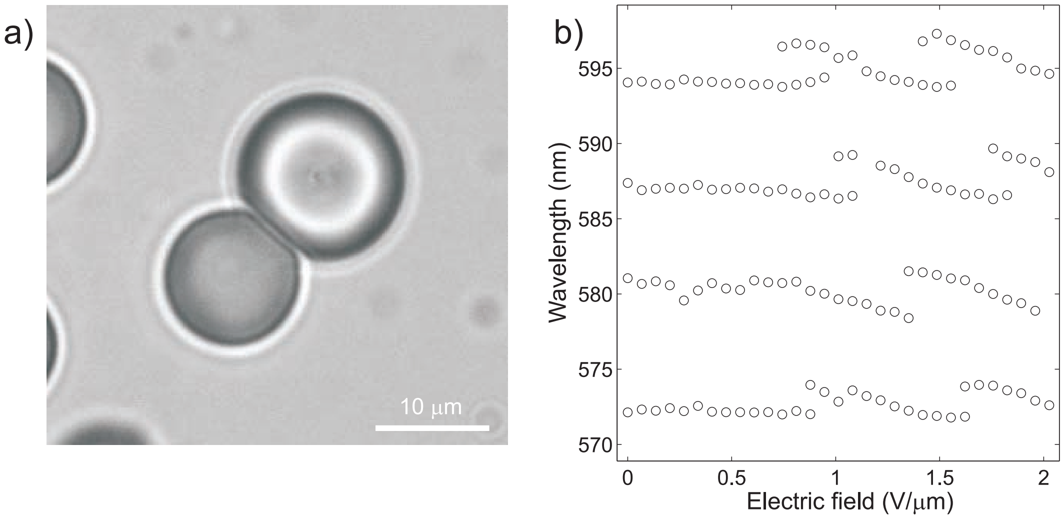

Figure 84: *Photonic molecules.* a) A fluorescent 10 μm MF particle in contact with an E12 LC droplet in PDMS. b) Positions of WGMs in the droplet with the MF particle being excited while the electric field is increased.

Measuring spectral width of WGMs using a Fabriy-Perot interferometer

To measure the Q-factor of WGMs in nematic LC crystal, we have used a spectrometer with the resolution of 0.05 nm. We have found that the spectral width of WGMs is the same or below this resolution. To use a higher resolution spectrometer of the same kind is not convenient because of the large size and price of such a device. Other methods could be used such as coupling of a droplet with a tapered fiber and using a narrow line tunable laser (Section 2.2.5.1). Other method would be to use a Fabriy-Perot interferometer. The interferometer is made similarly as a laser cavity with two highly reflective mirrors. Only the light that matches a mode inside the resonator is transmitted through the interferometer. One mirror is connected to a piezo actuator so that the modes in the cavity are scanned over the whole FSR of the interferometer. The interferometer is useful just to measure spectral features that are narrower than its FSR. In the other case the spectral features can overlap. The idea is to use the spectrometer as a monochromator that can pass to its output only a very narrow spectral region. A single WGM line can be selected by rotating the grating and by choosing the appropriate output slit width. This single line is then sent through the scanning interferometer to a photomultiplier.

Unfortunately when performing this experiment, the intensity of this single spectral line was so weak, that just noise was detected on the photomultiplier. To get better signal, the WGMs should be exited above the lasing threshold to achieve higher intensity, as well as a lock-in amplifier should be used at the output of the photomultiplier.

Pulse length of the 3D laser

We have also measured pulse length of the 3D laser and compared it to the pulse length of the spontaneous fluorescence (that is below the lasing threshold) and the pulse length of the Q-switched Nd:YAG excitation laser. We have used a fast photodiode and a 2.5 GHz oscilloscope (LeCray, WavePro 725Zi). A single CLC droplet was excited in the same way as for previous experiments and the generated light was sent through an optical fiber to the photodiode.

First, pulse length of the excitation laser (blue line) was measured. The results are shown in Figure 85. After the main pulse, a second pulse can be observed, which we believe originates from the photodiode and the amplifier. After the second pulse the signal also goes to negative values, which can not be attributed to the signal from the laser, but an artifact from the electronics. The length of the first pulse is 3 ns. The specified pulse length of the Q-switched laser given by the manufacturer is below 1 ns. We can conclude that the photodiode is not fast enough for this measurements. Regardless of this, a slightly different time response can be measured for the light emitted by a 3D laser compared to the excitation pulse. Below the lasing threshold (green line), the pulse length becomes longer in agreement to the typical fluorescence lifetime of the organic dyes. Above the lasing threshold (red line) the pulse length is shorter than for fluorescence. In this case, one would expect longer pulse length, since the light is trapped in the resonator and does not escape so fast. However, for the 3D laser line spectral width of 0.1 nm, the Q-factor equals 6000 and the corresponding photon lifetime in the resonator using (2) is of 0.002 ns. This is three orders of magnitude faster than the fluorescence lifetime and does not contribute to the results. On the other hand, it is obvious that the laser pulse from the CLC laser should be shorter than the fluorescence lifetime, since after long time, most of the excited molecules spontaneously decay into lower states and the population inversion no longer exists.

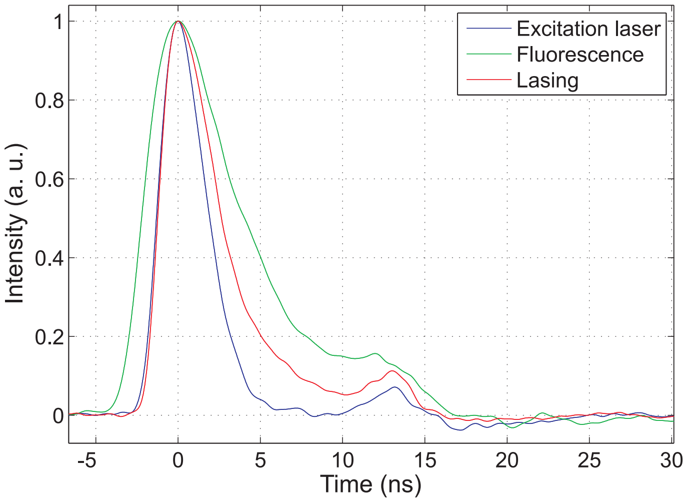

Figure 85: *Time response of the 3D laser.* Normalized intensity on a fast photodiode of a single pulse for the three cases: the Q-switched excitation laser and the 3D laser below the lasing threshold and above the lasing threshold.

Appendix B: Bibliography

List of publications related to this dissertation

- Humar, M.; Ravnik, M.; Pajk, S.; Muševič. I. Electrically tunable liquid crystal optical microresonators. *Nat. Photonics* **3**, 595–600 (2009).
- Humar, M.; Muševič, I. 3D microlasers from self-assembled cholesteric liquid crystal microdroplets. *Opt. Express* **18**, 26995–27003 (2010).
- Muševič, I.; Škarabot, M.; Humar, M. Direct and inverted nematic dispersions for soft matter photonics. *J. Phys.: Condens. Matter.* **23**, 284112 (2011).
- Muševič, I.; Humar, M. Tunable liquid crystal optical microcavities. *Proceedings of SPIE* **7955**, 795509-1–795509-8 (2011).
- Humar, M.; Muševič, I. Surfactant sensing based on whispering-gallery-mode lasing in liquid-crystal microdroplets. *Opt. Express* **19**, 19836–19844 (2011).

List of patents related to this dissertation

- Muševič, I.; Humar, M. Kroglasti tekočekristalni laser: patentna prijava P-201000377. Ljubljana: Urad RS za intelektualno lastnino, 2010.
- Muševič, I.; Humar, M. Spherical liquid-crystal laser: International Patent Application, PCT/EP2011/005607, 2011.